https://doi.org/10.15388/vu.thesis.960
https://orcid.org/0009-0008-1568-2557

VILNIUS UNIVERSITY
CENTER FOR PHYSICAL SCIENCES AND TECHNOLOGY

Sonata Pleskytė

Investigation of Photocatalytic Degradation Processes and Mechanisms of LDPE Microplastics Using TiO_2-based Nanomaterials

DOCTORAL DISSERTATION

Natural Sciences,
Chemistry (N 003)

VILNIUS 2026

The dissertation was prepared between 2022 and 2026 in the Center for Physical Sciences and Technology (Lithuania). The research was supported by the Research Council of Lithuania.

Academic Supervisors:
Dr. Ieva Uogintė (Center for Physical Sciences and Technology, Natural Sciences, Chemistry – N 003, 2025-01-10–2026-09-30).
Dr. Steigvilė Byčenkienė (Center for Physical Sciences and Technology, Natural Sciences, Chemistry – N 003, 2022-10-01– 2025-01-09).

This doctoral dissertation will be defended in a public meeting of the Dissertation Defence Panel:

Chairperson – Dr. Rita Plukienė (Center for Physical Sciences and Technology, Natural Sciences, Physics – N 002).
Members:
Assoc. Prof. Dr. Lina Mikoliūnaitė (Center for Physical Sciences and Technology, Natural Sciences, Chemistry – N 003),
Prof. Dr. Rasa Pauliukaitė (Center for Physical Sciences and Technology, Natural Sciences, Chemistry – N 003),
Prof. Habil. Dr. Iwona S. Stachlewska (University of Warsaw, Natural Sciences, Physics – N 002),
Dr. Arūnas Stirkė (Center for Physical Sciences and Technology, Natural Sciences, Chemistry – N 003).

The dissertation will be defended at a public meeting of the Dissertation Defence Panel at 2 p.m. on September 4, 2026, in meeting room D401 of the Center for Physical Sciences and Technology.

Address: Saulėtekio av. 3, Room No. D401, Vilnius, Lithuania.
Tel. +370 645 15 550; e-mail: office@ftmc.lt.

https://doi.org/10.15388/vu.thesis.960
https://orcid.org/0009-0008-1568-2557

VILNIAUS UNIVERSITETAS
FIZINIŲ IR TECHNOLOGIJOS MOKSLŲ CENTRAS

Sonata Pleskytė

LDPE mikroplastiko fotokatalitinės degradacijos procesų ir mechanizmų tyrimas naudojant TiO_2 nanomedžiagas

DAKTARO DISERTACIJA

Gamtos mokslai,
Chemija (N 003)

VILNIUS 2026

Disertacija rengta 2022–2026 metais Fizinių ir technologijos mokslų centre. Mokslinius tyrimus rėmė Lietuvos mokslo taryba.

Moksliniai vadovai:
dr. Ieva Uogintė (Fizinių ir technologijos mokslų centras, gamtos mokslai, chemija – N 003; 2025-01-10–2026-09-30).
dr. Steigvilė Byčenkienė (Fizinių ir technologijos mokslų centras, gamtos mokslai, chemija – N 003; 2022-10-01– 2025-01-09).

Gynimo taryba:
Pirmininkė – dr. Rita Plukienė (Fizinių ir technologijos mokslų centras, gamtos mokslai, fizika – N 002).
Nariai:
doc. dr. Lina Mikoliūnaitė (Fizinių ir technologijos mokslų centras, gamtos mokslai, chemija – N 003),
prof. dr. Rasa Pauliukaitė (Fizinių ir technologijos mokslų centras, gamtos mokslai, chemija – N 003),
prof. habil. dr. Iwona S. Stachlewska (Varšuvos universitetas, gamtos mokslai, fizika – N 002),
dr. Arūnas Stirkė (Fizinių ir technologijos mokslų centras, gamtos mokslai, chemija – N 003).

Disertacija ginama viešame Gynimo tarybos posėdyje 2026 m. rugsėjo mėn. 4 d. 14 val. Fizinių ir technologijos mokslų centro D401 posėdžių salėje.

Adresas: Saulėtekio al. 3, Vilnius, Lietuva, tel. +370 645 15 550, el. paštas info@ftmc.lt.

ABBREVIATIONS

AA	Acetic acid
AO	Ammonium oxalate
AOPs	Advanced oxidation processes
ATR	Attenuated Total Reflectance
BPA	Bisphenol A
BC	Biochar
CB	Conduction band
CI	Carbonyl index
DSC	Differential scanning calorimetry
EDX	Energy dispersive X-ray Spectroscopy
EPR	Electron Paramagnetic Resonance
FWHM	Full Width and Half Maximum
FTIR	Fourier Transform Infrared Spectroscopy
HAADF	High-Angle Annular Dark Field
HDPE	High-density polyethylene
IPA	Isopropyl alcohol
IR	Infrared
IS	Ionic strength
ISO	International Organization for Standardization
Kao	Kaolinite
LDPE	Low-density polyethylene
MMT	Montmorillonite
Mt	Metric ton
NPs	Nanoparticles
PA	Polyamide
PA66	Polyamide 66
PE	Polyethylene
PES	Polyester
PET	Polyethylene terephthalate
PP	Polypropylene

PS	Polystyrene
PU	Polyurethane
PVC	Polyvinyl chloride
PZC	Point of zero charge
PZNPC	Point of zero net proton charge
ROS	Reactive oxygen species
SD	Standard deviation
SEM	Scanning Electron Microscopy
SPR	Surface plasmon resonance
SSE	Sum of squared errors
TEM	Transmission Electron Microscopy
UV	Ultraviolet
VB	Valence band
VI	Vinyl index
Vis	Visible
WWTP	Wastewater treatment plant
WDXRF	Wavelength-dispersive X-ray fluorescence
XRD	X-Ray Diffraction

CONTENTS

INTRODUCTION

Plastics have become an indispensable material in modern society. However, their extensive use and accumulation have led to significant environmental concerns, with plastic pollution as the third major contributor to global waste (Yatoo et al., 2024). Current plastic waste management strategies rely on landfilling (79%), incineration (12%), and mechanical recycling (9%) (Geyer et al., 2017). Although landfilling remains a dominant global disposal method, it is considered the least favorable option due to its potential to contaminate soil and groundwater. According to Fayshal (2024), plastic waste is projected to reach 1 billion metric tons (Mt) by 2060. When plastic items enter the environment, instead of being completely mineralized into harmless organic matter, they fragment into even smaller pieces known as microplastics.

To date, microplastics have been detected across diverse ecosystems, including marine and terrestrial environments, and in a wide range of organisms, from wildlife to humans. Although the adverse effects of microplastics on living organisms are still being actively investigated, emerging evidence suggests that these particles may cause a range of harmful effects, including physical tissue damage, inflammatory responses, oxidative stress, and disruption of cellular and physiological processes (Jung et al., 2025).

Low-density polyethylene (LDPE) microplastics originate from one of the most widely used plastic polymers globally, owing to its extensive application in packaging materials, consumer goods, and industrial products. In addition, LDPE mulch films represent the primary source of global agricultural plastic waste, with annual consumption exceeding 1.6 Mt over 20 million hectares of farmland (Koskei et al., 2021). Europe alone generates more than 1.3 million Mt of agricultural waste annually (Maraveas and Hahladakis, 2025). Microplastics derived from agricultural plastic waste can become airborne through wind dispersal or enter aquatic systems via runoff or storms. The recycling of LDPE films is often technically and economically unfeasible due to their multilayer structure, pigment content, and substantial contamination with soil and organic matter, which can constitute over half of the total waste mass (Carrieri et al., 2025). This elevated mass increases waste volumes, raises logistical costs, and can damage processing equipment, thereby making the production of virgin plastics more economically favorable than recycling such materials.

The persistence and widespread distribution of microplastics in environmental matrices have highlighted the growing need for removal and

degradation technologies, with advanced oxidation processes (AOPs) considered among the most effective approaches. A considerable number of studies have investigated various catalysts, including pure semiconductors and metal oxides (TiO_2, ZnO), carbon-based nanomaterials, and nanocomposites, to induce microplastic degradation via reactive oxygen species (ROS) generation (Kaur and Kaur, 2025). While these materials have already shown promising results, many of them are synthetic, costly, or hazardous, limiting their practical applicability (Ahmed et al., 2025). The development of sustainable alternatives, especially nanocomposites with natural materials, enhances the scalability of photocatalytic degradation methods. Thus, in this study, TiO_2-clay nanomaterials were chosen for their environmental abundance, cost-effectiveness, and ability to provide high surface area and versatile functionality (Ding et al., 2022).

The existing research predominantly relies on model microplastics with simplified compositions that do not accurately reflect the complexity of real-world plastic waste (Ramírez-Escárcega et al., 2025). Environmental microplastics exhibit diverse physicochemical properties, including polymer type, additive type and amount, surface morphology, size, and color, all of which can influence their degradation efficiency. Therefore, there is a critical need to investigate environmentally relevant microplastics, with an emphasis on understanding how their physicochemical characteristics collectively affect degradation efficiency.

RELEVANCE

Conventional plastic and microplastic management approaches are often slow and insufficient, leading to long-term environmental and ecological risks. Photocatalytic degradation offers a promising, environmentally friendly strategy that can break down complex polymer structures without causing secondary pollution. Investigating this process in the aqueous phase is particularly important, as it can further be applied in wastewater treatment plants (WWTPs), which are considered the main barrier between anthropogenic activity and natural water bodies. The European Parliament, through the revised Urban Wastewater Treatment Directive (EU) 2024/3019, proposed the inclusion of microplastics as emerging pollutants, introducing systematic monitoring and promoting treatment technologies to achieve at least 80% removal of microplastics from urban wastewater, in line with broader EU objectives to reduce microplastic emissions by 30% by 2030 (European Parliament and Council of the European Union, 2024). Understanding the mechanisms of microplastic degradation, including the

effects of reaction parameters, the physicochemical properties of microplastics, and the generation of ROS, reveals pathways of microplastic mineralization under realistic conditions. The outcomes of such a study contribute to the development of more efficient water treatment technologies and mitigation approaches for plastic pollution.

THE MAIN STUDY AIM

The aim of this study is to evaluate the photocatalytic degradation efficiency and mechanisms of LDPE microplastics using titanium dioxide (TiO_2)-based nanomaterials in an aqueous medium. To address this aim, the following tasks were established:

TASKS

1. To synthesize TiO_2, TiO_2-Kao, and TiO_2-MMT nanomaterials using the sol-gel method, and Ag-TiO_2 NPs with varying Ag concentrations using the photoreduction method.
2. To characterize the structural, morphological, optical, and chemical properties of as-synthesized nanomaterials.
3. To examine the photocatalytic degradation of LDPE fragment-type microplastics in batch experiments, including the effect of materials ratio, pH, and ionic strength.
4. To investigate the influence of the physical properties of LDPE film-type microplastics on photocatalytic degradation efficiency.
5. To assess the formation of ROS within the photocatalytic degradation system and propose potential reaction mechanisms.

SCIENTIFIC NOVELTY

In this research, commercial, “real-to-world” LDPE mulch films and natural clay-based nanomaterials were systematically investigated in a TiO_2-driven photocatalytic degradation system. It evaluates the combined effect of various physicochemical properties of LDPE microplastics alongside a mechanistic analysis of ROS generation. This work provides a deeper understanding of the behavior of complex microplastic pollutants and direct applicability to “real-to-world” microplastic degradation strategies.

STATEMENTS OF THE DEFENSE

1. The modification of TiO_2 NPs with clay and metal NPs enhances the TiO_2 photocatalytic activity, leading to improved degradation efficiency of LDPE compared to unmodified TiO_2.
2. The photocatalytic degradation efficiency of fragment-type LDPE microplastics is increased by optimizing key reaction parameters, specifically through an acidic environment, higher catalyst loading, and prolonged irradiation duration.
3. The physical properties of film-type LDPE microplastics, particularly their size and color, influence the efficiency of photocatalytic degradation. Smaller, black LDPE microplastics are degraded twice as effectively as transparent ones.
4. Hydroxyl radicals *(·OH)* and superoxide radicals ($O_2^{\cdot -}$) are primarily ROS that initiate and control the film-type LDPE photocatalytic degradation processes and mechanisms in reaction systems driven by Ag-TiO_2.

AUTHOR CONTRIBUTION

The author of this work synthesized all studied materials (TiO_2, TiO_2-Kao, TiO_2-MMT, Ag-TiO_2), planned and conducted studies on the photocatalytic degradation of LDPE microplastics. Conducted UV-VIS and ATR-FTIR characterization and performed results interpretation. Participated in XRD, SEM, TEM, and XRF measurements and interpreted results. The author carried out data analysis and validation of photocatalytic degradation experiments, prepared graphical illustrations and data visualizations, wrote the original manuscripts, and submitted the findings to scientific journals. The results were presented by the author at multiple national and international scientific conferences. In addition, the author disseminated the results of this dissertation through numerous public outreach activities.

LIST OF PUBLICATIONS

1. **Pleskytė, S.**, Uogintė, I., Stanionytė, S., Selskienė, A., Byčenkienė, S. (2025). Application of nanocomposites based on TiO_2 and clay minerals for the photocatalytic degradation of low-density polyethylene microplastics. *International Journal of Environmental Science and Technology,* 22, 17061–17080. https://doi.org/10.1007/s13762-025-06752-3.
2. **Pleskytė, S.**, Uogintė, I., Selskienė, A., Stanionytė, S., Skapas, M., Giraitis, R., Byčenkienė, S. (2026). Photocatalytic degradation of LDPE films with Ag-TiO_2 catalysts: role of microplastic film size and color. *Journal of Environmental Chemical Engineering,* 14(2). https://doi.org/10.1016/j.jece.2026.121975.

OTHER PUBLICATIONS

3. Uogintė, I., **Pleskytė, S**., Skapas, M., Stanionytė, S., Lujanienė, G. (2023). Degradation and optimization of microplastic in aqueous solutions with graphene oxide-based nanomaterials. *International Journal of Environmental Science and Technology*, 20(9), 9693–9706. https://doi.org/10.1007/s13762-022-04657-z.
4. **Pleskytė, S.**, Uogintė, I., Burbulytė, A., Byčenkienė, S. (2023). Characteristics and removal efficiency of microplastics at a secondary wastewater treatment plant in Lithuania. *Water Environment Research,* 95 (12). https://doi.org/10.1002/wer.10958.
5. Sorkytė, Š., Byčenkienė , S., Uogintė, I., **Pleskytė, S**., Šiukščius, A., Virgailis, M., Šiugždinienė, R., Vaičiulienė, G., Rekešiūtė, A., Sutkevičienė, N. (2026). Microplastics in the seminal microenvironment of boar semen: associations with sperm motility and antimicrobial susceptibility. *Frontiers in Veterinary Science,* 13. https://doi.org/10.3389/fvets.2026.1847076.

LIST OF CONFERENCES

In total, the author presented **12 oral presentations** and **6 posters** at national and international conferences.

1. **Pleskytė, S.**, Uogintė, I. Photocatalytic degradation of microplastic in aqueous environment. 12th Conference of Doctoral Students and Young Researchers "FizTech 2022", October 19-20th 2022, Vilnius, Lithuania. P2 **(poster)**.
2. **Pleskytė, S.**, Uogintė, I. Seasonal variation, distribution and characteristics of microplastic in sewage sludge. "Micro 2022:Online atlas edition", November 14-18th, 2022, Lanzarote, Spain **(poster)**.
3. **Pleskytė, S.**, Uogintė, I., Byčenkienė, S. Removal efficiency and distribution of microplastic particles at wastewater treatment plant. 66th International Conference for Students of Physics and Natural Sciences "Open readings 2023", April 18th-21st, 2023, Vilnius, Lithuania **(poster)**.
4. **Pleskytė, S.**, Uogintė, I., Byčenkienė, S. Correlation between microplastic properties and removal efficiency in wastewater treatment plants. COST ACTION PRIORITY Training School "Recent Trends in Microplastic Research" May 22nd-26th, 2023, Jena, Germany **(poster, oral presentation)**.
5. **Pleskytė, S.**, Uogintė, I., Byčenkienė, S. New insights into microplastic pollution levels at wastewater treatment plant: removal efficiency and distribution across treatment stages. "18th International Conference on Chemistry and the Environment (ICCE) 2023", June 11-15th, 2023, Venice, Italy **(oral presentation)**.
6. **Pleskytė, S.**, Uogintė, I., Byčenkienė, S. Time-dependent photodegradation of low-density polyethylene microplastic particles using TiO_2 nanoparticles. National scientific conference "CHEMIJA IR GEOMOKSLAI 2024", March 22nd, 2024, Vilnius, Lithuania **(poster)**.
7. **Pleskytė, S.**, Uogintė, I., Byčenkienė, S. Photocatalytic degradation of low-density polyethylene in aqueous solution using TiO_2 nanoparticles deposited on clay kaolinite. 67th International Conference for Students of Physics and Natural Sciences "Open readings 2024", April 23rd-26th, 2024, Vilnius, Lithuania **(poster)**.
8. **Pleskytė, S.**, Uogintė, I., Byčenkienė, S. Photocatalytic degradation of LDPE microplastics by a TiO_2-clay nanomaterial "Chemistry and Chemical Technology 2024" (CCT2024)", May 17th, 2024, Kaunas, Lithuania **(oral presentation, received the best oral presentation award)**.

9. **Pleskytė, S.**, Uogintė, I., Byčenkienė, S. Enhanced photocatalytic degradation of LDPE Microplastics using TiO_2-Kaolinite and TiO_2-Montmorillonite Nanomaterials. "Micro 2024: Plastic Pollution from Macro to Nano", September 23rd-27th, 2024, Lanzarote, Spain **(oral presentation)**.
10. **Pleskytė, S.**, Uogintė, I., Byčenkienė, S. Application of TiO_2-based nanocomposites for the photocatalytic degradation of LDPE microplastics. 14th Conference of Doctoral Students and Young Researchers "FizTech 2024", October 15-17th, 2024, Vilnius, Lithuania **(oral presentation)**.
11. **Pleskytė, S.**, Uogintė, I., Byčenkienė, S. The Photocatalytic Degradation Process and Mechanisms of LDPE Microplastics Using Nanocomposites Based on TiO_2 and Clay Minerals. 4th International Student Conference "DISC2024", December 5-6th, 2024, Belgrade, Serbia, online **(oral presentation)**.
12. **Pleskytė, S.**, Uogintė, I., Byčenkienė, S. Influence of Microplastic Film Size on Photocatalytic Degradation of LDPE Using Ag-TiO_2 Nanomaterials. 68th International Conference for Students of Physics and Natural Sciences "Open readings 2025", May 13-16th, 2025, Vilnius, Lithuania **(oral presentation)**.
13. **Pleskytė, S.**, Uogintė, I., Byčenkienė, S. Photocatalytic degradation of low-density polyethylene (LDPE) microplastic mulch films using Ag-TiO_2 "19th International Conference on Chemistry and the Environment (ICCE) 2025", June 8-12th, 2025, Belgrade, Serbia **(oral presentation)**.
14. **Pleskytė, S.**, Uogintė, I., Byčenkienė, S. Photocatalytic degradation of LDPE mulch films using Ag-TiO_2 nanomaterials: the role of LDPE film size and color. The 24th biennial conference "EcoBalt2025", October 8-10th, 2025, Vilnius, Lithuania **(oral presentation)**.
15. **Pleskytė, S.**, Uogintė, I., Selskienė, A., Byčenkienė, S. Impact of the physical properties of LDPE mulch films on photocatalytic degradation efficiency under UV irradiation. 15th Conference of Doctoral Students and Young Researchers "FizTech 2025", October 21st-22nd, 2025, Vilnius, Lithuania **(oral presentation, received the best oral presentation award)**.
16. **Pleskytė, S.**, Uogintė, I., Selskienė, A., Byčenkienė, S. Photocatalytic Degradation of Microplastics: Effects of LDPE Film Properties and Degradation Mechanisms. 2nd International online conference "Microplastics and Nanoparticles: Emerging Threats to Environmental Health", November 21st, 2025, Klaipėda, Lithuania **(oral presentation, invited)**.

17. **Pleskytė, S.**, Uogintė, I., Selskienė, A., Byčenkienė, S. Influence of physical properties on the photocatalytic degradation of LDPE mulch films. 3rd International Conference "MICROPLASTICdays", February 2nd-5th, 2026, Ljubljana, Slovenia **(oral presentation)**.

PROFESSIONAL DEVELOPMENT

The author participated in **4 international training schools** focused on microplastic research, and **1 international training school** on environmental chemistry and atmospheric sciences.

1. COST Action Priority Summer School "Recent Trends in Microplastic Research", Jena, Germany (May 22–26, 2023).
2. University of Pisa training School "Advanced techniques for the analysis of novel materials strategic for sustainability transitions. 1-BIOPLASTICS", Pisa, Italy (January 29–February 2, 2024).
3. International 7th Baltic Earth Winter School for Young Scientists on "Earth System Science for the Baltic Sea Region" Klaipeda, Lithuania (March 24–28, 2025).
4. Aalborg University training school "Microplastic Research – Analytical Methods for Microplastic Quantification" (ONLINE), Aalborg, Denmark (October 1–15, 2025).
5. University of Ljubljana training school "Measurement uncertainties in microplastic laboratory research: Towards reliable and comparable results", Ljubljana, Slovenia (February 5th, 2026).

1. LITERATURE REVIEW

1.1. Microplastics

The invention of plastic materials occurred in the late 19th century. The development of the plastic industry was determined by the discovery of Bakelite (a phenol-formaldehyde resin) by Leo Baekeland between 1907 and 1909, which is recognized as the first fully synthetic plastic (Sayam et al., 2026). The successful invention of Bakelite was followed by the development of other common polymers, such as polyvinyl chloride (PVC), polystyrene (PS), polyurethane (PU), and polyamide (PA). Most synthetic plastics manufactured worldwide originate from non-renewable fossil fuel resources. In 1950, global plastic production began to rise, leading to its widespread use in daily life. Due to its high versatility, featuring low density, low thermal and electrical conductivity, corrosion resistance, affordability, durability, and high stability, plastic has become an irreplaceable material in many sectors, particularly packaging, building and construction, medical technology, and textiles. Therefore, from 1950 to 2024, global plastic production grew nearly 215 times, exceeding 430,9 million Mt worldwide by 2024, with PE (including LDPE and HDPE), polypropylene (PP), and PVC being the most widely applied plastic polymers, accounting for 26%, 19%, and 12.8%, respectively (PlasticsEurope, 2025).

While plastic provides numerous advantages for industrial purposes, its properties, such as durability and stability, have become a global environmental challenge in the current century. Plastics contain resistant functional groups and persistent covalent bonds, making their complete mineralization in the natural environment require hundreds of years (Zhang et al., 2021). However, over time, due to environmental factors (temperature, UV and VIS irradiation, microorganisms), plastic breaks down into smaller plastic items, known as microplastics. For the first time, the term "microplastics" was used by Thompson et al. (2004) to describe plastic items smaller than 20 μm found in coastal environments. Currently, microplastics are defined as any synthetic solid particles or polymer matrices that are insoluble in water and have a dimension from 1 μm to 5 mm, as suggested by the International Organization for Standardization (ISO) in 2023 (ISO 24187:2023, 2023)

Microplastics are categorized by their origin, physical dimensions, and chemical composition. First, microplastics are generally divided into primary and secondary groups. Primary microplastics are intentionally manufactured on a microscale and are commonly found as microbeads in personal care

products. PE constitutes the predominant polymer in these products. Another source of primary microplastics is plastic pellets used as raw materials in product fabrication, which may be released into the environment as waste. For instance, in 2012, around 4360 Mt of microbeads were used in the EU (Andrady, 2017). Because primary microplastics are intentionally manufactured, their production is considered easier to track and control than that of secondary microplastics. The use of primary microplastics is currently subject to regulatory control (Chapter *1.1.4*). Meanwhile, secondary microplastics are released through the fragmentation or weathering of larger plastic items and litter (plastic bags, food containers, fishing nets). The fragmentation of plastic items into microplastics is strongly influenced by different factors, such as mechanical abrasion, temperature, UV and VIS light irradiation, and biological processes. Although the generally accepted microplastic definition refers to microplastic particles with a size between 5 mm and 1 μm, there is a common classification regarding plastic dimensions into macroplastics (> 5 mm), mesoplastics (5–1 mm), microplastics (1 mm–1 μm), and nanoplastics (< 1 μm) (Priya et al., 2022). Based on molecular structure, synthetic polymers are categorized into two main groups: homocarbon-chain polymers and aromatic heterochain polymers (*Figure 1)*. Homocarbon-chain polymers consist of stable C–C bonds and are highly resistant to environmental factors. Meanwhile, aromatic heterochain polymers contain atoms other than carbon, such as O and N, within their main molecular chains, making them more prone to hydrolytic cleavage. The weathering and degradation of microplastics are strongly influenced by backbone composition.

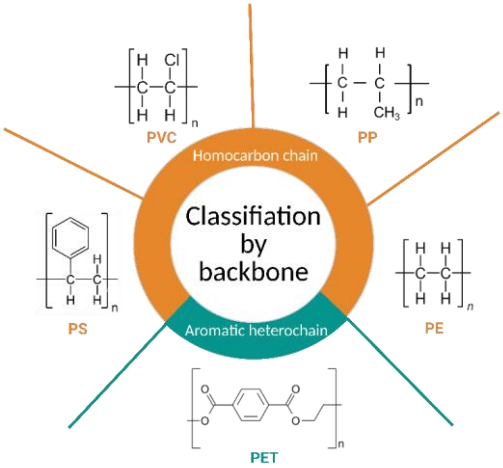

Figure 1. Classification of common microplastics based on the chemical structure of their polymer chain.

Microplastics pose a significant global threat due to their environmental presence and their role as vectors for hazardous substances, including persistent organic contaminants and heavy metals. Once microplastics are released into the environment, they can cause physical damage and bioaccumulation throughout the food chain. The amount of microplastics entering water systems is projected to increase from 20 Mt in 2016 to 53 Mt annually by 2030 (Walker and Fequet, 2023). Considering microplastics as an emerging contaminant, the following subsections will emphasize the key physical and chemical properties, sources and pathways of pollution, risks to the environment and human health, and existing pollution control regulations.

1.1.1. Physical and chemical properties

Plastic materials comprise up to twenty distinct organic polymers, derived from petroleum-based sources, each exhibiting varied characteristics and properties. The most relevant properties of microplastics for their behavior across different environments include size, shape, color, density, crystallinity, and chemical composition. In particular, these properties can determine their distribution in aquatic and terrestrial environments, their interactions with other pollutants and organisms, and their susceptibility to weathering and degradation.

The shape of microplastics is often linked to their origin and reflects the degree of weathering they have undergone in the environment. Frequently identified shape categories include fragments, pellets, fibers, films, foams, and granules. Fragments are characterized as irregular plastic pieces, often resulting from the degradation or weathering of larger plastic items. Fragments with sharp edges indicate a recent release into the environment, whereas smooth edges suggest prolonged environmental exposure and more extensive weathering. Pellets are typically known as primary microplastics, manufactured as raw materials for plastic products. Pellets can be found in various geometric morphologies, such as cylinders, disks, spherules, and ovoids. Another shape category widely found in the environment is fiber-type, consisting of thin, thread-like structures, often derived from textiles, and is primarily released during laundering. Film-type microplastics are most likely released into the environment from plastic bags or agricultural films. The shapes of microplastics, together with size and density, may determine their environmental fate (including sinking velocities in water bodies and tendencies to undergo biofouling) (Guo et al., 2024). In addition, certain microplastic shapes, such as fibers, are found to be more harmful to organisms than others. For example, fiber-type microplastics become entangled in the

digestive tract, forming strand aggregates that make them difficult to eliminate (Murray and Cowie, 2011).

Pigments are primarily incorporated into polymer blends during manufacturing to achieve coloration and enhance aesthetic appeal. Beyond aesthetics, pigments are used as inorganic additives to improve functional benefits such as UV resistance and flame retardancy. Once microplastics are introduced into the environment, their original colors change noticeably, making coloration a useful indicator of plastic aging. One of the most common changes is the "yellowing" or darkening of microplastics, which is attributed to photooxidation. In contrast to yellowing or darkening, some pigmented pellets may lose their original color over time, becoming lighter or bleached by weathering. The colors of microplastics found across many environments are highly variable and site-specific. However, certain colors are frequently reported as the most dominant, including black, white/transparent, and blue. The color of microplastics determines their ingestion by aquatic and terrestrial organisms. For example, species that prey on small zooplankton may specifically target microplastics that are colored white, tan, or yellow, which mimic the color of zooplankton (Wright et al., 2013). When organisms ingest colored microplastics, the hazardous substances may be released into the digestive tract, posing toxicological risks, or transferred to higher trophic levels.

Another important characteristic of microplastics is their density and crystallinity. Density primarily determines buoyancy and the initial vertical distribution of microplastics within the water column. As can be seen from *Table 1*, most plastics have densities close to that of water and therefore tend to float or remain suspended in the upper layers of the water column. For example, low-density polymers, such as PE and PP, float on the surface, while high-density polymers, such as PVC and polyethylene terephthalate (PET), sink to the sediment. This distribution is crucial as it determines how microplastics are transported in the environment, where they accumulate, and which marine organisms may ingest them. It is important to note that, over time, microplastic density can change due to biofouling, weathering, and degradation.

The density of a polymer is often linked to its crystallinity, as a higher degree of crystallinity generally results in higher density. For instance, LDPE has lower crystallinity (30-50%) compared to HDPE, which typically ranges from 80–90%. Crystallinity refers to the structural arrangement of the polymer chain, which can be crystalline, amorphous, or semi-crystalline (*Figure 2).* Semi-crystalline plastics such as PE, PP, and PET consist of microscale hard crystallites with an amorphous matrix. While crystallinity generally makes a

plastic tougher, extremely high levels can cause brittleness (Andrady, 2017). The degree of crystallinity influences the fragmentation and degradation processes of microplastics. Particularly, oxidative reactions occur mainly in the amorphous regions, as oxygen permeability is much lower in the crystalline domains. In addition, amorphous regions have larger gaps between molecular chains, making them more prone to sorb environmental pollutants or interact with other materials.

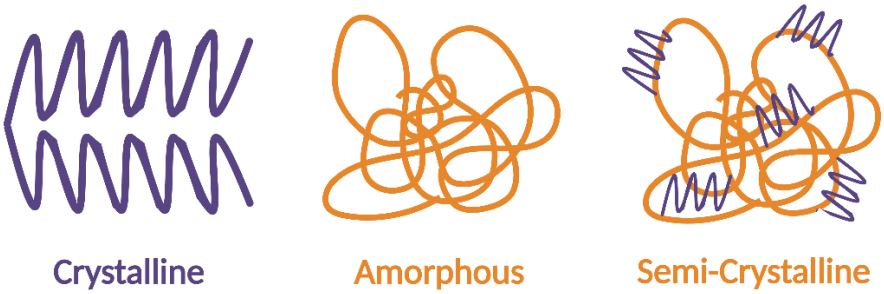

Figure 2. A schematic representation of polymer crystallization.

As previously indicated, microplastics are rarely pure polymers, as they are often compounded with various chemical additives to enhance their physical and chemical properties. Typical additives include plasticizers (e.g., bisphenol A (BPA) and phthalates), flame retardants (e.g., brominated compounds), stabilizers and antioxidants, and functional agents (e.g., metals and pigments). Most additives are low-molecular-weight and not chemically bound to the plastic matrix. Due to their weak interaction, they can easily leach into the environment throughout the plastic lifecycle. Most additives serve to preserve polymer integrity and provide resistance to weathering and degradation, such as stabilizers and antioxidants. However, the chemical nature of certain additives (e.g., BPA and phthalates) eventually can accelerate the fragmentation of microplastics (Sørensen et al., 2021). Although additives influence polymer properties, particular attention should be paid to the primary molecular chain of the polymer, as it determines its degradation behavior. Homocarbon-chain polymers consist of stable C–C bonds that are resistant to abiotic degradation, while aromatic heterochain polymers are more sensitive to degradation as they are prone to hydrolytic breakage. It should also be noted that some homocarbon-chain polymers are more susceptible to degradation than others. For example, PS contains aromatic phenyl rings, which act as light-absorbing chromophoric groups that accelerate UV reactions.

A detailed presentation of the properties of the selected plastics is provided in *Table 1*. Not all properties listed in the table are discussed in this work, since they are included to provide a broader overview.

Table 1. The physical and chemical characteristics of the selected types of plastics.

Polymer type	Chemical formula	*Density, g/cm^3	**Crystalinity, %	*Melting point, °C	**UV oxidation resistance	**Surface energy, MJ/m^2
LDPE	$[C_2H_4]_n$	0.92–0.93	30–50	110	Low	32.4
HDPE	$[C_2H_4]_n$	0.94–0.97	80–90	130	Low	32.4
PP	$[C_3H_6]_n$	0.89–0.94	30–50	160	Low	33.0
PS	$[C_8H_8]_n$	1.00–1.11	0–5	240	Mod.	40.6
PVC	$[C_2H_3Cl]_n$	1.20–1.45	5–15	100	Good	41.0
PET	$[C_{10}H_8O_4]_n$	1.37–1.45	10–30	260	Good	45.1

* Priya et al., 2022

** Andrady et al., 2017

1.1.2. Pollution across different environments

Improper plastic waste management is a primary driver of the introduction of large quantities of plastic into the environment, where it eventually fragments into microplastics. In 2015 alone, it was estimated that between 60 and 99 million Mt of plastic was improperly disposed of worldwide, while projections indicate that by 2060, mismanaged plastic waste will exceed 200 million Mt (Geyer et al., 2017; Fayshal, 2024).

Once microplastics enter the environment, they become highly mobile and can travel across various ecosystems. Given their diverse sources and numerous transport pathways, microplastics have been detected worldwide, even in remote areas such as the Arctic and deep-sea trenches (Wu et al., 2019). Surface runoff, precipitation, and riverine transport are the primary routes for transferring microplastics from land to water bodies. For example, rivers carry an estimated 1.15–2.41 million Mt of plastic into the ocean annually (Lebreton et al., 2017). Buoyant microplastics float on the surface of water bodies and can therefore be transported over long distances by ocean currents, winds, and tides. Meanwhile, microplastics with higher density, aggregated with denser particles such as clay, or contaminated by microorganisms, can move vertically through the water column and reach deep-sea sediments. Recent studies suggest that the ocean floor contains between 3 and 11 million Mt of plastic pollution (Zhu et al., 2024). Another

typical transport pathway is through the atmosphere, as small microplastics from landfills or urban streets can be blown into the air and travel long distances before being deposited back onto land or into the ocean via atmospheric fallout. A recent study using aircraft sampling within and above the planetary boundary layer found microplastics that air-mass trajectories suggest had travelled over 1000 km before deposition (González-Pleiter et al., 2021). In terrestrial environments, microplastics are primarily transported vertically by soil organisms such as earthworms.

WWTPs serve as a critical link between human activity and the environment in the context of microplastic pollution. Although some WWTPs can effectively remove microplastics, the massive volume of wastewater processed daily prevents the capture of many small microplastics, resulting in the release of large numbers of microplastics into freshwater systems. For example, Northern Italy's largest plant releases approximately 160 million microplastics into surface waters each day, despite achieving 84% removal of microplastics (Magni et al., 2019). Similar patterns were identified in the Estonian WWTPs. A study of six Estonian WWTPs reported overall removal efficiencies of up to 99.8%. Despite their high efficiency, these six plants collectively discharge approximately 97 million microplastic particles per day into water bodies that connect to the Baltic Sea (Ayankunle et al., 2025). Meanwhile, a study conducted at Lithuanian secondary WWTPs reported a removal efficiency of up to 63% for microplastics. As a result, the concentration of microplastics found in effluent ranged from 744 MP/L to 1244 MP/L (Uogintė et al., 2022). Furthermore, microplastics in wastewater are primarily removed through their capture and accumulation in sewage sludge. The agricultural utilization of sewage sludge effectively returns most of the microplastic content to the environment. Therefore, implementing effective microplastic degradation technologies is a crucial step in addressing global microplastic pollution.

In the terrestrial environment, plastic films are recognized as the predominant source of pollution. Plastic films pose a long-term environmental threat because they take more than 300 years to fully degrade under typical soil conditions (Ohtake et al., 1998). Previous studies have found that approximately 163 particles/cm^2 of microplastics are released into the soil from plastic films, with sizes ranging from 0.02 to 0.10 mm, after exposure to natural summer sunlight for 70 days (Yang et al., 2022). This has led to extreme microplastic contamination, exceeding 2000 particles/kg in southern Spain and reaching 324.5 kg/ha across 19 provinces in China (Huang et al., 2020; van Schothorst et al., 2021). The presence of microplastics in agricultural soils negatively impacts soil health by altering soil structure,

changing nutrient dynamics, and disrupting microbial diversity, ultimately affecting plant growth. In addition, this terrestrial pollution is a major contributor to marine pollution, as land-based sources account for roughly 80% of all plastic waste in the marine environment (Osman et al., 2023).

1.1.3. Adverse impact of microplastics

Microplastics pose multiple risks across global ecosystems, affecting the environment, wildlife, and human health. Due to their large specific surface area and hydrophobic nature, microplastics act as major carriers of environmental pollutants, including heavy metals and hydrophobic organic toxins, transporting them across different ecosystems. Microplastics in the environment can be ingested by a wide range of organisms, including species commonly consumed by humans.

Water organisms typically ingest microplastics by mistaking them for prey or by passively ingesting them during normal feeding behaviors, such as mussels and oysters (Megha et al., 2025). Because microplastics are similar in size to sediment and plankton, these particles are easily consumed by various low-trophic-level feeders and move through the food web via trophic transfer. The risks associated with this ingestion are both physical and chemical. Physical harm includes internal abrasion and clogging of the digestive system or feeding appendages, resulting in reduced food intake (Wu et al., 2019). In fish, microplastics can cause intestinal lesions, including cracking and splitting of villi (Megha et al., 2025). In addition, the leaching of toxic additives (phthalates, stabilizers) causes biological stress, including reduced growth and reproduction, neurotoxicity, oxidative stress, and severe liver damage, such as cellular necrosis (Iftikhar et al., 2024).

Human exposure to microplastics occurs through ingestion, inhalation, and dermal contact. It is important to note that research on microplastics in humans remains limited compared with extensive studies on aquatic organisms. However, previous studies have reported potential negative health impacts on humans. Microplastics deposited in the alveolar region of the lungs can trigger inflammatory reactions and disrupt cellular processes (Jung et al., 2025). In addition, small microplastics can translocate through biological barriers to reach secondary tissues and organs, including the blood, digestive tract, and liver. Deng et al. (2017) suggested that microplastics can disrupt energy and lipid metabolism and induce oxidative stress. Previous reports linked microplastic exposure to chronic conditions such as asthma, cardiovascular diseases like hypertension, and adverse impacts on reproductive health due to hormonal imbalances (Abbas et al., 2025).

1.1.4. Regulatory framework and policies

Growing concern over microplastic pollution has driven the development of new regulations and policies targeting plastic waste management and restricting the intentional addition of microplastics to products. As shown in *Table 2,* strategies adopted for microplastic mitigation differ across countries, incorporating both governance models and market-based approaches (Sayam et al., 2026).

Table 2. Overview of key international regulations and policies on microplastic pollution.

Region/Country	Regulation	Year	Target
USA	Microbead-Free Waters Act	2015	Ban on microbeads in wash-off cosmetic products
Europe	HELCOM (Baltic Sea Action Plan)	2015; Updated: 2021	To reduce and prevent marine litter, including microplastics
France	Microbeads regulation 2016/543/F	2016	Restriction of microplastics in cosmetics and personal care products
UK	The Environmental Protection (Microbeads) Regulation 2017/353/UK	2017	Ban on microbeads in rinse-off cosmetics (toothpaste, shower gel, scrubs)
Canada	Microbeads in toiletries regulations	2017	Official prohibition on the sale, manufacture, and import of toiletries that contain microplastics
EU	Single-Use Plastic Directive (EU) 2019/904	2019	To prohibit the placing on the market of products made of oxo-degradable plastic and restrict certain single-use items (like cotton bud sticks)
Ireland	The Microbeads Prohibition Act	2019	Ban microplastic beads in households and cleaning products
EU	Commission Regulation (EU) Directive 2023/2055	2023	Restriction of microplastics intentionally added to products.
EU	Urban Wastewater Treatment Directive (EU) 2024/3019	2024; Revised: 2026	To achieve a minimum average removal efficiency of at least 80% of microplastics from urban wastewater

Since 2015, regulatory tendencies have shifted toward targeted bans on primary microplastics and broader strategies for plastic waste management. A major wave of national legislation began with the USA "Microbead-Free Waters Act" of 2015, which prohibited microbeads in rinse-off cosmetics and personal care products (Microbead-Free Water Act of 2015, 2015). Meanwhile, in Europe, the Baltic Sea Action Plan (HELCOM) has introduced a regional action plan targeting microplastic pollution, focusing on recommendations for legal instruments, the development of microplastic-free

formulas, and the substitution of microplastics in personal care products (HELCOM, 2021). Between 2016 and 2018, microbeads were restricted in the rinse-off cosmetic products in France, the UK, Sweden, the Netherlands, Taiwan, South Korea, New Zealand, and Canada (Munhoz et al., 2022). However, only personal care products were addressed, while microbeads and other microplastics used in abrasive applications, such as plastic blasting and car molding, remained unregulated. Later regulatory and legislative development expanded their scope to include a broader category of microplastics. As follows, the EU Single-Use Plastics Directive (2019) was established to reduce secondary microplastics by targeting their macroplastic sources and emphasizing a circular economy (Directive (EU) 2019/904, 2019). In 2023, Commission Regulation (EU) 2023/2055 further restricted the intentional addition of microplastics to leave-on cosmetics, fertilizers, detergents, waxes, air care products, and agricultural products (Commission Regulation (EU) 2023/2055, 2023). The latest regulation, the Urban Wastewater Treatment Directive 2024/3019 (2024), adopted by the European Parliament, requires achieving a minimum average removal efficiency of 80% for microplastics from urban wastewater by 2045 (European Parliament and Council of the European Union, 2024).

While global regulations and policies are critical for reducing new inputs of microplastics, they cannot remove the vast amounts already present in the environment. It is important to note that mitigating microplastics requires not only prevention but also the implementation of removal technologies.

1.2. Removal technologies for microplastics

The management of microplastic pollution involves a wide range of technological approaches for implementation in WWTPs to enhance microplastic capture rates and ensure the safe disposal of residues. These methods are primarily categorized into four groups: conventional physicochemical treatments (filtration), advanced oxidation technologies, biotechnological approaches (biological degradation), and thermal conversion systems (Sanoja-López et al., 2026). The most widely employed methods are represented in *Figure 3***.**

The conventional treatment processes rely on well-established approaches such as membrane filtration (microfiltration, ultrafiltration, nanofiltration, reverse osmosis), coagulation-flocculation to aggregate particles, and adsorption using porous sorbents such as biochar (BC), activated carbon, or zeolites. Although these methods achieve removal

efficiencies of 85–99%, they have limitations, including the inability to remove microplastics smaller than 100 µm, the transfer of microplastics via sludge, and high maintenance and energy costs. To address these limitations, advanced oxidation technologies such as ozonation, photo-Fenton processes, photocatalysis, and electrochemical oxidation are employed. These oxidation technologies utilize ROS to chemically mineralize plastic polymers. Biotechnological approaches use biological systems, such as enzymatic or microbial degradation. While it is considered a sustainable approach, it has slow kinetics and is limited mostly to ester-containing polymers (PET, PLA). Finally, thermal conversion strategies, such as catalytic pyrolysis and gasification, can be applied to wastewater-treatment sludge to convert retained microplastics into energy resources (e.g., syngas). It is important to note that, typically, in order to achieve effective microplastic removal, a few treatment strategies are combined.

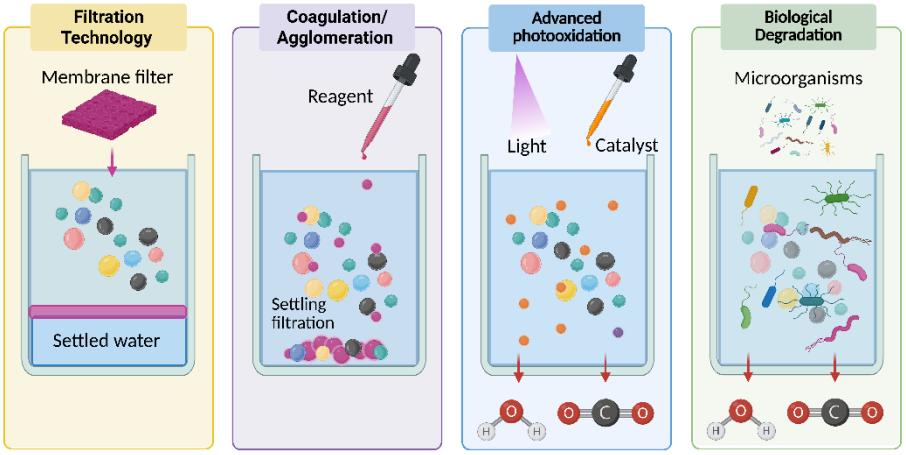

Figure 3. A schematic representation of the most widely used methods for microplastic removal.

Compared with other removal technologies, photocatalytic degradation is a sustainable and highly efficient method for microplastic remediation. This approach has demonstrated substantial efficacy in degrading various polymers, including PE, PS, PET, and PVC (Surana et al., 2024). The process facilitates extensive physicochemical transformations, such as weight reduction, alterations in morphology and polymer chains via oxidation and cross-linking, reduced crystallinity, and increased surface hydrophilicity. Unlike other advanced removal methods, photocatalytic degradation not only captures microplastics but also induces their mineralization, preventing secondary contamination.

1.2.1. Photocatalytic degradation

The photocatalytic degradation of microplastics is typically categorized into solid-phase and aqueous-phase approaches, each defined by the reaction environment and the interaction between the catalyst and the polymer. Both approaches have been extensively reported in previous studies, with considerably varying degradation efficiencies (Noor et al., 2024).

The solid-phase reaction is designed to replicate open-air conditions in which plastic waste is directly exposed to light irradiation. In this approach, photocatalysts are incorporated directly into the polymer matrix to create a composite film. In preparing such a composite, plastics are dissolved in solvents such as cyclohexane before the addition of a catalyst. Degradation occurs through direct exposure of the plastic to photocatalytic material dispersed within the polymer. The generated ROS diffuses into the matrix, abstracting hydrogen atoms from the polymer chain, thereby creating new carbon-centered radicals that eventually lead to chain scission (Noor et al., 2024). Since the solid-phase ensures direct contact between microplastics and catalysts, it contributes to efficient charge-carrier transfer. From a practical point of view, it simplifies post-degradation assessment, as catalysts do not need to be separated from the medium. In addition, solid-phase reaction prevents secondary contamination of water bodies (Wang et al., 2022). However, in the absence of an aqueous medium, the reaction may be limited by mass transfer, resulting in lower degradation rates than in aqueous-phase reactions.

The aqueous-phase reaction involves water, and it is intended to mimic wastewater treatment or natural water bodies. Microplastics are suspended as particles in the liquid or immersed as a film in water containing a catalyst. Degradation in aqueous-phase reaction is mainly driven by the generation of hydroxyl radicals in the bulk solution. The presence of water enhances mass transfer between microplastics and catalysts. In addition, it allows catalyst recovery through filtration or centrifugation. However, the post-degradation analysis poses new challenges for separating microplastics from catalyst NPs. Furthermore, there is a risk of secondary contamination if the catalysts leach into treated water.

Recent studies have reported the complete degradation of microplastics under aqueous-phase conditions across various plastic types, including polyester (PES), PE, and polyamide 66 (PA66) (He et al., 2023; Wang et al., 2025). In addition, high mass loss of microplastics was achieved in the aqueous-phase reaction, particularly by controlling solution pH and temperature. For instance, Ariza-Tarazona et al. (2020) found a 71.77% mass

loss of HDPE. Similar results were also reported by Ningsih et al. (2024), who achieved a 74% mass loss in PE films. On the contrary, some studies have observed relatively high mass loss of microplastics in solid-phase experiments due to direct contact between the polymer matrix and the catalyst. For example, Lu et al. (2025) achieved a mass loss of 58.30% in an LDPE film containing 5% TiO_2 using a solid-phase approach. However, other studies have shown lower degradation efficiencies under solid-phase conditions, with reported values of 21.3% for PE/TiO_2&MnO_2 (Kovinchuk et al., 2023) and 17.30% for LDPE (Kaewkam et al., 2022).

While solid-phase reactions provide simplified quantification and avoid secondary contamination, aqueous-phase systems offer better mass transport and more accurately reflect remediation of microplastics in aquatic environments.

1.2.2. Critical parameters affecting photocatalytic degradation

Photocatalytic degradation of microplastics is constrained by practical challenges arising from dependency on reaction conditions. Mainly, operational parameters govern ROS generation and overall reaction kinetics. Light-related factors (intensity, wavelength, and duration of exposure) are the primary drivers of semiconductor excitation and the subsequent separation of electron-hole (e^-/h^+) pairs (Kaewkam et al., 2022). The chemical environment, particularly pH and ionic strength (IS), further determines photocatalytic degradation performance, as these parameters can alter the catalyst's surface charge and its adsorption affinity for microplastics. Another critical reaction condition is the optimal catalyst loading, which should maximize the number of active sites on the catalyst surface while avoiding light scattering (Abdel-Khalek et al., 2018).

Although many other parameters affect photocatalytic degradation, such as temperature, oxygen availability, initial microplastic concentration, and water matrix components, this work will focus on UV irradiation, catalyst loading, pH, and ion strength.

1.2.2.1. Irradiation duration, light intensity, and wavelength

The efficiency of photocatalytic degradation of microplastics is strongly influenced by light intensity and wavelength. First, light intensity affects the generation of ROS and the behavior of e^-/h^+ pairs, while wavelength determines the energy available for bond cleavage and the activation of the photocatalyst.

Numerous studies have explored the photocatalytic reaction systems operating under UV and visible light irradiation. Kaewkam et al. (2022) found that UV-C (254 nm) is significantly more efficient than UV-A (325 nm) in degrading microplastics such as LDPE because it has higher energy, which is required to break C–H bonds. To date, the mass loss of LDPE under UV-C exposure has reached 17.04%, while the maximum mass loss under UV-A was only 4.95% over a period of 9 days. Furthermore, it was recently found that, under natural conditions at lower light intensity, the carbonyl index (CI) in HDPE was lower than under artificial weathering at higher light intensity (Fairbrother et al., 2019). Although shorter wavelengths and higher light intensities enhance microplastic degradation, they notably increase process costs and environmental impacts. In recent years, a growing number of studies have focused on strategies for improving microplastic degradation under UV-A and visible light.

The photocatalytic degradation efficiency of microplastics typically increases with time. The photocatalytic degradation involves complex, multistep reactions that begin with the generation of ROS, which must first attack the long polymer chains and then eventually lead to chain cleavage into smaller oxygenated products. The increase in degradation efficiency primarily corresponds to enhanced interaction between the catalyst and microplastics. Only a few previous studies have reported the complete degradation of microplastics, suggesting that complete mineralization requires extended irradiation time. For example, He et al. (2023) reported a complete mineralization of PE, PES, and PP in 480 h, 625 h, and 816 h, respectively.

1.2.2.2. Catalyst loading

The loading of the catalyst is important in determining the efficiency of microplastic degradation as it controls the availability of active sites and the dynamics of photon absorption. Increasing the catalyst dosage generally enhances degradation by providing more active surface sites and facilitating the generation of hydroxyl radicals. However, if the catalyst concentration exceeds the optimal value in the degradation system, degradation efficiency can notably decrease due to light scattering and particle agglomeration (Abdel-Khalek et al., 2018). Thus, determining the optimal catalyst loading level is crucial for maximizing the adsorption of available photons.

Previous studies reported on different optimal loading levels of catalysts. Tan et al. (2023) suggested that the optimal loading of Zn-GO for LDPE degradation is 1 g/L. Meanwhile, a higher catalyst loading was required in a photocatalytic system using TiO_2-GO, with the highest LDPE mass loss

observed at a catalyst concentration of 2 g/L (Uogintė et al., 2023). A slightly higher Ag-TiO_2 catalyst loading (3 g/L) was required for efficient degradation of PA66 (Wang et al., 2025). Overall, the optimal catalyst loading is system-specific and should be carefully considered to maximize catalytic performance.

1.2.2.3. pH of the solution

The pH level is an important factor that determines how microplastics degrade and interact with the photocatalyst, primarily through changes in electrostatic interactions. In general, photocatalyst surfaces are negatively charged under alkaline conditions and positively charged under acidic conditions. Meanwhile, many common microplastics (PE, PP, PS) have a negative charge in aqueous solution, therefore, under acidic conditions, the electrostatic attraction is likely to occur between the positively charged catalyst and microplastics. This enhanced adsorption also promotes stronger interactions between microplastics and positively charged holes (h^+) or generated ROS, such as hydroxyl radicals, thereby inducing polymer chain degradation. On the contrary, in an alkaline solution, both microplastics and catalysts develop negative surface charges, promoting repulsive forces that weaken adsorption capacity.

Previous studies have reported that various catalysts showed improved photocatalytic performance under acidic and neutral conditions. For example, Ariza-Tarazona et al. (2020) compared the degradation efficiency of HDPE using C,N-TiO_2 at pH levels of 3, 7, and 11, indicating the highest degradation efficiency at pH 3. Meanwhile, during the degradation of PET and PVC in the presence of kaolinite (Kao) and montmorillonite (MMT), the optimal pH was neutral (pH 7) (Ding et al., 2022). Adjusting the pH of the reaction solution has been shown to effectively control microplastic degradation performance.

1.2.2.4. Ionic strength of the solution

IS influences the behavior of both microplastics and the catalyst. In the context of microplastics, IS governs colloidal stability and aggregation kinetics. Typically, as the solution's IS increases, microplastics become less stable and more prone to aggregation. This is due to the increased hydrodynamic diameters of microplastic particles, which lead to larger particle clusters (Lu et al., 2018). In addition, divalent cations (Ca^{+2}, Mg^{+2}, Ba^{+2}) influence aggregation more than monovalent cations (Na^+, K^+) (Li et al., 2018). Furthermore, increasing IS leads to a negative zeta potential in

microplastics. Once microplastics have a negative zeta potential, the repulsive forces that normally keep the particles dispersed are reduced, allowing van der Waals forces to dominate and cause aggregation (Lu et al., 2018). The aggregation of microplastic particles reduces the number of available surface sites for reactions with catalysts and ROS, leading to a less uniform distribution in the reaction solution and lower degradation efficiency.

Similarly, increasing IS can influence the surface behavior and reactivity of the catalyst. For example, at higher IS levels, TiO_2 NPs exhibit greater compression of the electrical double layer, which reduces the repulsive forces between NPs and consequently promotes their aggregation (Zhu et al., 2014). Once larger NPs clusters form, they reduce the active surface area available for catalytic processes. While solution pH control can improve photocatalytic reaction efficiency, IS is likewise an important parameter, especially when analyzing microplastic and photocatalyst behavior in the solution.

1.3. TiO_2-based nanomaterials for microplastic degradation

A wide range of catalysts, including ZnO, WO_3, CuO, Fe_2O_3, SiO_2, and SnO_2, have been studied for the degradation of organic pollutants. However, TiO_2 NPs remain the most effective and established metal-oxide photocatalysts (Ahmed et al., 2025). It is relatively inexpensive compared with other materials employed in water treatment processes and can be easily synthesized under standard laboratory conditions. Moreover, a key advantage of TiO_2 over semiconductors such as ZnO for water treatment is that it does not form toxic decomposition products (Malato et al., 2009). TiO_2 can experience changes in oxidation state while maintaining its crystalline structure, making it an attractive material for photocatalytic applications. TiO_2 in the form of nanostructures (NPs, nanotubes, nanorods) is widely used in photocatalytic systems due to its high surface-area-to-volume ratio, higher reaction rates, and non-toxicity. In addition to their excellent catalytic properties, TiO_2 nanomaterials are also used in CO_2 reduction, antibacterial activity, water splitting, lithium-ion batteries, air purification, solar cells, paints, cosmetics, drug delivery, and more.

However, TiO_2 nanomaterials have several limitations when used as photocatalysts for water treatment. Its applications remain limited because it operates only within a narrow UV range ($\lambda < 400$ nm) and absorbs less than 5% of the available solar and indoor light, which is associated with its wide band gap (anatase ~3.2 eV) (Wang et al., 2020). In addition, TiO_2 also suffers from a high recombination rate of photogenerated electrons (e^-) and h^+, which

reduces the number of ROS available for the successful degradation of organic pollutants (El Mchaouri et al., 2025). Another drawback is the low affinity for organic contaminants, including microplastics, which limits interaction between the TiO_2 surface and these materials, resulting in a slow photocatalytic degradation rate. Furthermore, despite their widespread use in photocatalytic applications, TiO_2 NPs tend to agglomerate within such systems. The agglomeration of TiO_2 NPs reduces surface area and the number of active sites while increasing light scattering, ultimately leading to less efficient degradation. When TiO_2 is used as a slurry, the recovery and regeneration of TiO_2 NPs are additional challenging tasks. The discussed limitations of TiO_2 in the photocatalytic system are summarized in *Figure 4*.

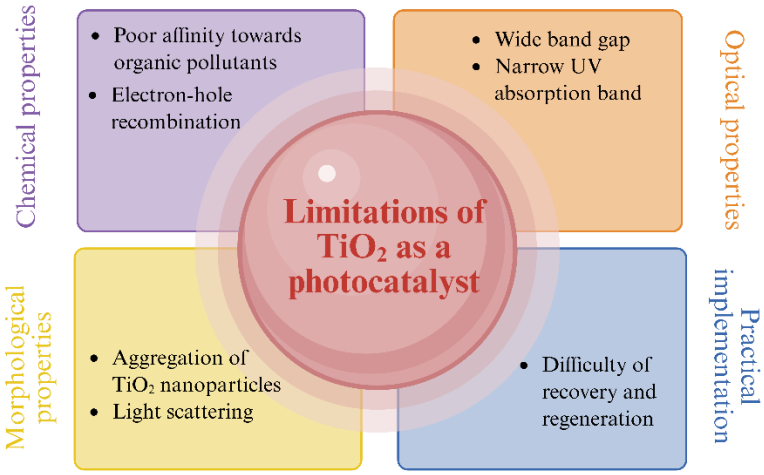

Figure 4. Limitations in the application of TiO_2 NPs for the photocatalytic degradation of organic pollutants.

To overcome these limiting factors and improve the photocatalytic properties of TiO_2, researchers are focusing on approaches such as surface modifications and dye sensitization, morphology control, nanocomposite formation, and metal doping. In this work, nanocomposite formation and metal doping were chosen to enhance the photocatalytic properties of TiO_2 NPs and improve the photocatalytic degradation of LDPE microplastics. In the following subsections, a detailed analysis of the properties of bare TiO_2 NPs, nanocomposites based on TiO_2 and clay minerals (Kao and MMT), and metal-doped TiO_2 will be presented.

1.3.1. Pure TiO_2 NPs

TiO_2 is an inorganic compound typically found in soils, sands, rocks, ores, and dust fields. It appears in three crystalline forms: anatase, rutile, and brookite (*Figure 5)*. Each crystallographic phase exhibits distinct properties and photocatalytic performances.

Anatase crystals commonly exhibit a thin, tabular, or platy structure, often with surface striations. Optically, the anatase phase is transparent and has a relatively high refractive index. In addition, the formation of the anatase phase occurs at temperatures below 600 °C, resulting in increased surface area and more abundant active sites for catalytic reactions, making the anatase phase even more favored for photocatalytic degradation processes (El Mchaouri et al., 2025).

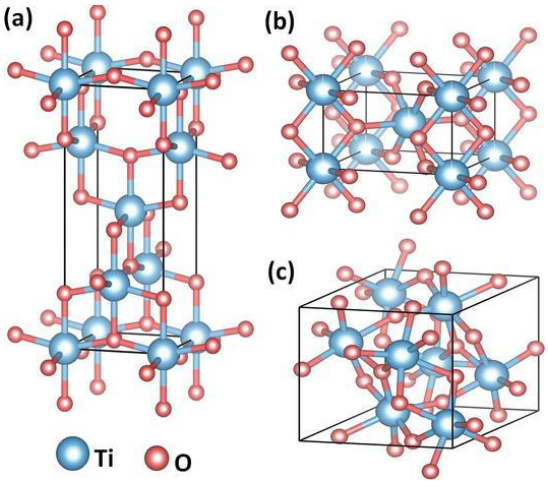

Figure 5. The schematic representation of TiO_2 crystal structures (a) anatase (tetragonal), (b) rutile (tetragonal), and (c) brookite (orthorhombic). Reproduced from Siddiqui (2020).

The rutile phase commonly forms needle-like crystals alongside other materials, giving them a distinctive appearance. These crystals have a high luster and can vary in color depending on impurity levels. Besides, the rutile phase is known for its inherent piezoelectric and ferroelectric properties, as well as the highest refractive index of ~2.8 compared to anatase and brookite (Goutham et al., 2022).

Both anatase and rutile have a tetragonal lattice, while brookite has an orthorhombic structure. The composition of anatase and rutile contains chains of TiO_6 octahedra in which each Ti^{4+} cation is surrounded by six O^{2-} anions. A calcination temperature of 500 °C is considered optimal for the formation of both the anatase and rutile phases of TiO_2 and for promoting a narrow

particle size distribution and high crystallinity (Kim et al., 2021). The anatase phase differs from rutile by having a longer Ti-Ti distance and shorter Ti-O bond length, resulting in a more elongated octahedral arrangement. Inter-octahedral bonds also vary: in rutile, each TiO_6 octahedron is linked to ten neighboring units, whereas in anatase it is connected to only eight.

Brookite crystals exhibit elongated prismatic or tabular morphologies. The average band gap of brookite is approximately 3.4 eV. Brookite is the most difficult TiO_2 crystalline phase to synthesize in its pure form, without the abundance of the anatase and rutile phases. Several factors, such as pH, surface energy, and particle size of the synthesized materials, can influence the phase transformation of TiO_2. Thermal treatment is one of the key approaches to control anatase and rutile formation. However, it remains unclear whether the anatase phase first transforms into brookite or vice versa before converting to rutile, although transformation enthalpies indicate that the thermodynamic stability of TiO_2 phases is ranked as anatase < brookite < rutile (Szołdra et al., 2023).

To date, anatase and rutile TiO_2 crystallites are the most widely used in photocatalytic applications. The lifetimes of photogenerated e^- and h^+ are longer in indirect band gap semiconductors, such as anatase, than in direct band gap materials, such as rutile. Furthermore, the relatively low average effective mass of photogenerated charge carriers in anatase enables efficient charge transfer to the surface and a lower e^-/h^+ recombination rate than in other TiO_2 crystallites (Zhang et al., 2014). On the other hand, a previous study indicated that a mixed-phase TiO_2 containing anatase and rutile exhibits the highest photoactivity under UV irradiation, as the presence of two phases reduces the recombination rate of charge carriers (Kaewkam et al., 2022).

1.3.2. Basic principles of TiO_2 NPs as photocatalysts

TiO_2 has been widely used as a photocatalyst because of its ability to induce a variety of surface redox reactions. In general, photocatalytic processes occurring on the TiO_2 surface proceed through five stages: (1) photoexcitation, which involves photon absorption and the generation of charge carriers, (2) charge carrier diffusion, (3) trapping at the surface or bulk sites, (4) e^-/h^+ recombination, and (5) oxidation reactions (*Table 3*) (Armaković et al., 2023).

Table 3. Key reactions involved in TiO_2 excitation and ROS formation.

Reactions	
$\mathbf{TiO_2 + h\nu \rightarrow e^- + h^+}$	(1)
$\mathbf{e^-_{CB} \rightarrow e^-_{TR}}$	(2)
$\mathbf{h^+_{vB} \rightarrow h^+_{TR}}$	(3)
$\mathbf{e^-_{TR} + h^+_{vB}(h^+_{TR}) \rightarrow e^-_{CB} + heat}$	(4)
$\mathbf{OH^- + h^+ \rightarrow OH^{\cdot}}$	(5)
$\mathbf{O_2 + e^- \rightarrow O_2^{\cdot -}}$	(6)
$\mathbf{O_2^{\cdot -} + OH^{\cdot} \rightarrow HOO^{\cdot}}$	(7)
$\mathbf{HOO^{\cdot} + e^- \rightarrow HO_2^-}$	(8)
$\mathbf{HOO^- + H^+ \rightarrow H_2O_2}$	(9)

Photocatalysis occurs on the TiO_2 surface when incident photons with energy greater than the band gap ($h\nu > E_g$) induces excitation from the valence band (VB) to the conduction band (CB) (Eq. 1). The phonon energies involved in this TiO_2 excitation process correspond to a wavelength of less than 400 nm. This results in the formation of e^-/h^+ pairs (Eq. 2, 3). Although photogenerated e^-/h^+ pairs typically last only a few nanoseconds, they can initiate redox processes on the TiO_2 surface. Subsequently, the generated charge carriers can either be separated and transferred to the surface to participate in redox reactions with organic and inorganic pollutants, or they may undergo recombination (Eq. 4), thereby decreasing the quantum yield of the photocatalytic reaction. It is important to note that on the TiO_2 surface, trapped electrons (e^-_{TR}) and holes (h^+_{TR}) have a slower recombination rate compared to those diffused in the bulk (El-Zohry et al., 2024). Furthermore, the photogenerated h^+ directly oxidize pollutants absorbed on the surface, initiating their degradation processes (Kim et al., 2014).

For most applications, the photocatalytic degradation reactions are performed in systems containing water, air, the target pollutant, and the photocatalyst. The absorbed OH^- and H_2O on the TiO_2 surface react with the positively charged h^+, generating hydroxyl radicals ($^{\cdot}OH$) (Eq. 5). Meanwhile, negatively charged electrons undergo a reaction with O_2, forming superoxide radical anion ($O_2^{\cdot -}$) and preventing the e^-/h^+ recombination. Further, $O_2^{\cdot -}$ radical may be protonated to generate hydroperoxyl radical ($HO_2^{\cdot}$) and eventually results in the formation of peroxide (H_2O_2) (Eq. 7-9). In addition, the presence of $HO_2^{\cdot}$ cotributes to the reduction of e^-/h^+ recombination on the

TiO_2 surface. This leads to an extended lifetime of h^+ carriers and increases their involvement in the photocatalytic reaction. The detailed overview of the TiO_2 excitation process and corresponding ROS formation is summarized in *Table 3*.

1.3.3. Natural materials containing nanocomposites

A wide range of natural materials is used for microplastic removal, particularly for adsorption studies, including cellulose- and polysaccharide-based nanomaterials, BC, chitosan, and zeolite (Li et al., 2026). For example, Wang et al., (2021) reported that the removal efficiency of 1.0 μm PS microspheres using BC was 25.89%. In comparison, Mg-modified magnetic biochar (Mg-MBC) and Zn-modified magnetic biochar (Zn-MBC) demonstrated significantly higher removal efficiencies of 98.75% and 99.46%, respectively. These findings emphasize the enhanced removal efficiency of microplastics, achieved with composites incorporating both natural materials and metal NPs.

Along with this, natural materials have attracted notable attention as photocatalyst carriers. The wide availability of natural materials offers key benefits, including low cost and environmental sustainability. Natural minerals serve as supports due to their high surface area and strong affinity for pollutant adsorption (Mishra et al., 2018). Although nanocomposite formation using natural materials is widely used for the removal of various organic pollutants (dyes, colorants, pharmaceuticals, antibiotics, pesticides), only a few studies focus on their application to the photocatalytic degradation of microplastics. Ariza-Tarazona et al. (2020) synthesized a bio-inspired C,N-doped TiO_2 photocatalysts using carbon and nitrogen derived from the extrapallial fluid of *Mytilus edulis*. This approach enhanced the visible-light photocatalytic activity as C doping improved light absorption, while N doping narrowed the band gap by introducing localized states that enable visible-light excitation. In a later study, Zhang et al. (2024) synthesized a g-C_3N_4/TiO_2 composites supported on waste cotton-based activated carbon. The formation of nanocomposites enhanced the visible-light absorption of TiO_2, broadened its spectral response range, and improved e^-/h^+ separation, ultimately achieving a PE mass loss of up to 68%. Further examples of improved TiO_2 photochemical properties through the synthesis of TiO_2-natural-material-based nanocomposites and their application to microplastic photocatalytic degradation are summarized in *Table 4*.

Table 4. Reported TiO_2-natural material nanocomposites used for the photocatalytic degradation of microplastics.

Nanocomposite	Natural material	Improved TiO_2 properties	MPs type	Reaction conditions	Mass loss	Ref
N-TiO_2	extrapallial fluid (EPF) of mussels; protein	Reduced energy band gap (from 3.1 to 2.9); photocatalytic activity under visible light.	HD-PE	Irradiation at visible light; 27 W fluorescent lamp; photocatalysis time of 8 h; room temperature.	6.4%	(Ariza-Tarazona et al., 2019)
C, N-TiO_2	extrapallial fluid (EPF) of mussels, protein	Reduced e^-/h^+ recombination, improved photocatalytic activity under visible light, Increased surface area.	HD-PE	Irradiation at 428 nm; 50 W LED lamp; photocatalysis time of 50 h; pH 3, 7 and 11, and temperature of 0, 20 and 40 ± 2 ◦C.	71.77% (at pH 4)	(Ariza-Tarazona et al., 2020)
g-C_3N_4-TiO_2/waste cotton-based activated carbon (WCT-AC) composite	Cotton	Decreased energy band gap to 2.54 eV; improved visible light; enables e^-/h^+ separation.	PE	Irradiation at > 420 nm; 500 W xenon lamp; photocatalysis time of 200 h; pH of 7; system temperature of 25 ◦C.	67.58%	(Zhang et al., 2024)
GO/N-TiO_2	N	Decrease in crystallite size from 13.69 nm to 3.13 nm; reduced energy band gap to 2.6 eV; increased thermal stability.	PVC	Irradiation at 446 nm; natural room light conditions (tungsten lamp); pH of 4, 7, and 10; photocatalysis time of 180 min.	98.2% (at pH 4)	(Kaur and Kaur, 2025)

In recent years, clay minerals (bentonite, halloysite, zeolite, montmorillonite, kaolinite) have gained considerable attention due to their natural origin, availability, high surface area, and distinctive physical, chemical, and structural properties. Clay-based composites serve as adsorbents, catalyst supports, or catalysts for environmental remediation processes. The catalytic activity of clay minerals can be attributed to four key factors: Brønsted acidity, Lewis acidity, redox-active species, and transition metals or cations (Zou et al., 2022). In particular, clay composites incorporating semiconductors or metal NPs have demonstrated enhanced photocatalytic efficiency. The photocatalytic performance of metal NPs depends on particle size, morphology, and the nature of the support material. Their immobilization on clay supports, such as montmorillonite or other pillared interlayered clays, can improve photocatalytic activity. Besides, clay nanocomposites exhibit high thermal and chemical stability, enhanced flame-retardant properties, and extended lifetime.

Although clay minerals and clay-based composites are widely used in water treatment, only a limited number of studies have investigated their efficiency in microplastic removal. Li et al. (2020) studied the interaction of both negatively and positively charged microplastics with kaolinite clay, indicating that kaolinite clay can absorb microplastics on its surface through the formation of microplastic-clay heteroaggregates. Similarly, Huang et al. (2022) investigated the removal of microplastics in aqueous medium using Fe-kaolinite and Co/Mn-kaolinite nanocomposites. The results showed microplastic removal capacities of 13.68 $mg \cdot g^{-1}$ and 22.00 $mg \cdot g^{-1}$ for Fe-kaolinite and Co/Mn-kaolinite, respectively. Furthermore, Ding et al. (2022) have shown that clay minerals (kaolinite and montmorillonite) facilitate the photodegradation processes of PVC and PET microplastics, as these minerals increase the generation of $^{\cdot}OH$ and $O_2^{\cdot -}$ radicals actively involved in microplastic degradation. These studies highlight the potential application of clay minerals for the removal and degradation of microplastics. However, the mechanisms and interactions between microplastics and clay minerals remain poorly understood.

1.3.3.1. Kaolinite

Rocks rich in kaolinite are called kaolin, also known as china clay. Kaolinite, with a chemical formula $Al_2Si_2O_5(OH)_4$, is a 1:1 layered clay mineral composed of structural layers formed by two different sheets (Mishra et al., 2018). The layer is composed of a tetrahedral silica sheet and an octahedral alumina sheet, joined by shared oxygen atoms in their coordination

polyhedra (*Figure 6)*. The layer is asymmetric and therefore strongly dipolar, leading to dipole-dipole stacking interactions. In kaolinite, the 1:1 layers are electrically neutral. They are linked by hydrogen bonding between the basal oxygens of the tetrahedral sheet and the hydroxyls of the outer plane of the adjacent octahedral sheet. As a result, the layers interact in a face-to-face manner, stacking to form pseudo-hexagonal platelets consisting of approximately 50-150 layers, with thicknesses of 30-100 nm (Romero and Garg, 2022).

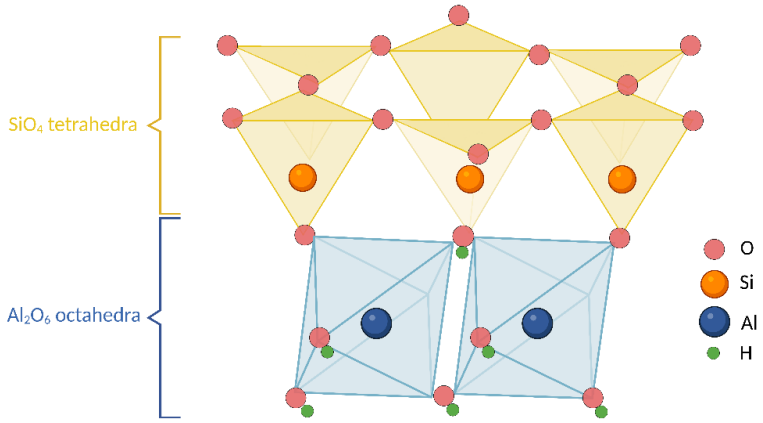

Figure 6. A simplified schematic representation of a kaolinite layer structure, showing the silica tetrahedral sheet and the alumina octahedral sheet.

Natural kaolinite has no charge as layers are stabilized by close hydrogen bonding, therefore it does not expand between layers and exhibits non-swelling characteristics under wet conditions. Kaolinite layers are strongly cohesive and stack with a basal spacing of 7.2 Å, which corresponds to one layer thickness and limits access to the interlayer space. Due to its unique layered structure, kaolinite has a low specific surface area of 5-40 m^2g^{-1} and a low capacity to absorb ions (Li et al., 2022). These kaolinite characteristics contrast with those of swelling 2:1 layered smectites, particularly montmorillonite, which is widely used in nanocomposites.

When kaolinite clay appears in aqueous medium, its particles develop oppositely charged surface regions, with a small permanent negative charge on the tetrahedral surface due to the minor isomorphic substitution within the tetrahedral sheet. Meanwhile, the octahedral surface carries a variable charge due to hydroxyl groups at its edges. Depending on pH, hydroxyl groups can be protonated or deprotonated, thereby creating positive or negative charges, respectively, corresponding to anion- or cation-exchange capacities. At pH 7, the cation exchange capacity of kaolinite varies between 3–15 meq·100 g^{-1}

and increases with increasing pH (Reinoso-Maset and Ly, 2016). The protonation of aluminol groups (Al-OH) on kaolinite occurs when the pH is lower than the point of zero net proton charge (PZNPC) (6.0 to 6.5) of the main edge site, resulting in a positively charged surface. On the other hand, when the pH exceeds the PZNPC of the main edge site, deprotonation of silanol (Si-OH) and aluminol groups occurs. This results in a negative charge at the edges, lowering the zeta potential of kaolinite and increasing the reactivity of the alumina groups. In addition, the hydroxyl groups on the octahedral sheet are less reactive than aluminol and silanol groups located on the broken edges. The main characteristics of kaolinite are summarized in *Table 5.*

Table 5. Main characteristics of clay kaolinite.

Characteristics	**Kaolinite**
Type	1:1
Basal spacing, Å	7.2
Swelling potential	Almost none
Specific surface area, m^2g^{-1}	5–40
Surface charge	pH-dependent
Cation-exchange capacity at pH 7, meq·100 g^{-1}	3–15

1.3.3.2. Montmorillonite

Montmorillonite ($(Na,Ca)_{0.33}(Al,Mg)_2Si_4O_{10}(OH)_2\cdot(H_2O)_n$) is a natural mineral that typically appears as the main component of bentonite clay. It primarily forms in low-oxygen environments, such as lakebeds and marine sediments, and is often associated with weathered volcanic rocks. Montmorillonite has a 2:1 layered structure, containing two silica tetrahedral sheets with a central alumina (or magnesium) octahedral sheet (Si-Al-Si) (Mishra et al., 2018). The tetrahedral sheets are composed of Si^{4+} cations coordinated by four oxygen atoms, and within the octahedral sheet, divalent (Mg^{2+}) or trivalent (Al^{3+}) cations are surrounded by six oxygen atoms (*Figure 7)*. The crystal sheets carry a negative charge due to isomorphic substitution, for example, Mg^{2+} or Fe^{2+} replacing Al^{3+} (Wang et al., 2021). The strength of the negative charge depends on the extent of atomic ionic substitutions. Meanwhile, the negative surface charge is compensated by interlayer cations, such as alkali metals (Li, Na, K, Rb, Cs, Fr) or alkaline-earth metals (Be, Mg, Ca, Sr, Ba, Ra). These interlayer cations bind the sheets together through electrostatic attractions. Montmorillonite typically contains 8-33 layers, with

each layer measuring roughly 1 nm in thickness. Other minerals, such as quartz, mica, muscovite, calcite, and feldspar, can be found in montmorillonite.

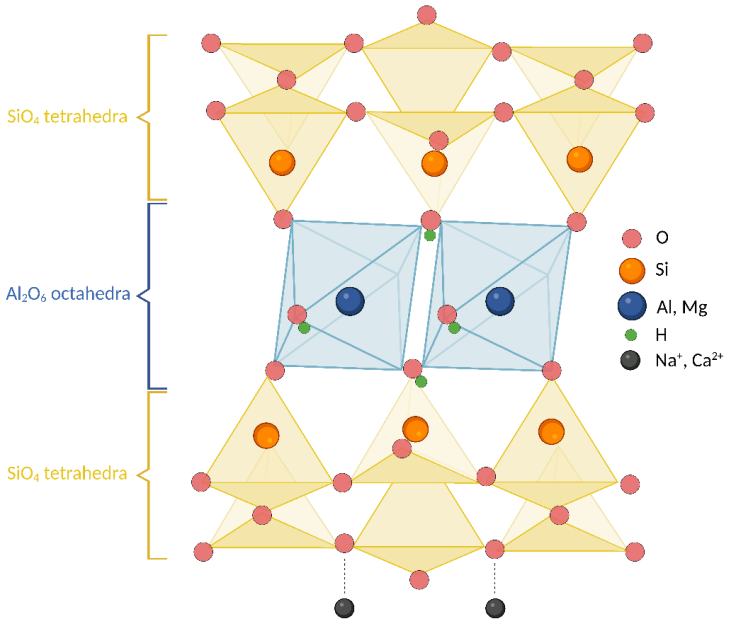

Figure 7. A simplified schematic representation of a montmorillonite layer structure, showing the alumina octahedral sheet situated between two silica tetrahedral sheets.

A weak interaction between oxygen atoms in the bottom tetrahedral sheet of one unit and the top sheet of a neighboring unit results in variable basal spacing ranging from 9.8 to 20 Å, which contains exchangeable cations and water. Because of the expansive properties of montmorillonite, these minerals have a notably higher specific surface area (up to 800 m^2g^{-1}). In contrast, non-expanding clay minerals, such as the previously discussed kaolinite, have much lower specific surface area. As a result, montmorillonite exhibits a high cation exchange capacity of 80–120 meq·100 g^{-1} (in neutral medium) and substantial swelling potential (Belbel et al., 2024). Although montmorillonite offers many favorable properties for application in different fields, it contains impurities, such as Fe^{2+} and Mg^{2+}, that limit its catalytic performance. These impurities may block the material's active sites, alter reaction pathways, or even cause unwanted side reactions.

Montmorillonite exhibits patch-wise charge heterogeneity, with oppositely charged surface regions. The basal surface has a permanent negative charge over a pH range of 2 to 12, arising from isomorphic substitution and is pH-independent (Zeng and Kobayashi, 2025). Meanwhile,

the edge surface contains amphoteric hydroxyl groups (Si-OH, Al-OH) whose protonation is strongly pH-dependent. At low pH, edges are positively charged, whereas at high pH, they are negatively charged (Gao et al., 2023). The protonation of Al-OH sites at the edges occurs when the solution pH is below the point of zero charge (PZC) of the edge hydroxyl groups (~6.5) (Tombácz and Szekeres, 2004). Further, an increase in pH enhances the contribution of negatively charged edge sites, thereby increasing cation exchange capacity. As pH increases, the concentrations of sodium and hydroxide ions in solution rise, enhancing ion adsorption on the mineral surface. This results in a thicker double layer and higher zeta potential. In comparison, kaolinite is less dependent on pH and IS than montmorillonite due to its non-expandable layers (da Silva et al., 2024). The key properties of montmorillonite are presented in *Table 6*.

Table 6. Main characteristics of clay montmorillonite.

Characteristics	**Montmorillonite**
Type	2:1
Basal spacing, Å	9.8-20
Swelling potential	High
Specific surface are, m^2g^{-1}	700-800
Surface charge	Basal surface: pH-independent Edge surface: pH-dependent
Cation-exchange capacity at pH 7, meq·100 g^{-1}	80-100

1.3.4. Metal-doped TiO_2

The metal doping process addresses major limitations of TiO_2 NPs, such as low solar absorption and a high recombination rate of photogenerated e^-/h^+ pairs. The metal doping process creates a new impurity level in TiO_2, resulting in a narrower band gap, enhanced visible-light absorption, and improved separation of photogenerated charge carriers.

The modification of TiO_2 through metal doping involves transition, rare-earth, and noble metals. Previous studies have shown that transition metals (Cr, Cu, Fe, Mn, Zn, V, W, Co, and Ru) influence the properties of TiO_2 NPs, including band gap energy, surface area, thermal stability, and particle size, thereby directly controlling their photocatalytic activity (Mogal et al., 2013). Transition-metal elements have partially filled d orbitals, which enable them to trap electrons and suppress charge-carrier recombination. Nevertheless, excessive doping of TiO_2 can create lattice defects that reduce

the transport of photogenerated charge carriers. Rare earth metals (Y, Sc, and fifteen lanthanoid elements), characterized by unfilled 4f and empty 5d orbitals, can also be employed as dopants in TiO_2 photocatalysts. These elements have the potential to reduce the recombination rate of charge carriers, increase TiO_2 light absorption, and form complexes with organic molecules by f-orbital (Shi et al., 2012). However, rare-earth-element doping can reduce the number of surface-active sites on TiO_2, thereby limiting its efficiency in degrading polymer chains and making it more effective against low-molecular-weight pollutants.

Another class of dopants for TiO_2 includes noble metals (Au, Pt, Ag, and Pd). These elements greatly enhance the photocatalytic activity of TiO_2 under both UV and visible light, primarily due to localized surface plasmon resonance (SPR). Although the use of noble metals for TiO_2 doping yields high degradation efficiency for organic pollutants, including microplastics, most of these elements are expensive and difficult to scale up. Among noble metals, silver is considered a cost-effective option for enhancing the visible-light absorption of TiO_2.

To date, a wide variety of metals have been studied for doping TiO_2 to enhance the photocatalytic degradation of microplastics. Although the photocatalytic degradation of microplastics strongly depends on their characteristics, chemical composition, and overall reaction conditions, previous studies suggest that metal-doped TiO_2 improves degradation efficiency, with reported values ranging from 9% to 100%. Recent studies on TiO_2 doped with various metals for microplastic degradation are summarised in *Table 7*. Particular attention should be paid to noble metal-doped TiO_2 due to its enhanced photocatalytic performance for microplastics. Yuwendi et al. (2022) compared the application of Fe-TiO_2 and Ag-TiO_2 for the photocatalytic degradation of PE. In the Fe-TiO_2 degradation system, the PE mass loss was approximately 9%, whereas in the Ag-TiO_2 system it was twice as high. These results indicated that high concentrations of transition metals could reduce the efficiency of PE degradation, as elevated Fe concentrations led to lattice defects and charge-carrier recombination. Zhou et al. (2022) used Pt-TiO_2 to degrade PET fiber microplastics, resulting in a mass loss of 29%. In addition, complete mass loss of PA66 microplastics was achieved using Ag-TiO_2, highlighting the excellent UVA light absorption properties of Ag-TiO_2 and its strong ability to separate photogenerated e^-/h^+ pairs (Wang et al., 2025).

Compared to other materials, Ag exhibits low toxicity and high thermal and electrical stability. Ag NPs serve as electron mediators and photosensitizers, promoting the generation and stabilization of e^-/h^+ pairs

under low-energy light irradiation. Numerous studies have shown that Ag-doped TiO_2 enhances photocatalytic degradation efficiency through three main mechanisms: (1) modification of TiO_2 morphology, which increases its affinity for dissolved oxygen, (2) suppression of charge carrier recombination, and (3) SPR effects that facilitate electron injection (Dong et al., 2019).

Table 7. Photocatalytic degradation of microplastics using metal-doped TiO_2.

Photocatalyst	Dopant	Degradation conditions	MPs type	Degradation efficiency	Ref
Fe-TiO_2	Fe	Time: 1.5 h UVC (λ = 254 nm)	PE; Size: 100-150 µm	~9%	(Yuwendi et al., 2022)
Ag-TiO_2	Ag	Time: 1.5 h UVC (λ = 254 nm)	PE; Size: 100-150 µm	18%	(Yuwendi et al., 2022)
Pt NPs decorated N-TiO_2	Pt wire	Time: 12 h; 300 W xenon lamp	PET fiber	29%	(Zhou et al., 2022)
$Bi_4Ti_3O_{12}$	Bi	Time: 6 h; 300 W xenon lamp	LDPE	38.27%	(Jia et al., 2024)
$(Al_2O_3)_{0.75}TiO_2$	Al_2O_3	Time: 8h; pH 9.5; 30 ± 0.5 °C; 4 W LED lamps	PET	37%	(Camacho-González et al., 2025)
CuMgAlTi-LDH	Cu, Mg, Al	Time: 300 h; 50 W xenon lamp	PS PE	54.2% 33.7%	(Jiang et al., 2023)
TiO_x/ZnO	Zn	Time:480/624/816 h; Pretreatment with 12% H_2O_2 for 96 h; UVA light	PE, PES, Env. MPs	100%	(He et al., 2023)
Ag-TiO_2	Ag	Time 4 h; UVA lamp	PA66	100%	(Wang et al., 2025)

1.4. Real-world applicability of photocatalytic degradation

1.4.1. Implementation into the wastewater treatment plant

Photocatalytic degradation is currently considered one of the most effective advanced oxidation processes for microplastic removal. Moreover, photocatalytic degradation has potential for implementation in the tertiary phase of WWTPs to control and mitigate the release of microplastics into the environment (Nohara et al., 2024).

This advanced treatment approach has already been studied for other organic pollutants in wastewater, such as antibiotics. For example, Moles et al., (2024) used a pilot-scale plant over multiple cycles and achieved removal rates of 5 antibiotic classes, ranging from 61% to 89%, in the WWTP effluent. While most studies indicate that the photocatalytic degradation approach is suitable for removing microplastics, large-scale application remains insufficiently studied and poorly understood. A previous study by Uheida et al. (2021) used a pilot-scale photocatalytic reactor to remove microplastics under WWTP conditions. The photocatalytic reactor consisted of eight clear soda-lime glass tubes, each measuring 2 cm in diameter and 24 cm in length, arranged over a mirror-finished aluminum reflector. In this specific setup, ZnO nanorods were irradiated with visible light to degrade PP microplastics, achieving a degradation efficiency of 65%. This system demonstrated for the first time that a photocatalytic reactor has great potential for being implemented into a WWTP, particularly for microplastic removal. However, the lack of studies on large-scale applications also suggests limitations of this process in real-world systems.

Several limitations restrict the broad implementation of photocatalytic degradation into WWTPs. A major concern remains the immobilization and recovery of photocatalysts after treatment. Furthermore, materials used in the photocatalytic reactor should maintain structural and functional stability under prolonged UV or solar irradiation and in the presence of other reactive chemicals. Another challenge is optimizing photocatalytic reaction conditions, as laboratory-scale studies can not accurately reflect conditions in field applications, including limited light penetration, variable flow conditions, and the presence of other contaminants in complex wastewater matrices. The wide diversity of microplastics in the environment poses additional challenges for ensuring consistent microplastic removal efficiency. Furthermore, reliance on the light source and its intensity, prolonged reaction duration, and the need for relatively large quantities of catalyst raise concerns about financial feasibility.

Overall, to improve the applicability of photocatalytic degradation, future studies should focus on pilot-scale experiments and the development of continuous-flow reactors to more closely simulate natural conditions and bridge the gap between fundamental research and industrial applications. In addition, the analysis of by-products and microplastic mineralization rate should also be carefully considered.

1.4.2. Floating photocatalysts

Traditional photocatalysts are often used in powder form and exhibit several limitations, including aggregation and sinking to the bottom, where light penetration is poor. Meanwhile, floating photocatalysts are nanocomposite materials designed to address the limitations of traditional powder-based photocatalysts. They typically consist of an active photocatalyst agent, such as TiO_2 or ZnO, immobilized on a lightweight, floatable substrate. Various lightweight materials can serve as substrates for metal oxides, including cork, hollow glass microspheres, and expanded clay aggregates. It is important to note that plastic materials, such as PE, PP, or PS, can serve as buoyant substrates for a nanocomposite containing catalytic materials (Varnagiris et al., 2020). Floating photocatalysts are considered a highly promising strategy for microplastic degradation because many types of microplastics have a relatively low density, causing them to remain suspended or float on the water surface rather than sink.

Floating catalysts overcome limitations that are commonly observed in powder-type catalysts. These catalysts receive direct solar or UV radiation without the energy losses that occur when light passes through water (Ramírez-Escárcega et al., 2025). As the floating catalyst remains on the surface of the reaction solution, it ensures better interaction with atmospheric oxygen, resulting in more effective ROS generation. Moreover, floating catalysts do not require stirring and can be easily separated from water after treatment processes, enhancing their reusability. Thus, the use of floating photocatalysts in WWTPs is a promising strategy to mitigate microplastic pollution. In addition, floating photocatalysts can be integrated into existing WWTP processes, such as combining them with nanofiltration membranes or electro-oxidation systems to improve removal rates and reduce membrane fouling (Poerio et al., 2024).

It should also be noted that floating photocatalysts are considered highly suitable for treating a variety of water bodies beyond WWTPs. Previous studies indicated that this photocatalytic degradation approach could be applied to remote rivers and lakes, seawater, and oceans. For example,

Wang et al. (2019) studied commercial TiO_2 NPs immobilized on hollow acrylic spheres for phenol degradation in seawater and achieved a removal efficiency of 95% after 8 hours of visible-light irradiation.

Although floating photocatalysts have great potential for degrading microplastics in both WWTPs and natural water bodies, several technical limitations remain. These include catalyst leaching, the formation of toxic degradation by-products, and the lack of scalable reactor designs for real-world applications. Future research should focus on microplastic degradation using floating photocatalysts to enhance the overall mineralization process and broaden applicability in natural water bodies.

1.5. Chapter conclusion

There is a growing environmental urgency regarding microplastic pollution, highlighting its persistence, widespread distribution, and potential risk to ecosystems and human health. Despite the development of regulatory frameworks to reduce plastic waste and microplastic emissions, current policies remain insufficient to address the scale of the problem. This highlights the need for advanced and scalable remediation technologies capable of efficiently removing microplastics.

Photocatalytic degradation is a promising approach because it can fully mineralize microplastics under environmentally relevant conditions. Catalysts, particularly TiO_2, play a key role in this process, with research focused on enhancing their catalytic efficiency through metal doping and nanocomposite formation. These modifications aim to overcome limitations such as insufficient visible-light activity and rapid e^-/h^+ recombination. While laboratory-scale studies demonstrate encouraging results, they also reveal variability in degradation efficiency across polymer types, catalyst properties, and operational parameters, indicating that further optimization is necessary.

Importantly, the translation of photocatalytic degradation from controlled experimental settings to real-world applications remains a critical challenge. The complexity of microplastic composition and physicochemical properties, as well as catalyst performance under varying reaction conditions, must be addressed to ensure the practical feasibility of photocatalytic degradation.

2. MATERIALS AND METHODS

2.1. Synthesis of nanomaterials

2.1.1. Synthesis of TiO_2, TiO_2-kaolinite and TiO_2-montmorillonite

The following materials were used for the synthesis of TiO_2-clay nanomaterials: titanium (IV) chloride ($TiCl_4$) (99.99%, Thermo Fisher Scientific), Kaolinite ($Al_2O_7Si_2{\cdot}2H_2O$; molecular weight: 258.16 g/mol, Sigma-Aldrich), Montmorillonite K10 ($Al_2H_2O_{12}Si_4$; surface area: 220–270 m^2/g, Sigma-Aldrich), ammonium hydroxide solution (NH_4OH) (25%, Sigma-Aldrich), absolute ethanol (C_2H_6O) (99.8%, Altakem Chemical Reagent). Deionized water was used throughout the entire experiment.

Nanoscale TiO_2 NPs were synthesized using a sol-gel process, as reported by Liu et al. (2007) and Zhang et al. (2011), with minor adjustments. First, a Ti^+ containing precursor was prepared by dropwise addition of $TiCl_4$ to a 2 M HCl solution under ice-bath cooling. The resulting mixture was diluted with 3–4 °C deionized water to adjust the $[Ti]/[H^+]$ molar ratio to 2:1. Then, 5M NH_4OH was introduced dropwise in 100 mL of the resulting mixture, under constant stirring until the pH reached 2–3. The obtained suspension was stirred at 650 rpm for 6 hours, then aged for 12 hours. After the above reaction, the formed precipitate was centrifuged, washed several times with deionized water and ethanol, oven-dried ("Snol" 67/350, Umega, Lithuania) at 70 °C for 24 hours, and calcinated at 500 °C for 1 hour in a muffle furnace ("Snol" 8.2/110, AB Utenos Elektrotechnika, Lithuania). TiO_2 NPs appeared as a milky-white powder.

Both TiO_2-Kao and TiO_2-MMT nanocomposites were prepared using the same synthesis pathway. Initially, 4 g of each clay was dispersed in 400 mL of deionized water in separate beakers, and the mixtures were homogenized by vigorous stirring for 5 hours at room temperature. Then, 100 mL of the as-prepared Ti^+ containing precursor was added to the suspension at a controlled dropwise rate. The pH of the resulting mixture was adjusted to 2-3 by adding 5 M NH_4OH. Afterward, the mixture was stirred at 70 °C for 4 hours, followed by a 12-hour aging period. The obtained nanocomposites were isolated by centrifugation, washed at least three times with deionized water and ethanol, dried in an oven at 70 °C for 24 hours, and calcined at 500 °C for 1 hour. TiO_2-Kao exhibited a grey-yellow color, while TiO_2-MMT appeared white-grey. Such coloration is typical of nanocomposites based on these specific clay materials, as reported in the literature (Barbosa et al., 2015). The synthesized TiO_2, TiO_2-Kao, and

TiO_2-MMT were placed in glass containers and preserved at room temperature in the dark until further use.

Among the various synthesis methods for TiO_2 NPs and TiO_2-clay nanocomposites, including hydrothermal/solvothermal, green and biological synthesis, microwave techniques, and electrodeposition, the sol-gel method is the most commonly used. This method employs mild reaction conditions, such as low temperatures, which require low energy, simple laboratory equipment, and are easily scalable. In addition, the sol-gel method ensures control over morphological properties, homogeneity, and size distribution of nanomaterials (Calabrese et al., 2023).

2.1.2. Synthesis of Ag-TiO_2 with varying Ag concentrations

To synthesize Ag-TiO_2 nanomaterials, the following reagents were used: anatase titanium (IV) oxide (TiO_2) (≥99%, Sigma-Aldrich), silver nitrate ($AgNO_3$) (99.8%, Honey Fluka), and absolute ethanol (C_2H_6O) (99.8%, Altakem Chemical Reagent).

Nanoscale Ag-TiO_2 nanomaterials with varying silver concentrations were prepared using the photoreduction method previously suggested by Huang et al. (2017). The pure anatase phase of TiO_2 (3 mmol) was added to 100 mL of deionized water under constant stirring to ensure uniform dispersion. Next, predetermined quantities of silver nitrate (0.5 mmol, 1 mmol, 3 mmol) were added to the suspension. The obtained mixtures were placed in a closed photoreaction chamber and exposed to a 36 W UV-A lamp at 365 nm for 6 hours, under constant stirring. The synthesized materials were collected by centrifugation, washed repeatedly with deionized water and ethanol, and dried at 70 °C for 10 hours. Ag-TiO_2 nanomaterials were labeled as Ag-$TiO_2$0.5, Ag-$TiO_2$1, and Ag-$TiO_2$3 to indicate silver concentrations of 0.5 mmol, 1 mmol, and 3 mmol, respectively. Finally, the nanomaterials were transferred to separate glass containers and stored at room temperature under dark conditions. Ag-TiO_2 nanomaterials appeared grey-purple.

The photoreduction method for Ag-TiO_2 synthesis is often chosen for its simplicity and efficiency. Recent studies have compared photoreduction with other methods, highlighting notable advantages, including complete reduction of Ag^+ ions, preservation of TiO_2 crystallinity, and enhanced photocatalytic activity (Behera et al., 2022).

2.2. Characterization of nanomaterials

The crystalline phases of the nanomaterials were characterized by X-ray diffraction (XRD) using a Rigaku SmartLab diffractometer configured in Bragg-Brentano geometry, equipped with a Cu-Kβ filter and an ultra-linear D/Tex detector. Diffraction patterns were collected over a 2θ range of 10–80° with a step size of 0.02°. The crystallite size of TiO_2 within the synthesized TiO_2-Kao and TiO_2-MMT nanocomposites was evaluated using the Scherrer equation, as described in earlier work (Eq. 10) (Toro et al., 2020):

$$D = \frac{K\lambda}{\beta\cos\theta} \tag{10}$$

where D indicates the crystallite size, K is the shape constant (~0.9), λ corresponds to the incident X-ray wavelength (0.15406 nm for Cu Kα), β is the full width at half maximum (FWHM) of the analyzed diffraction peak, and θ is the Bragg diffraction angle.

For Ag-TiO_2 nanomaterials, the average crystalline structure size was estimated using the Halder-Wagner method, as suggested in previous studies (Nath et al., 2020). The Halder-Wagner approach assumes that the diffraction peak broadening follows a symmetric Voigt profile, reflecting the combined contributions of Lorentzian and Gaussian components (Kawsar et al., 2024). The relationship between crystalline size and lattice strain within the Halder-Wagner approach is expressed as (Eq. 11):

$$\left(\frac{\beta^*_{hkl}}{d^*_{hkl}}\right)^2 = \frac{1}{D}\cdot\frac{\beta^*_{hkl}}{{d^*_{hkl}}^2} + \left(\frac{\varepsilon}{2}\right)^2 \tag{11}$$

where d_{hkl} corresponds to the distance between the (hkl) lattice planes, $\beta^*_{hkl} = \frac{\beta_{hkl}\cos\theta}{\lambda}$ and $d^*_{hkl} = \frac{2d_{hkl}\sin\theta}{\lambda}$.

Equation (11) was plotted with $(\beta^*_{hkl}/d^2_{hkl})$ along the X-axis and $(\beta_{hkl}/d_{hkl})^2$ on the Y-axis for each diffraction peak. The slope of the fitted line provides the average crystallite size.

The surface morphology of TiO_2-clay samples was analyzed using a FEI Helios Nanolab 650 scanning electron microscope (SEM). Before imaging, the samples were coated with carbon and imaged in secondary electron (SEI) mode at an acceleration voltage of 3kV and a beam current of 100 pA. For morphological properties of Ag-TiO_2 nanomaterials, transmission electron microscopy (TEM) was conducted using Tecnai G2 F20

X-TWIN (FEI, Netherlands, 2011) instrument, fitted with a Schottky field emission electron source and a high-angle annular dark-field (HAADF) detector. Imaging was performed using single and double tilt holders, and micrographs were captured using an 11 MPix ORIUS SC1000B (Gatan) CCD camera. Elemental composition of the samples (Ag-$TiO_2$0.5, Ag-$TiO_2$1, and Ag-$TiO_2$3) was examined using energy-dispersive X-ray spectroscopy (EDX).

Fourier transform infrared (FTIR) spectroscopy was performed by a micro-FTIR LUMOS II (Bruker, Germany, 2024) with an attenuated total reflectance (ATR) germanium (Ge) (refractive index ~4.0) accessory. IR spectra were recorded over a wavenumber range of 4000-680 cm^{-1} with a resolution of 4 cm^{-1} and 128 scans per sample.

UV-Vis spectroscopy was employed to measure the optical absorption of the synthesized nanomaterials. The measurements were performed over a 250-800 nm wavelength range using a UV-Vis spectrophotometer ("Specord 210 Plus", Analytic Jena, Germany). The optical band gap (E_g) was determined according to Tauc's equation (Eq. 12) (Tauc et al., 1966):

$$\alpha h\nu = \alpha\left(h\nu - E_g\right)^n \quad (12)$$

where α represents the absorption coefficient, h is Planck's constant, and ν is the photon frequency. For direct transition ($n = \frac{1}{2}$), the E_g derived from a Tauc plot obtained by plotting $(\alpha h\nu)^{\frac{1}{n}}$ as a function of hν.

2.3. Selection and characterization of LDPE microplastics

Fragment-type, natural-color LDPE microplastics with an average size of ~300 μm were purchased from Goodfellow (Germany). LDPE fragments were defined by low density, flexibility, and hydrophobicity. In its powder form, it provides a high surface area and strong dispersibility.

Film-type LDPE was commercially available in a local market ("Ermitažas", Vilnius, Lithuania) and was bought in September 2024. Both black and transparent colors were used in this study, with a film thickness of 120 μm. LDPE films were cut into two size groups: 1×1 mm and 3×3 mm using the trimmer "Fellowes Neutron Plus" (Dongguan, China).

To analyze the morphological and chemical properties of LDPE microplastics, LDPE was first subjected to spectroscopic analysis using a micro-FTIR LUMOS II spectrometer (Bruker, Germany, 2024) in ATR mode. IR spectra of LDPE were obtained by averaging 128 scans over the wavenumber range 4000–680 cm^{-1}, with a spectral resolution of 4 cm^{-1}. Each LDPE microplastic type was measured at five positions, as previously

suggested by Kaewkam et al. (2022). The schematic illustration of measurement positions for fragment-type and film-type microplastics is provided in the following *Figure 8*. The obtained spectra were used to verify and confirm the chemical composition of LDPE microplastics.

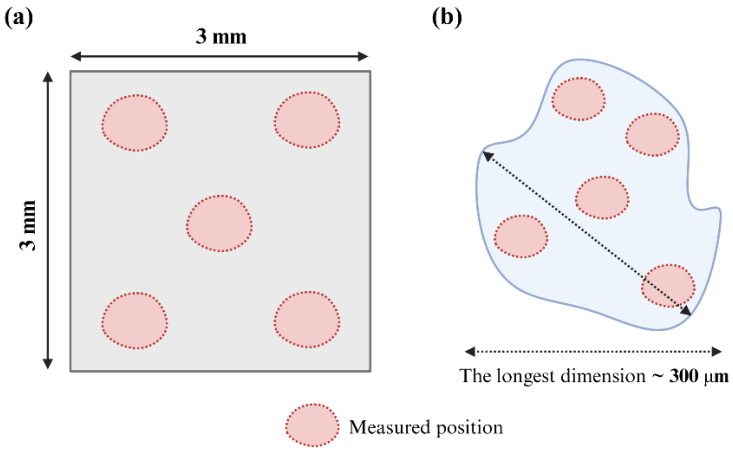

Figure 8. Schematic illustration of selected positions for measurements: (a) film-type LDPE, (b) fragment-type LDPE.

The surface morphology of film-type LDPE was characterized by SEM imaging using the same equipment as described in Chapter *2.2*. Prior to measurements, LDPE microplastics were chromium-coated (see chapter *2.5.2*). The SEM analysis of pristine LDPE microplastics revealed their surface properties and alterations.

Wavelength-dispersive X-ray fluorescence (WDXRF) analysis was conducted using an Axios mAX spectrometer (Panalytical, Netherlands) to characterize the elemental composition of the LDPE films. The instrumentation incorporated a 4 kW Rh-anode X-ray tube (STmax160) alongside a detection system comprising proportional-flow and sealed-proportional detectors (Xe gas) and a high-efficiency scintillation detector. Elemental analysis, ranging from oxygen (O) to uranium (U), was performed using six crystal analyzers. Furthermore, the system was calibrated against certified reference materials to ensure precise measurements across a diverse array of chemical elements.

2.4. Photocatalytic test

All photocatalytic tests were performed in a closed photochemical reaction chamber equipped with a 36 W UV-A light source at 365 nm. A UV wavelength of 365 nm was employed in this study because TiO_2 exhibits maximal absorption in the near-UV region, particularly close to 387 nm (Zhou et al., 2024). Furthermore, recent research has shown that 365 nm irradiation penetrates a TiO_2 dispersion more effectively than shorter wavelengths (254 nm) or longer wavelengths (420 nm and 475 nm), thereby improving overall photocatalytic efficiency (Li et al., 2021). The UV light source was positioned 10 cm above the sample. The Photocatalytic reaction was conducted at room temperature (22–24 °C) for the predetermined duration.

For the photocatalytic degradation of fragment-type LDPE microplastics, 20 mg each of LDPE and catalyst (TiO_2, TiO_2-Kao, or TiO_2-MMT) were added to a Petri dish and suspended in 10 mL of deionized water. Further, a Petri dish with the reaction mixture was placed in a photochemical reaction chamber. The photocatalytic degradation reaction was carried out for 60–480 min. This study also explored the influence of various factors on photocatalytic degradation, including the LDPE-to-catalyst ratio (1:2, 1:1, 2:1), solution pH (3–11), and solution IS (0.05–0.5 mol/L, adjusted with NaCl).

For film-type LDPE microplastics, a designated catalyst (TiO_2, Ag-$TiO_2$0.5, Ag-$TiO_2$1, or Ag-$TiO_2$3) was first suspended in 10 mL of deionized water to obtain a final concentration of 1 g/L. First, the mixture was subjected to ultrasound treatment for 10 min to prevent catalyst agglomeration and keep a homogeneous distribution of nanomaterials. Then, film-type LDPE was introduced into the mixture at a concentration of 1 g/L. The mixture was stirred at 200 rpm for 15 min to ensure uniform distribution within the reaction system. It was then placed in a photochemical reaction chamber and allowed to react for 60 to 960 min. The schematic representation of the experimental setup is provided in *Figure 9*.

The control experiments for both fragment-type and film-type LDPE microplastics were performed following the same procedures except that no catalyst was added. After the photocatalytic test, each sample was filtered through a glass fiber filter (“Branchia”, 50 mm, 1.6 μm pore size, Germany), several times washed with deionized water, and oven-dried at 40 °C for 60 min. Subsequently, fragment-type and film-type microplastics were collected and stored in glass Petri dishes at room temperature in the dark for further analysis.

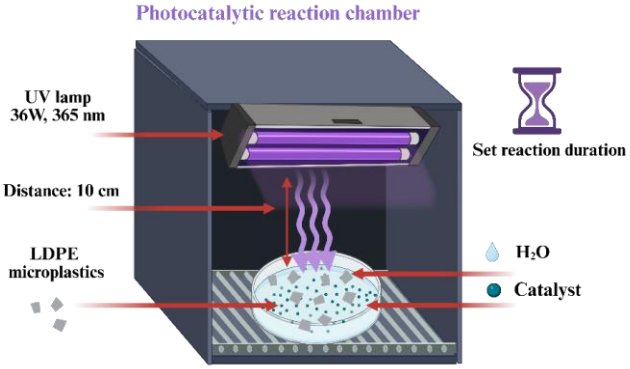

Figure 9. The schematic representation of the photocatalytic degradation experimental setup.

2.5. Post-degradation analysis of LDPE

2.5.1. Mass loss of LDPE and kinetic study

The removal efficiency of both fragment-type and film-type LDPE microplastics was determined by mass loss (%) analysis at set time intervals using a laboratory balance ("RADWAG XA 110", Poland). Mass loss is one of the most widely used approaches for assessing microplastic degradation, as it provides a direct, quantitative measure of material removal (Kinyua et al., 2024; Tan et al., 2023). This method offers notable advantages, given that it is easy to implement, requires no expensive laboratory equipment, and is sensitive to even minor changes in polymer mass.

The mass loss of LDPE was calculated by the following formula:

$$\text{Mass loss } (\%) = 100 \cdot \frac{M_i - M_t}{M_i} \tag{13}$$

where M_i presents the initial mass of LDPE microplastics and M_t is the final LDPE mass after degradation at the particular time of UV exposure.

The degradation kinetics of LDPE were determined using a pseudo-first-order kinetic model (Eq. 14). The kinetic parameters were obtained from the plot C_t *vs* t, using the "Origin Pro 2025" software.

$$\ln \frac{c_t}{c_i} = k_1 t \tag{14}$$

where c_i is the initial concentration of LDPE films, c_t is the final concentration of LDPE films at the defined degradation period, and k_1 is the rate constant for the pseudo-first-order kinetic model.

2.5.2. Surface morphology changes

An FEI Helios Nanolab 650 SEM was used to examine changes in the surface morphology of film-type LDPE before and after the photocatalytic degradation process. Before SEM measurements, each LDPE film was chromium-coated. It is crucial to note that chromium coating was chosen over the more often used carbon coating due to its lower sputtering temperature (near room temperature), which prevents deformation or melting of plastic polymers. LDPE films were measured and analyzed in SEI mode, operated at an acceleration voltage of 3 kV and a beam current of 100 pA.

2.5.3. Spectroscopic analysis

IR spectra of LDPE microplastics were recorded using a micro-FTIR LUMOS II (Bruker, Germany, 2024) in ATR mode over a wavenumber range of 4000–680 cm^{-1}, with a spectral resolution of 4 cm^{-1}, and 128 scans were collected per sample. The functional group changes and oxidation processes within the polymeric chain were evaluated by calculating carbonyl and vinyl (VI) indices, as follows Eq. 15 and Eq. 16, respectively (Almond et al., 2020; Sura and Nain, 2024).

$$\mathrm{CI} = \frac{\text{Area under band } 1850-1650\ \mathrm{cm^{-1}}}{\text{Area under band } 1500-1420\ \mathrm{cm^{-1}}} \tag{15}$$

$$\mathrm{VI} = \frac{\text{Area under band } 930-880\ \mathrm{cm^{-1}}}{\text{Area under band } 1500-1420\ \mathrm{cm^{-1}}} \tag{16}$$

The CI is a key indicator for evaluating oxidation processes and the formation of oxygen-containing groups within polymer chains, particularly the peak associated with carbonyl groups (−C=O). In contrast, the VI indicates the formation of vinyl groups (−C=C), which likely arise from chain scission during oxidation processes (Fairbrother et al., 2019). The CI and VI values were determined using an area-integrated approach by employing "Origin Pro 2025" software. The calculations were conducted after applying a baseline correction and using peak-analysis tools. The CI and VI were determined as the mean value of three randomly selected samples (significance level, 0.05).

2.6. Quenching experiments

The quenching test is a qualitative method that uses specific chemical quenchers to react with a particular ROS. These quenchers compete with LDPE films for ROS, thereby reducing or inhibiting LDPE degradation reactions.

In this study, the major ROS involved in the photocatalytic degradation process of film-type LDPE in the presence of catalyst were evaluated using isopropyl alcohol (IPA) (10 mM) ($(CH_3)_2CHOH$) (≥99.5%, Sigma-Aldrich), ascorbic acid (AA) (2 g/L) ($C_6H_8O_6$) (99.7-100.5%, Sigma-Aldrich), and ammonium oxalate (AO) (1 g/L) ($(NH_4)_2C_2O_4 \cdot H_2O$) (≥99%, Sigma-Aldrich), to quench $\cdot OH$, $O_2^{\cdot -}$, and h^+, respectively. Among various chemical quenchers, these are noted for high sensitivity to the targeted ROS, without affecting the properties of LDPE microplastics. Quenching tests were carried out for 240 min following the same procedure as the photocatalytic tests (chapter *2.4*), with minor adjustments to incorporate ROS quenchers into the reaction system.

Other analytical approaches for characterizing ROS include electron paramagnetic resonance (EPR), chemiluminescence analysis, and spectrophotometric methods. It is important to note that qualitative tests are generally more favorable for characterizing ROS than quantitative tests. Firstly, quantitative methods can be challenging to implement due to the need for expensive laboratory equipment and the short lifespan of ROS, which ranges from nanoseconds to microseconds. Next, the heterogeneity of microplastic surfaces promotes ROS diffusion, further complicating the quantitative detection of ROS (Ge et al., 2022). Meanwhile, qualitative methods such as quenching tests, along with other analytical tools like surface morphology analysis and spectroscopic analysis, provide reliable, consistent data for studying degradation mechanisms.

2.7. Statistical analysis

Statistical analysis was conducted to evaluate the significance of differences between experimental groups. All photocatalytic degradation experiments were performed in triplicate or more and are presented as mean ± standard deviation (SD). A one-way analysis of variance (ANOVA) was used to assess differences among multiple groups, followed by Tukey's honest significant difference (HSD) test for Post-hoc pairwise comparisons. A significance level of $p < 0.05$ was considered statistically significant. All statistical analyses were carried out using "JASP" (version 0.18.3.0).

3. RESULTS AND DISCUSSION

3.1. Characterization of nanomaterials

3.1.1. Structural analysis by XRD

The XRD diffractograms of TiO_2, TiO_2-MMT, and TiO_2-Kao are presented in *Figure 10 (a)*. Strong peaks at 2θ = 27.38° (110), 36.08° (101), 39.29° (200), 41.22° (111), 44.16° (210), 54.32° (211), 56.61° (211), 62.89° (002), 64.23° (310), 69.01° (301), and 69.89° (112) correspond to the rutile phase of TiO_2 (PDF Card No.: 04-004-4337), while the weaker peaks observed at 25.34° (101) and 48.05° (200) indicate the presence of anatase TiO_2 (PDF Card No.: 04-002-2750). In TiO_2-Kao, the anatase phase of TiO_2 was detected at 25.34°, in contrast to TiO_2-MMT, which contained only rutile TiO_2. The kaolinite phase in TiO_2-Kao was confirmed by diffraction peaks at 21.9° and 26.6° (PDF Card No.: 00-005-0143), whereas the montmorillonite phase in TiO_2-MMT was identified by a peak at 35.02° (PDF Card No.: 00-029-1499). Additional peaks observed in TiO_2-MMT at 26.79°, 32.04°, and 45.42° were attributed to muscovite (PDF Card No.: 00-058-2037). Although the montmorillonite was commercially obtained, the presence of muscovite is commonly reported due to natural co-occurrence or trace impurities (Marsh et al., 2018).

The characteristic rutile TiO_2 peaks at 39.29°, 44.16°, 56.61°, 62.80°, 64.23°, 69.01°, and 69.89° were absent in the TiO_2-Kao and TiO_2-MMT nanocomposites, indicating successful deposition of TiO_2 on the surface of the clay minerals. The low intensity of the clay peaks further supports effective TiO_2 loading, consistent with observations reported by Zhang et al. (2011). The average crystallite size of TiO_2 NPs, calculated using Scherrer's equation (Eq. 10), was found to be 40–60 nm. After incorporation into clay minerals, the TiO_2 particle size decreased slightly to 30–40 nm. This indicates that the clay matrix inhibits crystallite growth and facilitates NPs dispersion (Li et al., 2020).

The XRD diffractograms of Ag-$TiO_2$0.5, Ag-$TiO_2$1, and Ag-$TiO_2$3 are shown in *Figure 10 (b)*. The detected diffraction peaks at 25.31°, 36.95°, 38.58°, 48.04°, 53.90°, 55.07°, 62.69°, 68.76°, 70.30°, and 75.06° were assigned to the (101), (103), (112), (200), (105), (211), (204), (116), (220), and (215) planes of anatase TiO_2 (PDF Card No.: 04-014-5762). The sharp and well-resolved peaks indicate a highly crystalline structure, as expected for commercial TiO_2. These findings suggest that Ag^+ ions are primarily deposited

on the TiO_2 surface, rather than being integrated into the crystal lattice, which aligns with the TEM results presented in Section *3.1.3* (Guo et al., 2009).

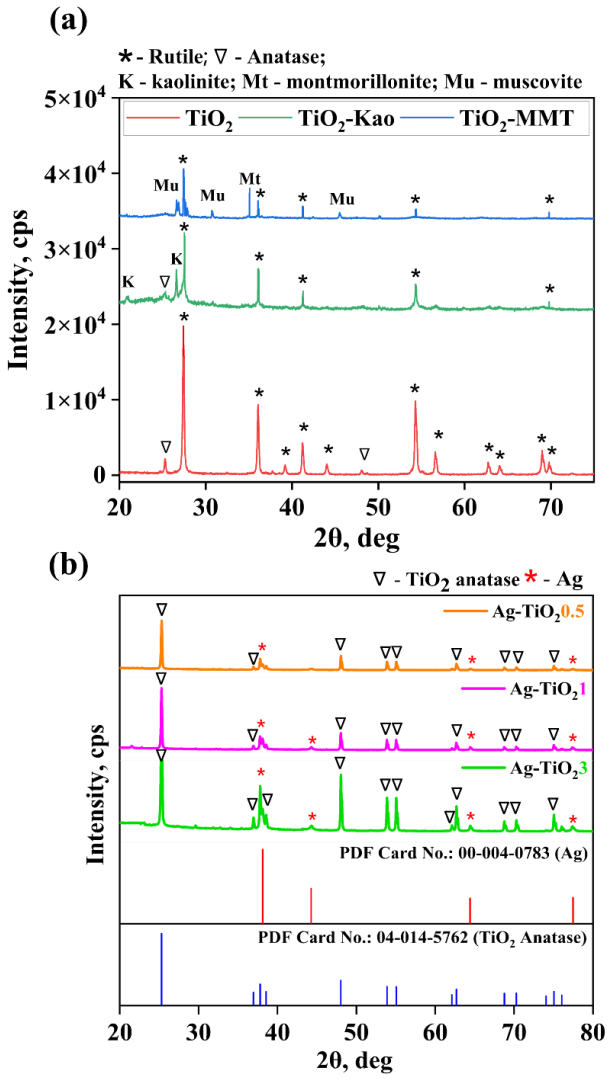

Figure 10. XRD diffractograms of (a) TiO_2, TiO_2-Kao, and TiO_2-MMT and (b) Ag-$TiO_2$0.5, Ag-$TiO_2$1, and Ag-$TiO_2$3.

Diffraction peaks at 38.12°, 44.28°, 64.43°, and 77.47° were attributed to the (111), (200), (220), (311) planes of the metallic silver phase (PDF Card No.: 00-004-0783), confirming successful Ag deposition onto the surface of TiO_2. The relatively low intensity of metallic silver indicates limited deposition of silver, consistent with earlier reports (Zheng et al., 2019). As the amount of $AgNO_3$ in the photoreduction synthesis increased, the intensity of the Ag peaks became more pronounced, likely due to an elevated Ag^+

concentration, which promotes the formation of more metallic silver NPs. The average crystallite size of the Ag NPs was determined to be 19 nm, calculated using the Halder-Wagner method (Eq. 11).

3.1.2. ATR-FTIR spectral analysis

The ATR-FTIR spectra of the synthesized TiO_2, TiO_2-Kao and TiO_2-MMT are shown in *Figure 11*. For TiO_2, the absorption bands observed in the range of 800–680 cm^{-1} are assigned to the stretching vibrations of titanium-oxygen-titanium (Ti-O-Ti). In the TiO_2-Kao, the presence of kaolinite is confirmed by its characteristic bands at 1054 cm^{-1}, 754 cm^{-1}, and 720 cm^{-1}, whereas the TiO_2-MMT shows the typical absorption peaks of montmorillonite at 1037 cm^{-1}, 917 cm^{-1}, and 720 cm^{-1}. The absorption band appearing at ~1030 cm^{-1} is common to both kaolinite and montmorillonite and is attributed to the stretching vibrations of Si-O bonds, including Si-O-Si and O-Si-O (Li and Yang, 2014). In the TiO_2-Kao and TiO_2-MMT nanocomposites, the Si-O stretching band exhibits a shift to 1054 cm^{-1} and 1037 cm^{-1}, respectively, indicating the formation of new chemical interactions between the TiO_2 surface and Si-O groups of the clay minerals. Additionally, the band observed at 917 cm^{-1} in TiO_2-MMT is attributed to the antisymmetric stretching vibration of Si-O-Ti, arising from the polarization of the Si-O bond (Barbosa et al., 2015).

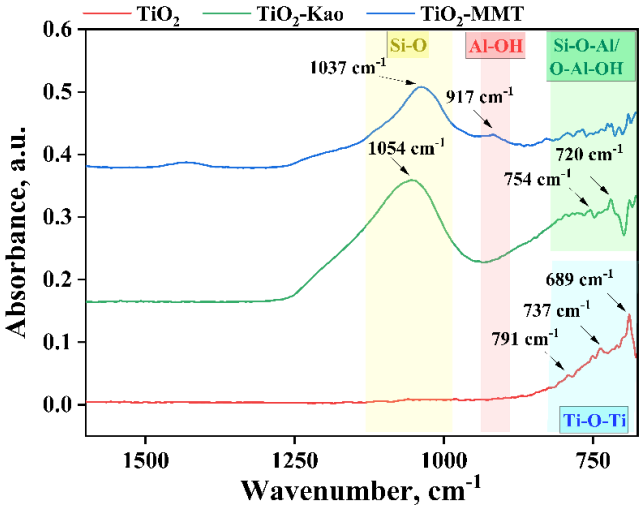

Figure 11. ATR-FTIR spectra of TiO_2, TiO_2-Kao, and TiO_2-MMT in the region 1600–680 cm^{-1}.

The intensity of the characteristic peaks of TiO_2 decreases slightly when forming composites with kaolinite and montmorillonite. The TiO_2 band at 737 cm^{-1} is no longer observed in either the TiO_2-Kao or TiO_2-MMT composites, while the band at 791 cm^{-1} disappears only in the TiO_2-Kao composite. This behavior suggests stronger interfacial interactions between TiO_2 and kaolinite than between TiO_2 and montmorillonite.

Further, ATR-FTIR spectroscopy was used to investigate the surface functional groups of TiO_2 and Ag-TiO_2 nanomaterials. *Figure 12* shows that the blue line contains a broad band at 680-800 cm^{-1}, which corresponds to Ti–O–Ti stretching vibrations and O–Ti–O lattice, confirming the formation of the Ti-O crystal (Jadhav et al., 2025). The deposition of Ag (orange, purple, and green curves) did not alter the overall band structure of TiO_2, showing only minor spectral variations. A slight decrease in the intensity of the Ti–O–Ti stretching vibrations was observed as the amount of $AgNO_3$ in the precursor suspensions increased, which may be attributed to interactions between Ag and TiO_2. In addition, the absence of emerging characteristic bands indicates that Ag remains in the metallic state, without the formation of a distinct oxide phase.

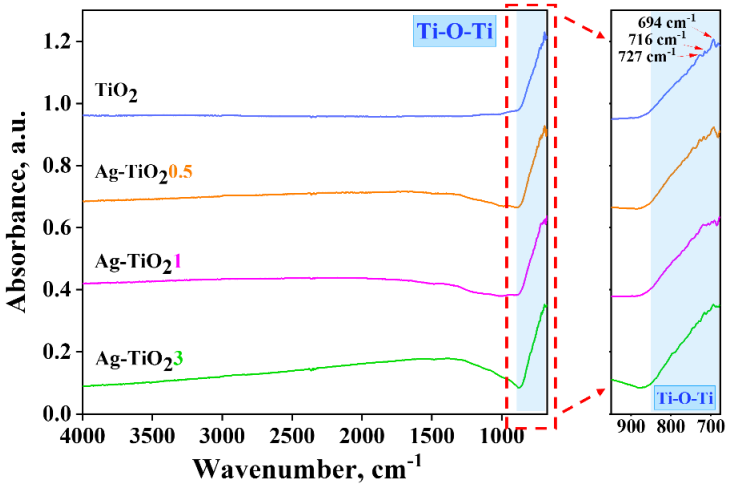

Figure 12. ATR-FTIR spectra of TiO_2, Ag-$TiO_2$0.5, Ag-$TiO_2$1and Ag-$TiO_2$3 in the region 4000–680 cm^{-1}.

The broad band assigned to the O–H bending vibrations in the 1250–640 cm^{-1} range for samples Ag-$TiO_2$1 and Ag-$TiO_2$3 suggests the presence of surface hydroxyl groups and adsorbed water. By contrast, the spectra of both samples, TiO_2 and Ag-$TiO_2$0.5, showed an absence of O–H bending vibrations, while the most intense O–H bending modes were found in Ag-$TiO_2$3. The high Ag content in Ag-$TiO_2$3 results in an increased number of

surface defects and exposed active sites, thereby promoting water absorption (Sun et al., 2021). The presence of absorbed hydroxyl ions enhances the photocatalytic reaction by capturing charge carriers and generating ROS. Moreover, hydroxyl ions act as absorption sites and active sites for microplastics, thereby improving the photocatalytic performance of nanomaterials.

3.1.3. SEM and TEM imaging

SEM images of TiO_2, kaolinite, montmorillonite, TiO_2-Kao, and TiO_2-MMT composites are presented in *Figure 13*. TiO_2 NPs have spherical to irregular shapes and tend to aggregate (*Figure 13* (a, b)). Such irregular and porous surface properties contribute to a high surface area, which is favorable for catalytic applications. Kaolinite clay minerals are characterized by platy, sheet-like particles with pseudohexagonal morphology and smooth surfaces (*Figure 13* (c, d)). Meanwhile, montmorillonite exhibits irregular, rough-textured layers that aggregate into clusters (*Figure 13* (e, f)). These surface features closely correspond to the known morphological characteristics of each clay (Ural, 2021).

TiO_2 NPs were effectively loaded onto kaolinite and montmorillonite, as shown in *Figure 13* (g-j), which aligns well with XRD and ATR-FTIR analyses. Following TiO_2 loading, the kaolinite surface remains platy, with a hexagonal structure and a smooth texture (*Figure 13* (g, h)). In comparison, TiO_2-MMT exhibits rougher, irregular layers, with TiO_2 particles dispersed unevenly and tending to form aggregated clusters (*Figure 13* (i, j)). The aggregation of TiO_2 NPs was more pronounced on the montmorillonite surface compared to kaolinite. While this may increase the TiO_2 content in TiO_2-MMT, excessive aggregation can reduce the surface area available for photocatalytic reactions. TiO_2 NPs are more evenly distributed on the kaolinite surface, thereby enhancing light absorption and active-site accessibility, contributing to more effective photocatalytic degradation performance.

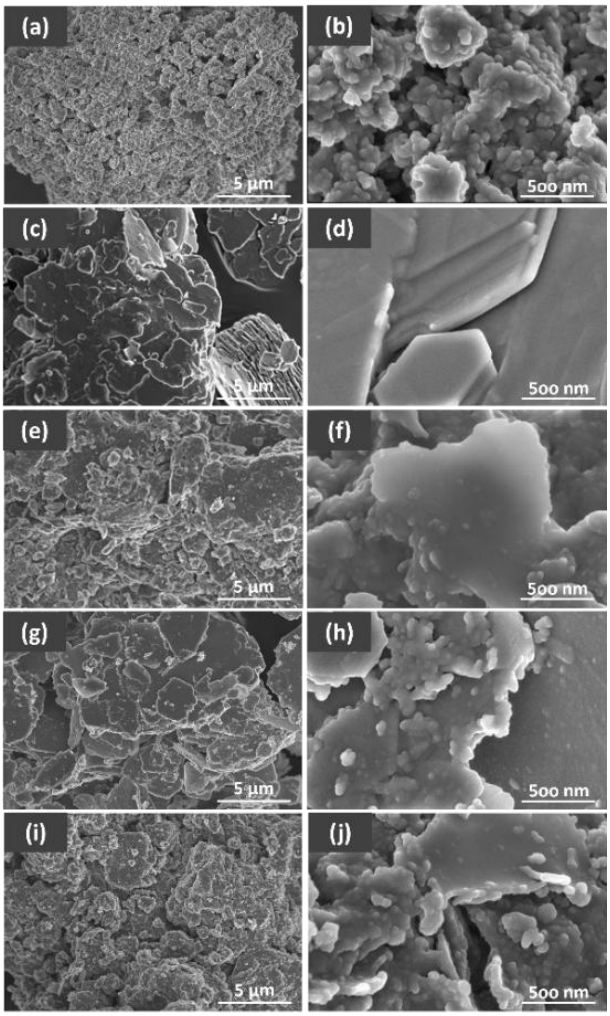

Figure 13. SEM images of TiO_2, TiO_2-Kao, and TiO_2-MMT at different magnifications: (a,b) TiO_2; (c, d) kaolinite; (e, f) montmorillonite; (g, h) TiO_2-Kao; (i, j) TiO_2-MMT.

TEM imaging was carried out to evaluate the surface morphology of TiO_2 and Ag-TiO_2 nanomaterials. As shown in *Figure 14 (a, b),* TEM analysis indicated that TiO_2 NPs are irregular in shape and broadly distributed in size, with an average diameter of 130 nm. The appearance of dark spots on the TiO_2 surface indicates the presence of Ag NPs, as silver has a higher atomic weight than titanium (*Figure 14 (b-d)*). The size and shape of the TiO_2 crystallites remain unchanged after the deposition of silver on their surface. Furthermore, the density of dark dots on the surface of TiO_2 increased as the concentration of Ag-NO_3 in the reaction precursor suspension increased, indicating successful silver loading on the TiO_2 through the photoreduction method.

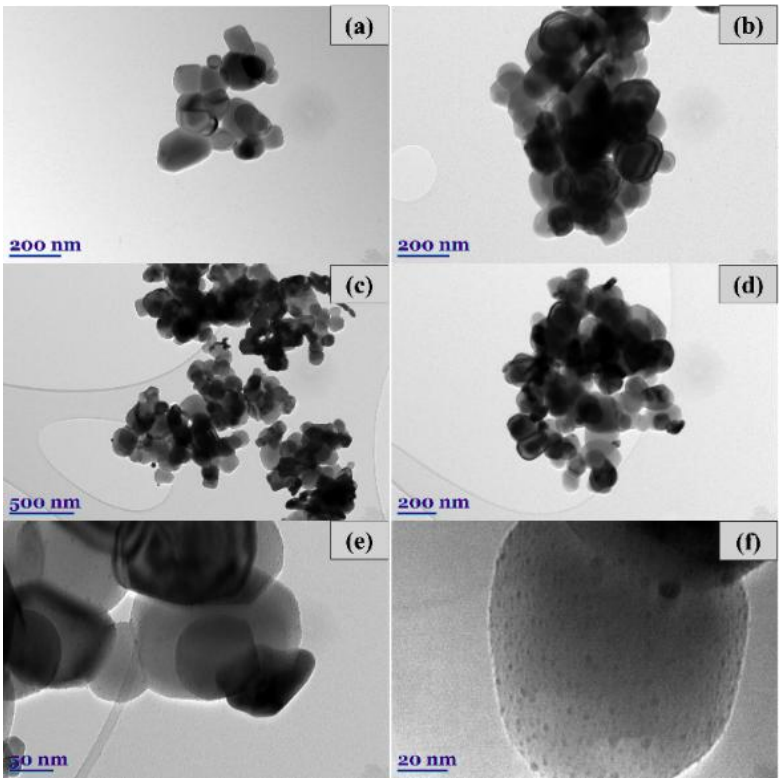

Figure 14. TEM images of TiO_2 and Ag-TiO_2 nanomaterials at different magnifications: (a) TiO_2; (b) Ag$TiO_2$0.5; (c) Ag-$TiO_2$1; (d-f) Ag-$TiO_2$3.

The presence of Ag in Ag-TiO_2 nanomaterials was also confirmed by EDX spectra, which are consistent with TEM results (*Table 8*). Based on EDX measurements, the silver content in Ag-TiO_2 nanomaterials was 4.82 wt%, 19.56 wt%, and 42.76 wt% for Ag-$TiO_2$0.5, Ag-$TiO_2$1, and Ag-$TiO_2$3, respectively. Ag-$TiO_2$3 has shown higher local Ag wt% values, most likely because EDX measurements were conducted in well-deposited areas of the sample. At higher magnification, Ag NPs appear nearly spherical, with a narrow size distribution of 15-20 nm. Their relatively small size makes them attractive candidates for photocatalytic applications, due to the increased specific surface area and enhanced catalytic activity (*Figure 14 (e-f)*). Moreover, the Ag NPs are evenly distributed across the TiO_2 surface, indicating a core-shell structural configuration that enhances the photocatalytic activity of the silver-containing TiO_2 nanomaterials compared to pure TiO_2 NPs (Petronella et al., 2019).

Table 8. Energy dispersive X-ray spectroscopy (EDX) analysis of Ag-TiO_2 nanomaterials.

Nanomaterials	Element	wt %	Atomic %
Ag-$TiO_2$0.5	Ti	69.31	51.99
	O	25.85	41.56
	Ag	4.82	1.44
Ag-$TiO_2$1	Ti	62.16	43.56
	O	18.26	49.51
	Ag	19.56	6.91
Ag-$TiO_2$3	Ti	41.37	35.31
	O	15.84	35.31
	Ag	42.76	18.48

3.1.4. Optical characterization and Tauc plot analysis

The optical properties of TiO_2, TiO_2-Kao, and TiO_2-MMT were assessed using UV-Vis absorption spectra measured over the wavelength range of 300–600 nm (*Figure 15)*. Tauc plot analysis was used to determine the band gap energy (E_g) for each catalyst (Eq. 12). A reduction in the band gap was observed with the formation of the TiO_2-clay nanocomposite, with values decreasing from 3.10 eV for pure TiO_2 NPs to 2.95 eV for TiO_2-MMT and 2.88 eV for TiO_2-Kao. The shift in band gap energy is likely associated with heterojunction development, particle size, and strain effects, as well as Ti–O–Si (or Ti–O–Al) bonding, which alter the electronic structure of TiO_2 (Chanani et al., 2023). These results are consistent with previously reported studies indicating that TiO_2-clay nanocomposites exhibit lower band gap energies than pure TiO_2 NPs (Li et al., 2020). The band gap reduction strongly depends on the clay type, composition, and synthesis conditions. For example, TiO_2-metakaolin composites were found to exhibit a band gap energy of 3.06–3.11 eV, TiO_2-red clay of 2.1 eV, and TiO_2-zeolite of 2.56 eV (Sitorus et al., 2025). In this study, the decrease in band gap energy suggests that both kaolinite and montmorillonite enhance the photocatalytic performance of TiO_2 as a lower band gap energy of the catalyst can facilitate electron excitation and extend absorption into longer wavelengths.

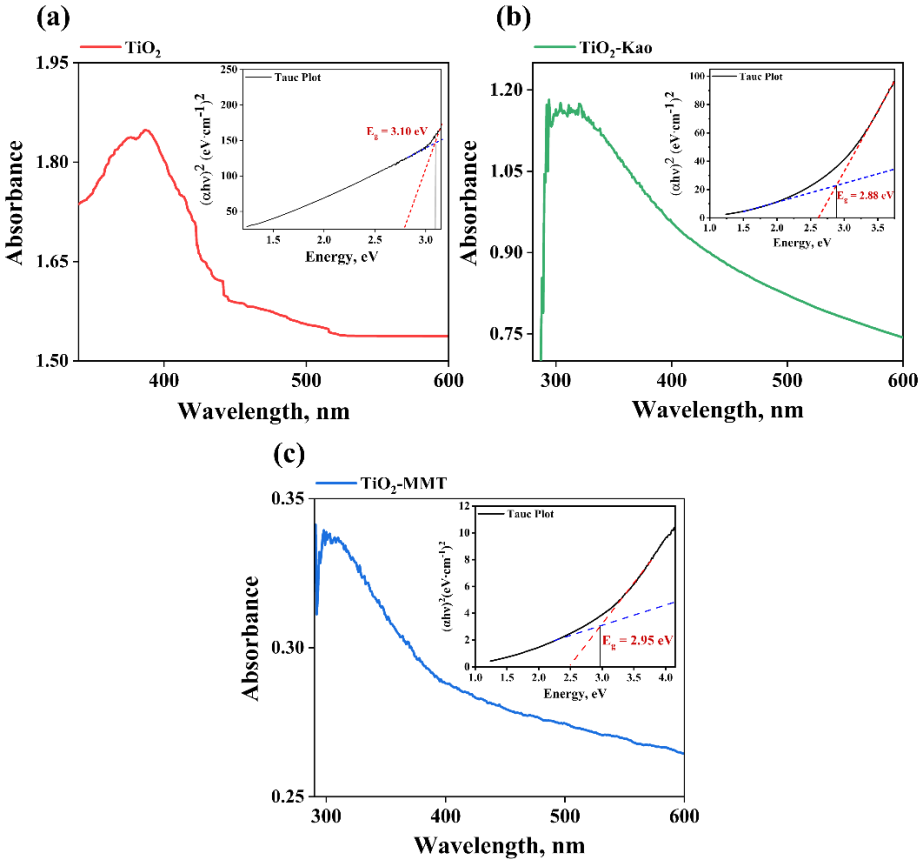

Figure 15. UV-Vis absorption behavior and corresponding Tauc plots of TiO_2 and TiO_2-clay nanomaterials: (a) TiO_2; (b) TiO_2-Kao; (c) TiO_2-MMT.

The UV-Vis absorption spectra of TiO_2 and Ag-TiO_2 nanomaterials with varying silver concentrations were studied over the wavelength range of 300–650 nm, as shown in *Figure 16 (a)*. TiO_2 NPs exhibited a maximum absorption peak at 330 nm, consistent with previous reports indicating that TiO_2 absorbs light within the 275–405 nm wavelength range (Ghamarpoor et al., 2023). Once Ag was deposited on the TiO_2 NPs surface, the absorption band shifted to longer wavelengths, with maximum absorption at 331 nm, 340 nm, and 358 nm for Ag-$TiO_2$0.5, Ag-$TiO_2$1, and Ag-$TiO_2$3, respectively. This shift toward the visible-light region is attributed to the surface plasmon resonance (SPR) effect. This effect could be explained by the spatial confinement of electrons in Ag^0 particles on the TiO_2 surface (Jung et al., 2018). Furthermore, the formation of a broad absorption band in Ag-$TiO_2$1 and Ag-$TiO_2$3 within the range of 480-620 nm indicates an extensive coverage of Ag on the TiO_2 surface.

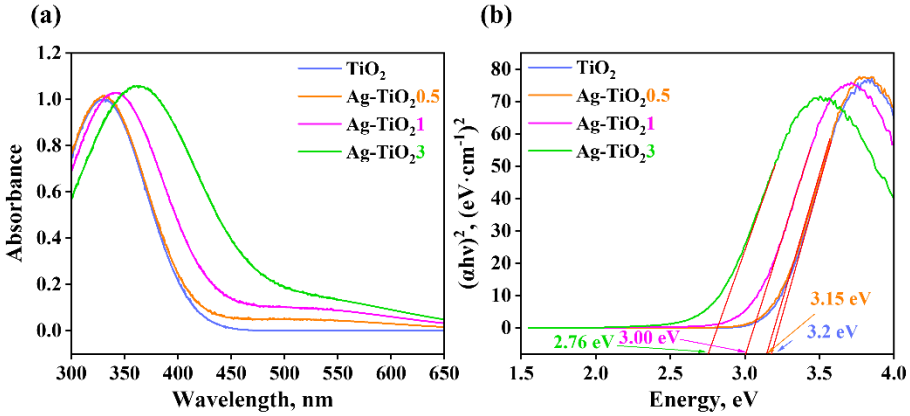

Figure 16. (a) UV-Vis absorbance spectra of TiO_2 and Ag-TiO_2 nanomaterials and (b) corresponding Tauc plots.

Figure 16 (b) shows the optical band gap of TiO_2 and Ag-TiO_2 nanomaterials, determined using the Tauc plot method. The deposition of Ag on TiO_2 reduced the band gap from 3.2 (pure TiO_2) to 3.15 eV, 3.00 eV, and 2.76 eV for Ag-$TiO_2$0.5, Ag-$TiO_2$1, and Ag-$TiO_2$3, respectively. An increase in Ag content in Ag-TiO_2 nanomaterials reduced the band gap energy, which is in good agreement with previously reported studies. For instance, Kumar and Gnanavel (2017) reported energy band gaps of 2.97 eV and 2.74 eV for Ag-doped TiO_2 nanomaterials with 3 wt% and 5 wt% Ag content, respectively. The observed decrease in the energy band gap due to Ag deposition primarily results from the localized SPR of Ag NPs. The presence of Ag NPs enables excitation with lower-energy light and enhances charge separation within TiO_2, thereby improving photocatalytic performance. In addition, the deposition of Ag NPs increases the number of accessible active sites, thereby enhancing the potential for photooxidation (Jadhav et al., 2025).

3.2. Photocatalytic degradation of fragment-type LDPE microplastics using TiO_2-clay nanocomposites

3.2.1. Effect of irradiation time on LDPE photocatalytic degradation

The photocatalytic degradation of fragment-type LDPE microplastics was monitored over time under neutral conditions (pH 7). *Figure 17* presents the degradation plots of LDPE over the studied period, where part (a) illustrates a decrease in LDPE concentration, while part (b) shows the mass loss (%) of LDPE. In the control group, an LDPE degradation test was

conducted without the addition of a catalyst. After 60 min of UV-A irradiation, the mass loss of LDPE increased sharply to 4.12%, with a less notable increase thereafter. The control experiments showed approximately 4.78% mass loss in LDPE after 480 min of UV irradiation, suggesting that plastic polymers can directly absorb photons, thereby generating excited states and initiating further oxidation. Earlier studies have also reported UV-induced alterations in microplastics, including changes in surface morphology and functional groups. For example, Ding et al. (2022) investigated PET and PVC microplastics under UV exposure and observed fine and large cracks on their surfaces, suggesting that the polymers underwent partial surface degradation due to decomposition. Although direct photodegradation of microplastics can be induced by specific light sources, complete degradation in natural environments is highly inefficient and proceeds slowly (Liu et al., 2019). In this study, the complete degradation of LDPE microplastics was not observed even in the presence of catalysts. However, the examined reaction system revealed trends and mechanistic differences in the degradation behavior of LDPE using TiO_2 NPs and TiO_2-clay nanocomposites.

Once the catalyst was introduced into the reaction system, the mass loss of LDPE notably increased. With bare TiO_2 NPs present, the mass loss of LDPE after 60 min was 13.29%, and it remained similar throughout the 480 min reaction period, reaching 14.66%. Meanwhile, LDPE showed slightly higher mass losses of 14.90% and 17.08% after 60 min with TiO_2-MMT and TiO_2-Kao, respectively. The mass loss of LDPE using TiO_2-Kao and TiO_2-MMT further increased with UV exposure time up to 480 min, reaching 21.25% and 28.36%, respectively. During the initial stage of the photodegradation process, the reduction in LDPE mass arises from the formation of low-molecular-weight, volatile, and soluble compounds (aldehydes, ketones, alcohols, carboxylic acids, ethers), which can eventually be broken down to CO_2 and H_2O (Ainali et al., 2021). These results suggested that prolonged UV-A irradiation enhances the photocatalytic degradation performance of LDPE, particularly when TiO_2-clay nanocomposites are used. Extended UV irradiation increases the number of molecular collisions between microplastics and the catalyst, enhances the catalyst's absorption capacity, and maintains a constant interaction with ROS in solution (He et al., 2023). In addition, differential scanning calorimetry (DSC) analysis has shown that the peaks of LDPE and HDPE broaden with increasing the time of UV irradiation, resulting in reduced crystallinity and the formation of amorphous regions that serve as initiation sites for photocatalytic degradation (Ainali et al., 2021).

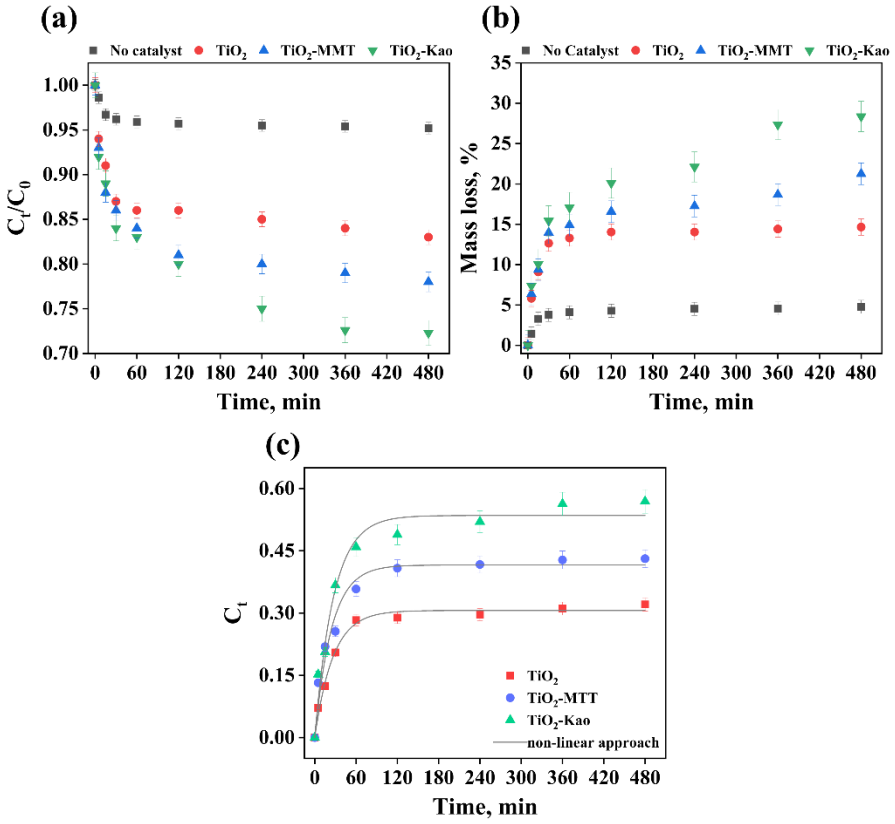

Figure 17. Photocatalytic degradation of LDPE over 480 min is expressed in terms of (a) LDPE concentration, (b) LDPE mass loss (%), and (c) pseudo-first-order kinetic plots.

Compared with bare TiO_2 NPs, TiO_2-clay nanocomposites exhibited improved photocatalytic degradation efficiency for LDPE microplastics. After 480 min, the mass loss of LDPE was approximately 1.5 times that of bare TiO_2 NPs when using TiO_2-MMT and nearly twice that when using TiO_2-Kao. A one-way ANOVA revealed a significant difference in LDPE mass loss among the tested catalysts (TiO_2, TiO_2-Kao, and TiO_2-MMT), $F(2;15) = 233.84$, $p < 0.001$, $\eta^2 = 0.96$. Post hoc comparisons using Tukey's test revealed that LDPE mass loss was significantly higher with TiO_2-Kao than with bare TiO_2 or TiO_2-MMT. The improved photocatalytic properties of TiO_2 could be attributed to the properties of kaolinite and montmorillonite, particularly their large surface area, porosity, high adsorption capacity, and availability of surface-active sites.

In comparison, montmorillonite has more layers, a larger surface area, and a higher cation exchange capacity than kaolinite. These characteristics of montmorillonite strongly enhance the photoactivity of TiO_2. However,

kaolinite contains more available surface hydroxyl groups at its edges, which contribute to the formation of oxygen vacancies in the metal oxide lattice. In addition, surface hydroxyl groups on kaolinite can interact with photogenerated h^+, resulting in enhanced formation of hydroxyl and superoxide radicals (Cao et al., 2021). These findings align with the study by Ding et al. (2022), which compared kaolinite and montmorillonite in the photodegradation system of PET and PVC. It indicated that kaolinite causes more pronounced peaks of $\cdot OH$ and $O_2^{\cdot -}$ radicals. Meanwhile, hydroxyl groups in montmorillonite are located between silica tetrahedral layers and have limited access to surface reactions.

The photocatalytic reaction kinetics were analyzed using the pseudo-first-order model to evaluate the reaction rate for all three catalysts (TiO_2, TiO_2-Kao, and TiO_2-MMT) (*Figure 17 (c)*). The pseudo-first-order model showed a good fit for all three catalysts, as indicated by the high coefficient of determination (R^2) from the C_t versus t plots, with the highest R^2 value observed for TiO_2-Kao ($R^2 = 0.984$) *(Table 9)*. In addition to the R^2 evaluation, the sum of squared errors (SSE) was calculated to assess model accuracy. Low SSE values further indicated a good agreement between experimental and predicted data, supporting the suitability of the applied kinetic model. The calculated degradation rate constant (k) for TiO_2, TiO_2-MMT, and TiO_2-Kao was found to be $3.79 \cdot 10^{-2}$ min^{-1}, $4.09 \cdot 10^{-2}$ min^{-1}, and $4.49 \cdot 10^{-2}$ min^{-1}, respectively. Based on the kinetic data and calculated reaction rate constants, TiO_2-Kao appears to be the most favorable catalyst for the studied degradation reaction.

Table 9. Kinetic parameters determined from the pseudo-first-order model for the photocatalytic degradation of LDPE fragments.

Catalyst	Non-linear approach			
	k, min^{-1}	**SD, σ**	**R^2**	**SSE**
TiO_2	$3.79 \cdot 10^{-2}$	$3.32 \cdot 10^{-3}$	0.983	0.001
TiO_2-Kao	$4.49 \cdot 10^{-2}$	$4.90 \cdot 10^{-3}$	0.984	0.001
TiO_2-MMT	$4.09 \cdot 10^{-2}$	$6.11 \cdot 10^{-3}$	0.967	0.006

Previous studies have also investigated the photocatalytic degradation of PE, LDPE, or HDPE in reaction systems containing TiO_2-based nanomaterials (*Table 10*). In this study, the highest degradation efficiency of LDPE in a neutral (pH 7) medium reached 28.36% after 480 min of UV irradiation with TiO_2-Kao. The achieved mass loss of LDPE was higher than in comparable studies. For example, Ariza-Tarazona et al. (2019) studied N-doped TiO_2 for photocatalytic degradation of HDPE microspheres and

achieved the mass loss of 2.86%. Similarly, Llorente-García et al. (2020) used N-TiO_2 for the photocatalytic degradation of HDPE microspheres and LDPE films, achieving mass losses of 1.38% and 4.65%, respectively. The limited degradation efficiency of PE has also been reported in earlier studies. Asghar et al. (2011) have found a PE mass loss of 14.37% after 300 hours of UV irradiation using metal-doped TiO_2. By contrast, only a few studies reached notably higher degradation efficiency of PE, such as 67.58% after 200 hours and 71.77% after 50 hours of light irradiation (Ariza-Tarazona et al., 2020; Zhang et al., 2024).

Not all studies provide the kinetics of microplastic degradation, making it difficult to directly compare the efficiency of different catalysts. However, pseudo-first-order kinetics are the most commonly reported in related studies, which emphasizes the consistent degradation pathways of the PE polymer chain in TiO_2-driven system (Kinyua et al., 2024; Tejaswini and Pathak, 2023).

Table 10. Photocatalytic degradation of PE, LDPE, and HDPE using TiO_2 based nanomaterials.

Type of catalyst	Type of MPs	Light source	Time, h	Removal efficiency	Kinetic model	References
Fe-TiO_2	PE	UV-A (365 nm)	300	13.49%	-	(Asghar et al., 2011)
Ag-TiO_2				13.75%		
Fe-Ag-TiO_2				14.34%		
N-TiO_2	HDPE microspheres	VIS light	8	2.86%	First order	(Ariza-Tarazona et al., 2019)
			20	6.40%		
C,N– TiO_2	HDPE microspheres	VIS light	50	71.77%	Pseudo first order	(Ariza-Tarazona et al., 2020)
N-TiO_2	LDPE film	VIS light	50	1.38%	First order	(Llorente-García et al., 2020)
	HDPE microsphere			4.65%		
TiO_2	LDPE film	UV-A (352 nm)	216	3.28%	Zero order	(Kaewkam et al., 2022)
		UV-C (254 nm)	216	17.30%		
GO-TiO_2	PE fragments	UV-A (350 nm)	8	50.46%	Pseudo first order	(Uogintė et al., 2023)

Type of catalyst	Type of MPs	Light source	Time, h	Removal efficiency	Kinetic model	References
TiO_2	LDPE film containing TiO_2	UV-A; UV-B (250 nm; 420 nm)	288	6.25%	First order	(Tejaswini and Pathak, 2023)
TiO_2 P25	LDPE microspheres	Xenon lamp, VIS light	6	19.89 %	-	(Jia et al., 2024)
$Bi_4Ti_3O_{12}$				28.35 %		
TiO_2	HDPE pellets	VIS light	350	2.0%	Pseudo first order	(Kinyua et al., 2024)
V-TiO_2				5.7%		
TiO2/WCT-AC	PE	VIS light	200	67.58 %	-	(Zhang et al., 2024)
TiO_2	LDPE fragments	UV-A (365 nm)	8	14.66%	Pseudo first order	This study
TiO_2-MMT				21.25%		
TiO_2-Kao				28.36%		

3.2.2. FTIR analysis of LDPE during photocatalytic degradation

The FTIR spectra of the studied LDPE microplastics are presented in *Figure 18* within the wavenumber range of 4000–680 cm^{-1}. The observed FTIR spectra of untreated LDPE showed characteristic peaks typical of its nature. An absorption band around 2800–3000 cm^{-1} is attributed to symmetric and asymmetric CH_2 stretching vibrations. A strong peak observed at 1463 cm^{-1} corresponds to CH_2 bending vibrations, and a peak at 1378 cm^{-1} is ascribed to CH_3 bending vibrations (Jia et al., 2024). Even untreated LDPE microplastics exhibited slight alterations in their FTIR spectra, most likely due to the processing, storage, or handling. LDPE typically exhibits two distinct absorption bands in the 2800–3000 cm^{-1} region, corresponding to the asymmetric (at ~2915 cm^{-1}) and symmetric (at ~2845 cm^{-1}) stretching vibrations of CH_2 groups (Jung et al., 2018). However, the studied LDPE microplastics appear to exhibit a single broad band in this region, as previously indicated. This broadening and merging of untreated LDPE peaks can result from LDPE heterogeneity, including variations in crystallinity, branching, or minor oxidative changes that may occur during manufacturing.

Spectral changes in the LDPE polymer chain are observed after 60 min of photocatalytic degradation, particularly with TiO_2-MMT and TiO_2-Kao. A new functional group in LDPE was identified at 2634 cm^{-1}, which is attributed to C–H stretching of aldehyde groups. A weak peak at 2023 cm^{-1} is ascribed

to C–O stretching vibration. A formation of a broad absorption band was observed at 1850 cm^{-1} to 1700 cm^{-1}, corresponding to the C=O stretching in carboxylic acids or ketones. In particular, the appearance of oxygen-containing groups indicates a successful oxidation of the polymer chain. These results are supported by earlier studies, which indicated the oxygenated groups within the LDPE polymer chain in regions of 1700–1760 cm^{-1}, 3600–3610 cm^{-1}, and 1100–1300 cm^{-1}, corresponding to carboxyl groups, hydroperoxides, peroxides, alcohols, and ethers (Ningsih et al., 2024; Tofa et al., 2019). Under continued irradiation, LDPE may undergo further degradation, leading to the formation of oxygen-containing groups, particularly in the range of 3600 cm^{-1} to 3100 cm^{-1}. This range corresponds to the O–H stretching region of hydroxyl groups, indicating the formation of additional hydroperoxides and alcohols (Ali et al., 2016; Jia et al., 2024).

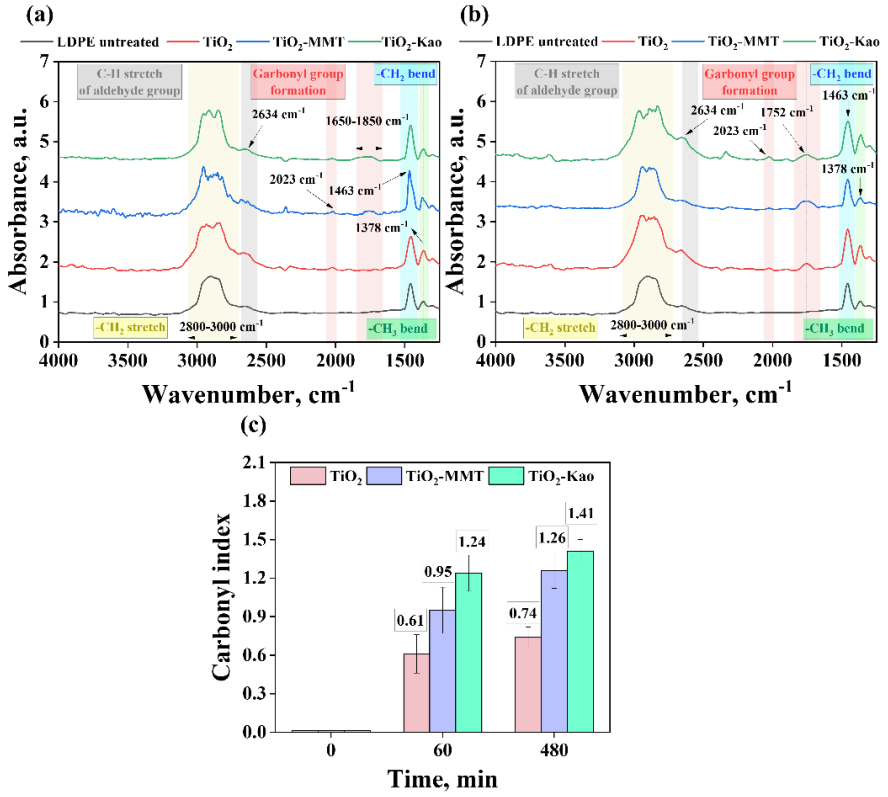

Figure 18. FTIR spectra for LDPE (a) after 60 min of UV irradiation, (b) after 480 min of UV irradiation, and (c) carbonyl index (CI).

After 480 min of photocatalytic reaction, the LDPE spectra exhibited slight broadening of characteristic peaks, indicating chain scission, branching, and the formation of more CH_2 and CH_3 groups within the polymer chain. The

broadening of the spectra also suggests a decrease in polymer crystallinity, leading to more sensitive regions for photo-oxidation. The intensity of the absorption band at 1752 cm^{-1} (C=O) increased notably after 480 min of reaction. In addition, the FTIR spectra revealed distinct differences in the evolution of carbonyl-containing species depending on the catalyst used. In the presence of bare TiO_2, only a slight formation of the carbonyl absorption band was detected after 60 min of UV irradiation. A more pronounced characteristic carbonyl band appears only after 480 min of exposure. In contrast, when TiO_2-clay nanocomposites were used, the formation of a carbonyl group was already evident after 60 min of UV irradiation, as indicated by the corresponding absorption band in the region of 1650–1850 cm^{-1}. Furthermore, the intensity of this band increased with irradiation time up to 480 min. These results imply that TiO_2-MMT and TiO_2-Kao exhibit higher photocatalytic efficiency, leading to earlier and more pronounced carbonyl group formation.

The CI was calculated to quantify the extent of oxidative degradation of LDPE microplastics during UV irradiation. As shown in *Figure 18 (c)*, CI values were monitored at 60 min and 480 min, showing a consistent increase throughout the irradiation period. The CI values for bare TiO_2 slightly increased from 0.61 ± 0.15 to 0.74 ± 0.08 over 480 min, whereas for TiO_2-MMT and TiO_2-Kao, the CI values were higher and increased from 0.95 ± 0.18 to 1.26 ± 0.14 and from 1.24 ± 0.14 to 1.41 ± 0.09, respectively. Previous studies on the photocatalytic degradation of LDPE microplastics indicated that CI values typically ranged from 0.35 to 1.60 (Sura and Nain, 2024; Tofa et al., 2019). The degree of degradation, as reflected by CI, was strongly associated with degradation time and the chosen photocatalyst. In this study, the TiO_2-Kao catalyst showed a notably shorter reaction time and a comparatively high CI value, further confirming its suitability and promising potential for the photocatalytic degradation of microplastics.

3.2.3. Effect of LDPE-to-catalyst ratio

The effect of catalyst amount on the reaction system was investigated by adjusting the LDPE-to-catalyst ratio to 2:1, 1:1, and 1:2, as shown in *Figure 19*. The degradation profiles of LDPE microplastics indicated a clear dependence of photocatalytic performance on the catalyst loading. When the catalyst dosage was increased from 10 mg to 40 mg, the degradation efficiency of LDPE increased from 9.27% to 22.59% for bare TiO_2 NPs, from 10.99% to 23.03% for TiO_2-MM, and from 14.55% to 25.98% for TiO_2-Kao. This enhancement can be attributed to the increased catalyst surface area,

which provides more available active sites and facilitates the generation of more ROS, such as hydroxyl and superoxide radicals (Tan et al., 2023). When the catalyst dosage was lower than that of LDPE, photocatalytic degradation was at least effective. A one-way ANOVA was used to assess the effect of varying catalyst amounts on LDPE degradation efficiency. The analysis indicated that the choice of catalyst had its greatest impact when the LDPE-to-catalyst ratio was set to 2:1 ($F(2;14) = 66.416$, $p < 0.001$, $\eta^2 = 0.905$). At this LDPE-to-catalyst ratio, pairwise comparison confirmed that each catalyst differed significantly from the others. In contrast, at the LDPE-to-catalyst ratio of 1:2, where the catalyst amount is double, the influence of catalyst type is decreased ($F(2;13) = 13.441$, $p < 0.001$, $\eta^2 = 0.674$). While TiO_2-Kao remains more effective than other catalysts, at the ratio 1:2, there was no significant difference between bare TiO_2 NPs and TiO_2-MMT ($p = 0.830$).

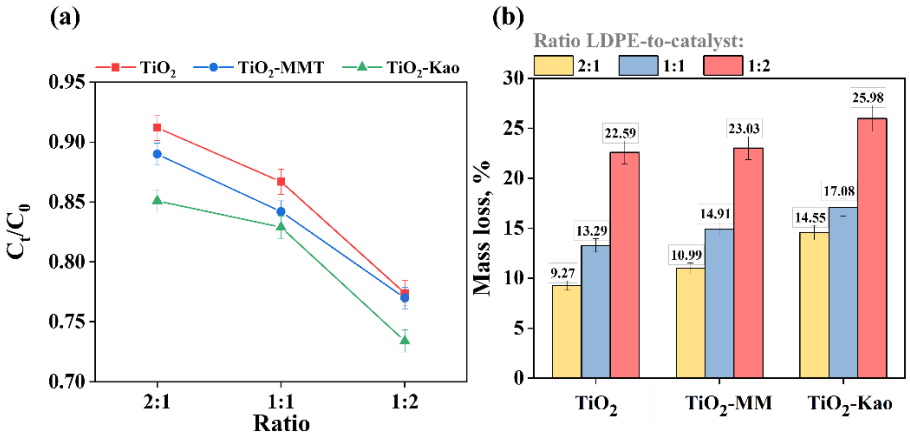

Figure 19. Influence of LDPE-to-catalyst ratio on LDPE degradation. The degradation efficiency is expressed in terms of (a) LDPE concentration and (b) mass loss (%).

The findings regarding optimal catalyst dosage in this study align with previously reported values. Similarly, Uogintė et al. (2023) found that increasing the catalyst-to-pollutant ratio to 2:1 led to a 6.5% increase in mass loss of PE microplastics. Another study on LDPE degradation found that LDPE mass loss increased with catalyst concentration, rising from 500 ppm to 1000 ppm. Meanwhile, when the catalyst dosage was further increased from 1000 ppm to 1500 ppm, the mass loss was reduced by 6.68% (Tan et al., 2023). The decrease in degradation efficiency can be attributed to increased solution turbidity, which reduces light penetration and causes light scattering, as well as particle aggregation, which controls the total surface area available for the photocatalytic reactions (Abdel-Khalek et al., 2018).

The catalyst dosage in the reaction system can control photocatalytic performance, indicating that it is a critical parameter. Consequently, researchers must determine an optimal dosage to maximize the production of reactive radicals while ensuring that light can still effectively penetrate the reaction solution. Maintaining the optimal catalyst dosage is important to prevent catalyst waste and achieve a cost-efficient microplastic removal process.

3.2.4. Effect of solution pH

The photocatalytic degradation of LDPE microplastics is strongly influenced by solution pH, with acidic conditions significantly more effective than neutral or alkaline conditions. In this study, the photocatalytic degradation of LDPE was investigated over a pH range of 3–11 (*Figure 20*). The highest degradation efficiency was achieved at pH 3, with LDPE mass loss of 24.67% for bare TiO_2, 25.28% for TiO_2-MMT, and 30.96% for TiO_2-Kao over 60 min of UV irradiation. At a neutral pH of 7, the degradation efficiency was approximately half that observed under acidic conditions, yielding mass losses of 13.29%, 14.56%, and 17.08% for the respective catalysts. Conversely, the lowest degradation rates were observed under alkaline conditions at pH 11, where mass losses decreased sharply to 4.75% for TiO_2, 6.67% for TiO_2-MMT, and 7.41% for TiO_2-Kao. The high concentration of hydrogen ions (H^+) in acidic solutions promotes the formation of ROS by neutralizing the permanent negative charge on the surface, thereby improving contact between microplastics and the catalyst (Ariza-Tarazona et al., 2020). After LDPE photocatalytic degradation, the pH changes at different initial pH values were also measured (*Table 11*). The observed decrease in initial pH during LDPE degradation suggested the formation of acidic intermediates.

Table 11. pH variation during 60 minutes photocatalytic degradation of LDPE at initial pH 3 – 11 with different catalysts (no catalyst, TiO_2, TiO_2-MMT, TiO_2-Kao).

Initial pH / **Catalyst**	3	5	7	9	11
No catalyst	3.17	5.67	6.87	7.54	10.38
TiO_2	3.31	4.33	5.84	6.18	7.85
TiO_2-MMT	3.54	4.51	5.72	7.58	9.42
TiO_2-Kao	3.40	4.47	5.62	6.55	7.85

In this system, the photocatalytic degradation of LDPE is primarily driven by the generation of ROS via photoexcitation of TiO_2 NPs. The PZC of TiO_2 lies between 5.55 and 6.50 (Maleki et al., 2023). Acidic conditions induce a positive charge on the TiO_2 surface. This charge enhances the electrostatic attraction toward the negatively charged LDPE particles, thereby facilitating interaction and interfacial radical attack. In addition, the LDPE particles typically exhibit a negative surface charge in aqueous solution, therefore, a positively charged catalyst is expected to favor the reaction. In contrast, neutral and alkaline environments lead to electrostatic repulsion between the negatively charged surfaces of both TiO_2 and LDPE microplastics. Under strongly alkaline conditions, elevated hydroxyl ion concentrations further inhibit degradation by competing with LDPE for available active sites on the TiO_2 surface, thereby reducing photocatalytic performance (Huang et al., 2022). Meanwhile, at a pH below 7, the reaction solution contains a high concentration of H^+ and H_3O^+, which is why competitive adsorption at the catalyst active sites is no longer present.

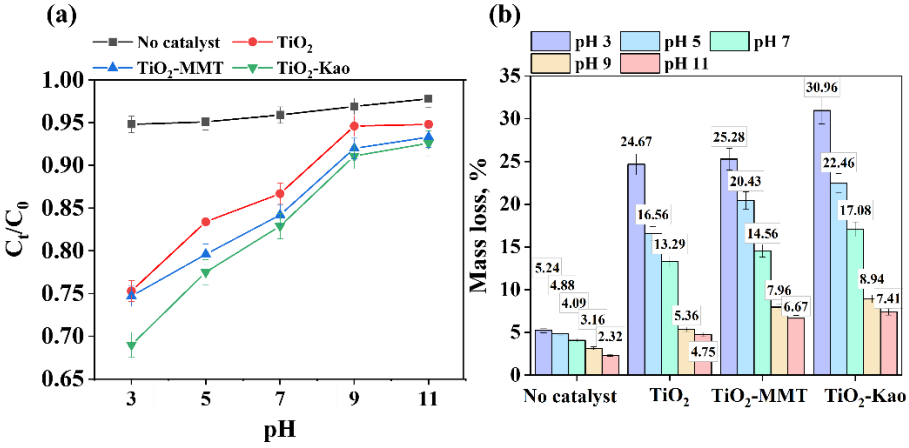

Figure 20. Influence of solution pH on LDPE degradation. The degradation efficiency is expressed in terms of (a) LDPE concentration and (b) LDPE mass loss (%).

TiO_2-Kao and TiO_2-MMT exhibited greater photocatalytic efficiency than bare TiO_2 NPs among the tested catalysts under pH 3–11. The one-way ANOVA showed that the effect of catalyst type was most significant under acidic conditions. At pH 3, the statistical analysis showed significant differences between catalysts ($F(2;6) = 23.426$; $p = 0.001$, $\eta^2 = 0.886$). Meanwhile, the Post-hoc Tukey tests revealed that TiO_2-Kao was statistically superior to both bare TiO_2 ($p = 0.002$) and TiO_2-MMT ($p = 0.003$). Under acidic conditions, no significant difference was found between TiO_2 NPs and TiO_2-MMT ($p = 0.903$). While differences among catalysts remained

significant under alkaline conditions, they were slightly narrower ($F(2;6) = 8.276$; $p = 0.019$; $\eta^2 = 0.734$). Particularly, a significant difference was found between TiO_2 and TiO_2-Kao ($p = 0.017$), while no significant difference was found between TiO_2-Kao and TiO_2-MMT ($p = 0.075$) and between TiO_2 and TiO_2-MMT ($p = 0.476$). These results indicated that alkaline conditions similarly affect used catalysts, resulting in comparable photocatalytic activity performance. The results of this study are consistent with those reported in previous research. Zhang et al. (2011) found that TiO_2-Kao nanocomposites exhibited higher photocatalytic activity than commercial TiO_2 NPs. In particular, acidic and neutral reaction conditions enhanced the activity of TiO_2-Kao. Huang et al. (2022) observed that high pH inhibited the ability of Co/Mn-Kaolin to remove microplastics, as hydroxyl ions competed for available active sites. When kaolinite or montmorillonite is subjected to acidic conditions, the edges of the clay surface become positively charged due to the protonation of their hydroxyl groups (Al-OH sites at the edges). Meanwhile, under alkaline conditions, hydroxyl groups deprotonate, leading to a negatively charged surface at the clay edges (Kumari and Mohan, 2021). Surface edges become positively charged primarily at pH values below approximately 6.0–6.5, which corresponds to the PZC of both clay minerals. This phenomenon explains the most effective photocatalytic degradation of LDPE observed in highly acidic conditions, as it enhances the electrostatic attraction between the clay-containing catalyst and the negatively charged LDPE surface. In addition, the acidic environment promotes expansion of the basal spacing in clay minerals, which ultimately improves their adsorption capacity and accelerates the formation of ROS (Ding et al., 2022).

3.2.5. Effect of solution ionic strength

The effect of IS on the efficiency of the photocatalytic degradation reaction was examined in the presence of a NaCl solution (*Figure 21*). The IS of the reaction solutions was adjusted from 0.05 $molL^{-1}$ to 0.5 $molL^{-1}$. The photocatalytic degradation of LDPE microplastics decreased as the IS of the solution was increased, with mass loss at an IS of 0.5 mol L^{-1} roughly half that observed in distilled water. When the IS was raised from 0 to 0.5 $molL^{-1}$ using NaCl, the mass loss of LDPE dropped from 13.29% to 7.82% for bare TiO_2, 14.56% to 9.48% for TiO_2-MMT, and 17.08% to 8.31% for TiO_2-Kao. The greatest reduction in mass loss, by 8.77%, was achieved with TiO_2-Kao. Meanwhile, when using bare TiO_2 NPs and TiO_2-MMT, the mass loss decreased by approximately 5%. IS can affect the behavior of LDPE in aqueous solutions and alter the characteristics of nanomaterials.

A decrease in LDPE degradation efficiency with increasing IS is primarily attributed to electrostatic charge screening by Na^+, which limits the aqueous stability of microplastics. The electrostatic charge screening effect of the cations reduces the Debye radius and minimizes repulsive forces between negatively charged particles. As repulsive forces decrease, the Van der Waals attraction becomes dominant, causing microplastics to aggregate into larger clusters. The resulting aggregates have an increased hydrodynamic diameter, which reduces the particle diffusion rate and overall mobility (Lu et al., 2018). For example, the hydrodynamic diameter of microplastics found in seawater was twice that of those from groundwater (Singh et al., 2019). The size of LDPE particles plays an important role in their behavior in solutions of varying IS, as smaller microplastics are more prone to destabilization by metal-cation adsorption than larger ones. This could be explained by the increase in Gibbs free energy associated with smaller particles (Song et al., 2019). The behavior of LDPE microplastics in a reaction solution at different IS can help improve understanding of the photocatalytic degradation of these particles in wastewater, where IS ranges from 0.003 to 0.1 $molL^{-1}$ (Singh et al., 2019).

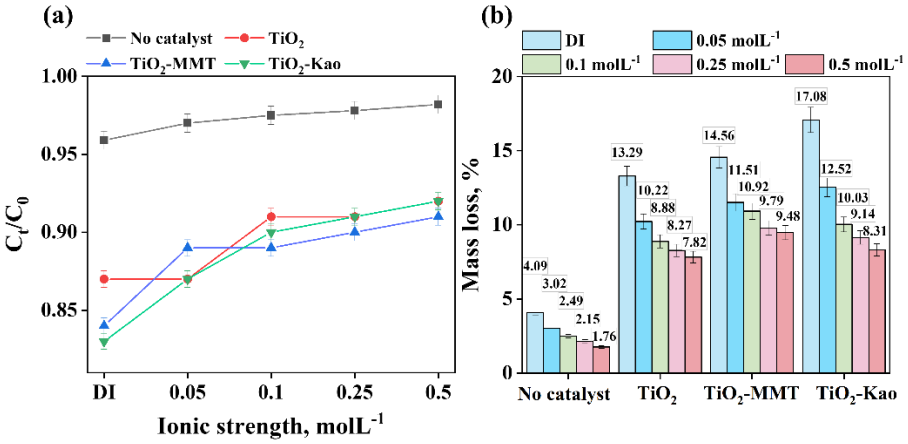

Figure 21. Influence of solution ionic strength on LDPE degradation. The degradation efficiency is expressed in terms of (a) LDPE concentration, and (b) LDPE mass loss (%).

Across different IS conditions, LDPE mass loss (%) exhibited a consistent pattern for all three catalysts examined in this study. A one-way ANOVA was used to evaluate whether significant differences in the degradation system driven by TiO_2, TiO_2-Kao, or TiO_2-MMT occurred as the salt concentration in the solution increased. Differences in degradation performance among the catalysts diminish as NaCl concentration increases, with significant differences observed only at the lowest concentration

(0.05 $molL^{-1}$). At this concentration, post-hoc comparisons indicated differences in LDPE degradation between bare TiO_2 and TiO_2-Kao ($p = 0.003$), while all other catalyst pairs remained statistically similar. The lack of a notable difference between TiO_2 and TiO_2-MMT may be attributed to the influence of IS on montmorillonite. Previous studies have shown that increasing IS reduces the effective repulsion between charged montmorillonite particles, promoting faster aggregation compared to kaolinite particles (Doi et al., 2019). As the IS increases to 0.1 $molL^{-1}$ and 0.5 $molL^{-1}$, the results become non-significant ($p = 0.149$ and $p = 0.061$). This could be attributed to the presence of Na^+ and Cl^- ions in the solution, which can alter the catalyst's surface characteristics and possibly diminish the distinctions between the synthesized catalysts.

TiO_2-Kao and TiO_2-MMT showed slightly higher degradation performance than bare TiO_2 NPs under varying IS conditions. While the overall clay surface has a negative charge, the edges of clay minerals are often positively charged. These edges can effectively absorb the negatively charged LDPE microplastics. Moreover, clay minerals act as supports that stabilize TiO_2 NPs against salt-induced aggregation, thereby maintaining a higher active surface area and providing better interaction between LDPE and TiO_2-Kao or TiO_2-MMT (Singh et al., 2019). The presence of ions in the reaction solution influences the electrostatic properties of TiO_2 NPs. Increased concentration of Na^+ and Cl^- from NaCl reduces the Debye length and electrostatic repulsions between particles. This leads to the formation of TiO_2 aggregates, which eventually reduce surface reactions between LDPE microplastics and the catalyst, explaining the reduction in mass loss at higher salt concentrations. In addition, the zeta potential of TiO_2 NPs diminishes as the IS increases, further contributing to particle aggregation. For example, studies have shown that TiO_2 NPs of 40 nm in size (which is comparable to the nanomaterial size employed in this work) can form clusters as large as 180 nm at an IS of 0.001 $molL^{-1}$ and pH of 7 (Lecoanet et al., 2004). Other researchers indicated that IS also controls the behavior of ROS generated by TiO_2. Cl^- ions can interfere with LDPE degradation pathways, because hydroxyl radicals may react with Cl^- to produce chlorine radicals ($Cl^{\cdot}$). This prevents the hydroxyl radicals from directly attacking the LDPE polymer chain, thereby reducing the overall degradation efficiency (Wang et al., 2022).

3.2.6. Chapter conclusion

The formation of TiO_2-clay nanocomposites significantly enhanced the photocatalytic degradation of 300 μm, fragment-type LDPE microplastics in an aqueous medium. The band gap energy of bare TiO_2 NPs was reduced from 3.10 eV to 2.95 eV for TiO_2-MMT and to 2.88 eV for TiO_2-Kao. Kinetic analysis was fitted to a pseudo-first-order model, in which TiO_2-Kao exhibited the highest rate coefficient, $4.49 \cdot 10^{-2}$ min^{-1}. After 480 min of UV-A irradiation, the maximum mass loss of LDPE microplastics was 28.36% with TiO_2-Kao, whereas TiO_2-MMT and bare TiO_2 NPs achieved mass losses of 21.25% and 14.66%, respectively. Spectroscopic analysis further validated the chemical transformation of LDPE microplastics, with the highest CI value of 1.41 for TiO_2-Kao, indicating successful oxidation. These findings suggest TiO_2-Kao as a sustainable and cost-efficient catalyst for microplastic removal.

The study of optimal degradation conditions revealed that degradation is most efficient under strongly acidic conditions (pH 3), where mass loss reached 30.96% with TiO_2-Kao after only 60 min of UV-A irradiation, whereas at pH 11 it dropped to 7.41%. Furthermore, doubling the catalyst amount from 20 mg to 40 mg increased LDPE mass loss by approximately 10%. Conversely, increasing the IS to 0.5 $molL^{-1}$ significantly reduced degradation efficiency, decreasing the mass loss of LDPE from 17.08% (in deionized water) to 8.31%. The systematic analysis of reaction parameters indicated that while TiO_2-clay nanocomposites are promising for microplastic remediation, real-world success requires optimizing environmental variables to maximize mass loss and overcome inhibitory aquatic factors.

3.3. Photocatalytic degradation of film-type LDPE using Ag-TiO_2 nanomaterials

3.3.1. Characterization of pristine LDPE films

In this study, commercially available LDPE plastic mulch films in black and transparent colors were purchased from a local market (*Figure 22 (a, c)*). SEM imaging was used to analyze surface morphology and revealed distinct differences between black and transparent LDPE films. Black LDPE films contain roughness, wrinkles, and irregularities, while transparent LDPE films exhibited a uniform, smooth surface texture, without detectable cracks or mechanical damage, as presented in *Figure 22 (b, d)*.

The characteristic absorption bands of pristine LDPE films were studied by ATR-FTIR spectroscopy. Absorption bands at ~2916 cm^{-1} and

~2845 cm^{-1} correspond to asymmetric and symmetric CH_2 stretching vibrations, respectively. The band at ~1462 cm^{-1} indicates CH_2 bending vibrations, while the peak near 717 cm^{-1} arises from CH_2 rocking vibrations (*Figure 22 (e, f)*). The observed absorption bands in both black and transparent LDPE films correspond to characteristic LDPE bands (Jung et al., 2018). However, noticeable differences are evident between black and transparent LDPE films. The black LDPE film shows an extra peak at 873 cm^{-1}, which is linked to vinyl groups (C=C) (Miranda et al., 2021). In transparent LDPE films, several spectral changes were observed. Notably, there was a broadening of the absorption band in the 892 cm^{-1} to 770 cm^{-1} region, which is attributed to C=C stretching vibrations. Additionally, a broad absorption band appeared in the range of 3600–3200 cm^{-1}, indicating the formation of alcohol (O–H) groups. Furthermore, a new peak was detected at 1661 cm^{-1}, suggesting the presence of carbonyl (C=O) groups. Oxygen-containing groups can be found even in untreated pristine LDPE films, typically appearing as weak absorption bands. These groups may arise from manufacturing processes, such as oxidative reactions during polymerization, or from additives that are incorporated into the polymer matrix (Wang et al., 2022). Manufacturers produce LDPE films using thermal conversion processes, most commonly by film blowing (tubular extrusion) or sheet extrusion. During the extrusion process, oxygen-containing groups are introduced into the LDPE chain. This occurs due to a combination of thermal stress, mechanical strain, and the presence of oxygen. Commercial plastic films exhibit changes in the C=O and fingerprint regions due to the formation of oxidation products, particularly ketones, aldehydes, acids, and esters. Oxygen-containing groups in pristine LDPE may influence the photocatalytic degradation, however, this study emphasizes the role of film size and color.

Plastic films, particularly LDPE films, are used in agriculture for a wide range of applications, including mulching films, greenhouses, silage, low-tunnel, and irrigation systems. Agricultural polymeric materials contain a broad range of chemical additives, which make up approximately 15% of their total weight, depending on the specific material and its application. To date, typical chemical agents found in agricultural LDPE films are UV absorbers, light stabilizers, carbon black, pigments, antioxidants, anti-blocking agents, and surfactants.

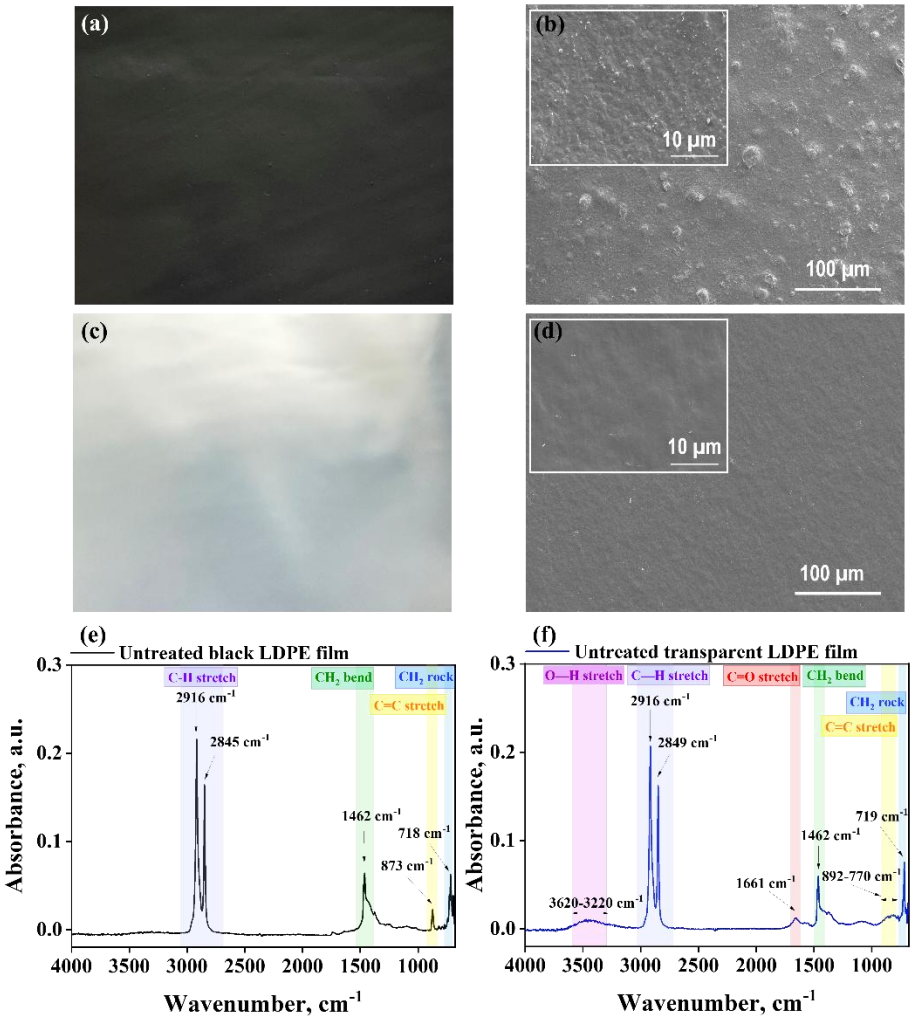

Figure 22. Pristine LDPE films, along with SEM images and ATR-FTIR spectra, in which a, b, and e indicate black films, and c, d, and f represent transparent films.

The XRF analysis reveals the chemical composition of inorganic elements in LDPE films, which are linked to the additives, fillers, and pigments used during processing (*Table 12*) (Carrieri et al., 2025). Transparent films contain only trace levels (less than 0.05%) of elements such as Na, Al, Si, Cl, Ca, and Zn. For producing transparent LDPE films, only pure or low-additive LDPE is used. To preserve this transparency, manufacturers may incorporate only very small quantities of specific substances, such as thermoplastic starch, silica aerogel, or ZnO (Yang et al., 2022). In contrast, black LDPE films exhibited a much higher number of inorganic elements, most notably Ca (25.2776%) and Ti (5.0056%). The elements Mg, Al, Si, Fe, and Zn each have a total weight higher than 0.05%.

Additionally, other inorganic elements, including Na, K, Ni, Br, Sr, and Ba, were found in black LDPE films, each with a total weight of less than 0.05%. Ca, alongside Mg, Al, and Si, serves as an antiblocking agent that induces surface roughness and minimizes film adhesion (Vallada et al., 2020). The detection of antiblocking agents in black LDPE films is consistent with SEM images, which showed surface heterogeneity and roughness. The presence of Ti in black LDPE films is attributable to TiO_2, which is often used as a UV stabilizer, particularly for outdoor applications. In addition, other inorganic elements detected in black films originate from various minor additives introduced during polymer production and processing.

Table 12. Elemental assessment of black and transparent LDPE films.

Element	Black LDPE film Concentration, wt%	Transparent LDPE film Concentration, wt%
O	3.666	0.098
Na	< 0.050	< 0.050
Mg	0.126	-
Al	0.072	< 0.050
Si	0.166	< 0.050
Cl	0.191	< 0.050
K	< 0.050	-
Ca	25.278	< 0.050
Ti	5.006	-
Fe	0.194	-
Ni	< 0.050	-
Zn	0.061	< 0.050
Br	< 0.050	-
Sr	< 0.050	-
Ba	< 0.050	-

Several other properties of microplastics also influence the degradation behavior of LDPE, including molecular weight, molecular weight distribution, and production process. In this study, such data were unavailable for the commercially obtained LDPE films, as the suppliers did not disclose them. Typically, LDPE films exhibit a weight-average molecular weight between $1 \cdot 10^5$ and $4 \cdot 10^5$ g/mol (Azmi et al., 2019). LDPE films with a lower molecular weight (less than 233.000 g/mol) are more prone to degradation, whereas higher molecular weights (around 430.000 g/mol) provide greater stability (Garnai Hirsch et al., 2019). It is worth noting that while LDPE film color (such as black or transparent) indicates different additive profiles, it does not necessarily correspond to significant differences in molecular weight.

3.3.2. Control study of LDPE film photodegradation

The control study of LDPE films was conducted by exposing black and transparent LDPE films (size 1×1 mm and 3×3 mm) to UV-A irradiation for up to 960 min in the absence of a catalyst. The results after 960 min of UV irradiation indicated negligible mass loss of LDPE films, with values below 0.55% for 1×1 mm and 0.35% for 3×3 mm films, suggesting that considerable degradation is more likely to occur in systems containing a catalyst (*Figure 23*). In addition to the present study, Llorente-García et al. (2020) reported that no significant mass reduction of LDPE films was observed even after 50 hours of UV exposure without a catalyst.

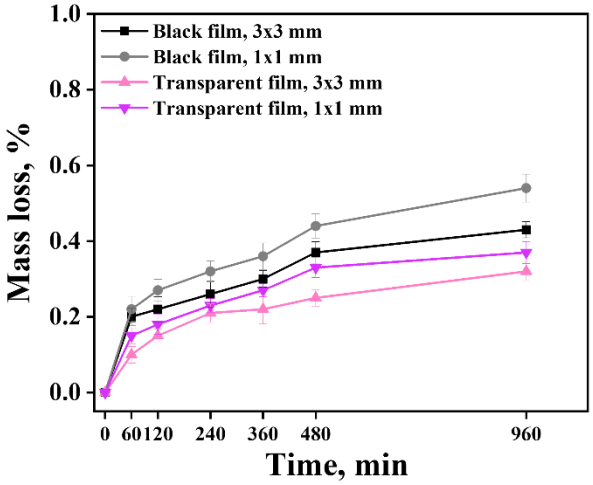

Figure 23. Mass loss of LDPE films after 960 min of UV-A irradiation without the use of a catalyst.

SEM analysis of LDPE films after 960 min of photodegradation revealed no notable surface alterations (*Figure 24)*. Black LDPE films maintained surface roughness comparable to that of untreated samples, with no visible new irregularities, such as cracks or cavities. For transparent LDPE films, the surface remained flat and smooth, similar to untreated films.

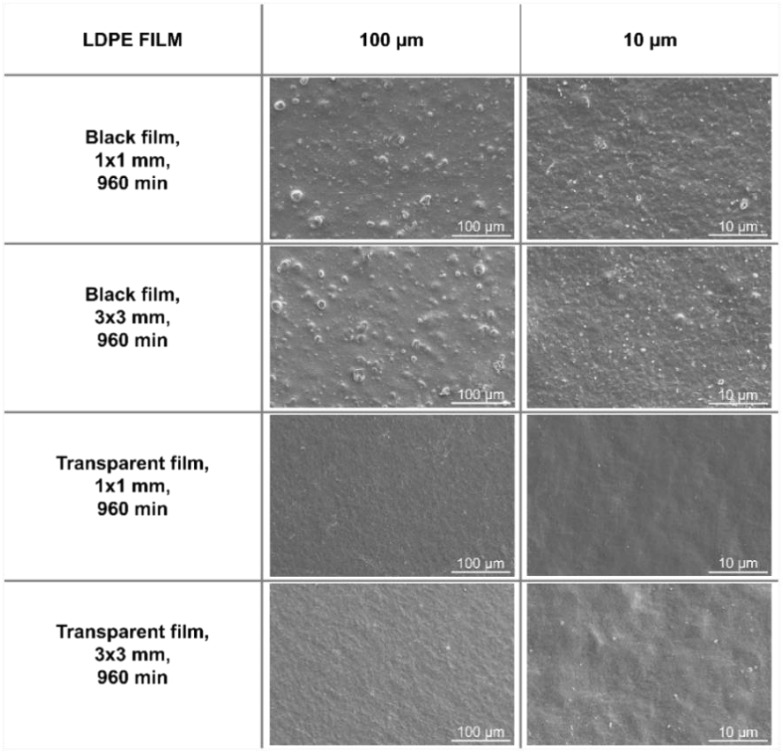

Figure 24. SEM micrographs of LDPE films after 960 min of UV-A irradiation without the use of a catalyst.

The results from mass loss measurements and SEM imaging are further supported by FTIR spectral analysis. ATR-FTIR analysis indicated no spectral changes in LDPE films after 960 min of UV light exposure (*Figure 25*). The characteristic peaks of black and transparent LDPE films at ~718 cm^{-1}, ~1462 cm^{-1}, ~2845 cm^{-1}, and ~2916 cm^{-1} stayed sharp and well-defined as observed in untreated LDPE films. Doğan (2021) reported similar findings, noting that LDPE films did not undergo any chemical transformation even after a week of exposure to UV-B and UV-C light. The physicochemical analysis of LDPE films after photodegradation suggested that light absorption alone does not affect the reaction system under these particular conditions. Although microplastics degrade slowly in the environment, they undergo long-term changes in their physicochemical properties. After 11 months of weathering, PS and PE microplastics showed morphological alterations, fragmentation, and new absorption peaks (Liu et al., 2019). Nonetheless, these degradation processes lack efficiency, thus, utilizing catalysts is an essential method for improving the photodegradation of microplastics.

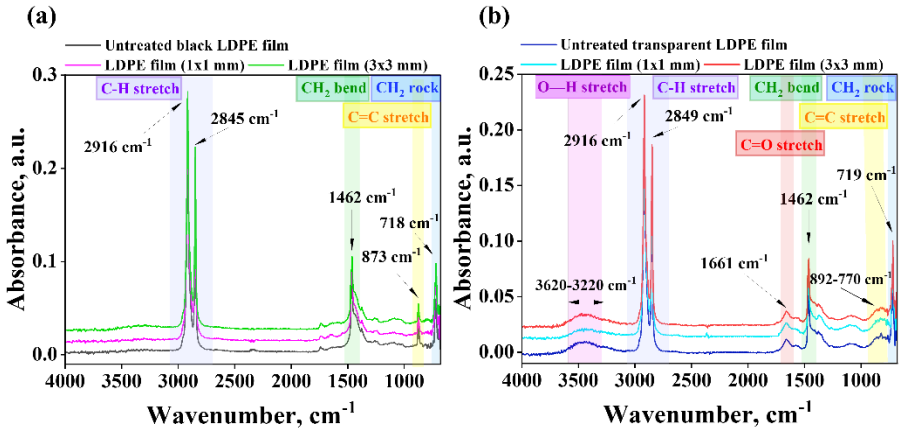

Figure 25. ATR-FTIR spectra of LDPE films after 960 min of UV-A irradiation without the use of a catalyst (a) black LDPE films and (b) transparent LDPE films.

3.3.3. Photocatalytic degradation of LDPE films using Ag-TiO_2

This study explored the photocatalytic degradation of four types of LDPE films under UV-A irradiation over a reaction period of 60–960 min. Particular attention was given to evaluating and comparing the effects of varying Ag content in Ag-TiO_2 catalysts. The presence of a catalyst enhanced the degradation efficiency of the studied LDPE films over 960 min of UV-A irradiation (*Figure 26)*. Higher LDPE film mass loss was achieved using Ag-$TiO_2$1 and Ag-$TiO_2$3 compared to bare TiO_2 NPs and Ag-$TiO_2$0.5. The highest recorded mass loss was 7.14% ± 0.11% with Ag-$TiO_2$1 and 9.88% ± 0.20% with Ag-$TiO_2$3, both observed in black LDPE films (1×1 mm) after 960 min. For the same black LDPE films, the mass loss with bare TiO_2 NPs was 3.08% ± 0.15%, while with Ag-$TiO_2$0.5 it reached a slightly higher degradation efficiency of 4.52% ± 0.13% over 960 min of UV-A exposure. Other studies have similarly reported that bare TiO_2 NPs exhibited low degradation efficiency, emphasizing the limitations of unmodified TiO_2 in degrading microplastics. Tejaswini and Pathak (2023) reported a mass loss of 6.25% for LDPE films, while Kaewkam et al. (2022) found a slightly lower value of approximately 3.28%.

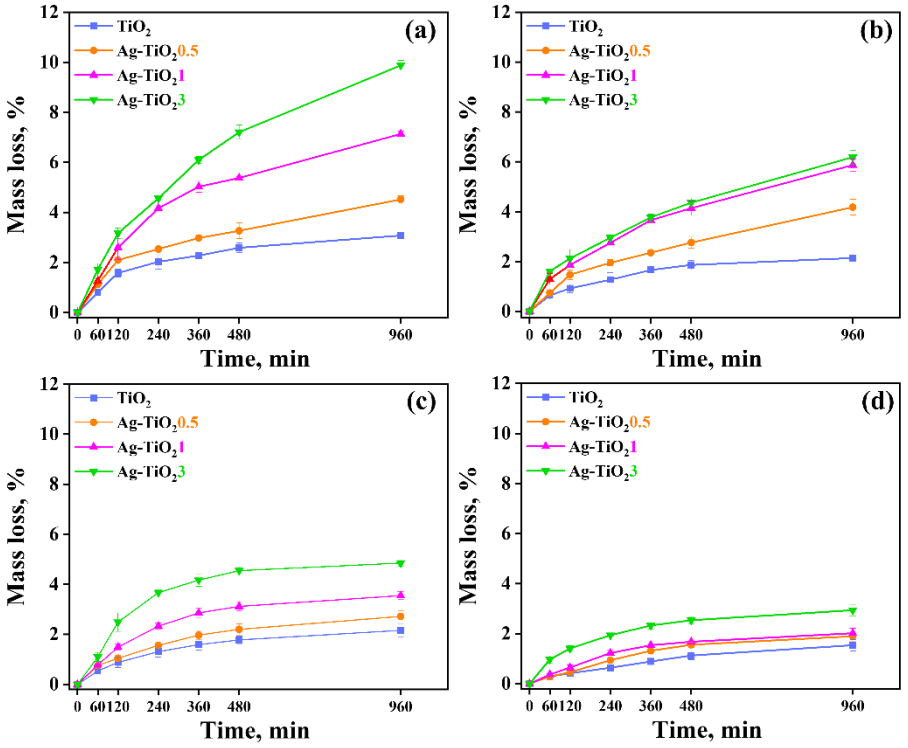

Figure 26. Photocatalytic degradation of LDPE films over 960 minutes with TiO_2, Ag-$TiO_2$0.5, Ag-$TiO_2$1, and Ag-$TiO_2$3 catalysts (a) black film 1×1 mm, (b) black film 3×3 mm, (c) transparent film 1×1 mm, and (d) transparent film 3×3 mm.

As discussed in the literature review (subsection *1.3.4*), metal doping is an effective approach to address the limitations of TiO_2. The findings of this study indicate that Ag doping enhances the photocatalytic performance of TiO_2 in degrading LDPE films, with higher Ag content corresponding to greater degradation efficiency. For example, when the Ag-$TiO_2$3 catalyst was used, the mass loss of black LDPE films (1×1 mm) was 4.5 times higher than that observed with bare TiO_2 NPs and twice as high as that obtained with Ag-$TiO_2$0.5. In contrast, for transparent LDPE films (1×1 mm), the differences in mass loss were slightly less pronounced, with Ag-$TiO_2$3 showing a degradation efficiency nearly twice that observed using both bare TiO_2 NPs and Ag-$TiO_2$0.05. To statistically validate these findings and differences among Ag-TiO_2 catalysts with varying silver concentrations, a one-way ANOVA was conducted, revealing significant differences among the four catalysts (TiO_2, Ag-$TiO_2$0.5, Ag-$TiO_2$1, and Ag-$TiO_2$3). The most notable differences between the catalysts were observed after 240 min of UV irradiation for the degradation of black LDPE films (1×1 mm), $F(3, 8) = 475.8$, $p < 0.001$, $\eta^2 = 0.994$. Post-hoc comparison using Tukey's test confirmed that

both Ag-$TiO_2$1 and Ag-$TiO_2$3 resulted in significantly greater mass loss of LDPE films than pure TiO_2 or Ag-$TiO_2$0.5 ($p < 0.05$). In contrast, the impact of silver concentration in the catalysts was minimal for transparent LDPE films (3×3 mm). There was no significant difference found between the catalyst pairs over 960 min of UV irradiation: $AgTiO_2$0.5 vs $AgTiO_2$1 ($p = 0.900$), $AgTiO_2$0.5 vs TiO_2 ($p = 0.259$), and $AgTiO_2$1 vs TiO_2 ($p = 0.102$). The degradation efficiency of the transparent LDPE films (3×3 mm) remained very low even after 960 min of UV irradiation (1.54% ± 0.23% for TiO_2, 1.90% ± 0.19% for Ag-$TiO_2$0.5, 2.02% ± 0.20% for Ag-$TiO_2$1, and 2.94% ± 0.23% for Ag-$TiO_2$3). Comparable degradation efficiencies suggested that, within the given reaction conditions, variations in Ag content have only a marginal effect on the degradation of transparent LDPE films (3×3 mm). A more in-depth analysis of how the physical properties of LDPE affect degradation efficiency is provided in subsection *3.3.5*.

The photocatalytic degradation of LDPE films using all four catalysts (TiO_2, $AgTiO_2$0.5, $AgTiO_2$1, and $AgTiO_2$3) followed the pseudo-first-order kinetic model with a high reliability of coefficient of determination (R^2) ranging between 0.972 and 0.998 and a low SSE (from $1.62 \cdot 10^{-6}$ to $2.49 \cdot 10^{-5}$) (*Figure 27, Table 13).* The rate constant (k) increased with silver content in the catalysts, with the highest values observed in black LDPE films (1×1 mm). The observed k values were $2.64 \cdot 10^{-2}$ min^{-1} for TiO_2, $4.10 \cdot 10^{-2}$ min^{-1} for Ag-$TiO_2$0.5, $5.91 \cdot 10^{-2}$ min^{-1} for Ag-$TiO_2$1, and $1.00 \cdot 10^{-1}$ min^{-1} for Ag-$TiO_2$3. The calculated k values are consistent with prior experimental findings and the established order of photocatalytic performance for the studied catalysts. Moreover, these findings confirm that Ag doping enhances the photocatalytic activity of TiO_2 NPs, which aligns closely with the nanomaterial's characteristics. This improvement is likely attributed to enhanced charge separation and increased ROS formation. These findings are consistent with previous studies, which also reported that the degradation of various LDPE types follows a pseudo-first-order kinetic model (Ariza-Tarazona et al., 2020; Kinyua et al., 2024).

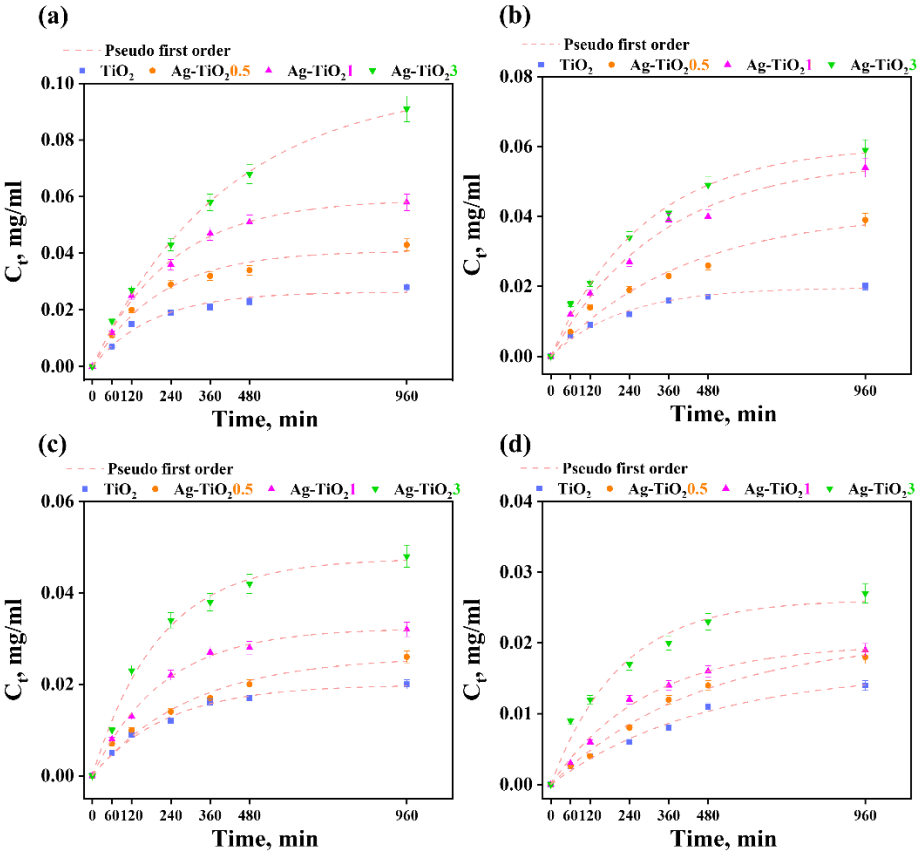

Figure 27. Analysis of kinetic parameters of the photocatalytic degradation of LDPE films with TiO_2, Ag-$TiO_2$0.5, Ag-$TiO_2$1, and Ag-$TiO_2$3 catalysts: a) black film 1×1 mm, (b) black film 3×3 mm, (c) transparent film 1×1 mm, and (d) transparent film 3×3 mm.

Ag doping on TiO_2 primarily improves its properties by enhancing photocatalytic activity. When TiO_2 is exposed to UV light, Ag particles capture and accumulate photogenerated electrons from the TiO_2 conduction band. This is likely due to the work function of Ag, which is more negative than that of TiO_2. Interfacial charge transfer between TiO_2 and Ag promotes charge separation and suppresses recombination, thereby enhancing ROS generation and improving the degradation efficiency of LDPE films. The efficiency of charge transfer between TiO_2 and Ag is strongly dependent on the size, shape, and distribution of Ag on the surface of TiO_2, as well as the surface structure of the TiO_2. In the current study, Ag NPs were approximately 19 nm in size, nearly spherical, and uniformly distributed across the TiO_2 surface. Ag-$TiO_2$1 and Ag-$TiO_2$3 contain a higher concentration of well-distributed Ag NPs than Ag-$TiO_2$0.5, which facilitates charge separation and provides more surface-active sites. Furthermore, the presence of Ag on

the TiO_2 surface broadens the light absorption range toward longer wavelengths, thereby reducing the band gap and enhancing photocatalytic activity. Along with these findings, previous studies emphasized that photocatalytic degradation of PA66 increases with Ag content from 0.5 wt% to 1.5 wt%, but only up to the optimal loading point. The Ag-TiO_2 catalyst with 1.5 wt% Ag loading demonstrated the highest degradation efficiency of 58.9% for PA66 in 4 hours under UV-A light irradiation. Meanwhile, when Ag content was further increased to 2.0 wt%, the photocatalytic degradation efficiency sharply dropped to below 15% (Wang et al., 2025). Yuwendi et al. (2022) observed a similar trend, noting that loading of 0.03 M Ag on TiO_2 achieved the highest degradation efficiency for PE at 18%, whereas increasing the Ag content to 0.06 M and 0.09 M reduced the degradation efficiency to 15%. High concentrations of Ag can lead to the formation of Ag clusters on the TiO_2 surface, thereby reducing the number of active sites available to absorb photons and potentially acting as recombination centers.

Table 13. Kinetic parameters determined from the pseudo-first-order model for the photocatalytic degradation of LDPE films.

Catalyst	k, $\mathbf{min^{-1}}$	SD, σ	$\mathbf{R^2}$	SSE
Black film, 1×1 mm				
TiO_2	$2.64 \cdot 10^{-2}$	$1.44 \cdot 10^{-3}$	0.976	$1.36 \cdot 10^{-5}$
Ag-$TiO_2$0.5	$4.10 \cdot 10^{-2}$	$2.01 \cdot 10^{-3}$	0.983	$2.28 \cdot 10^{-5}$
Ag-$TiO_2$1	$5.91 \cdot 10^{-2}$	$1.26 \cdot 10^{-3}$	0.997	$7.18 \cdot 10^{-6}$
Ag-$TiO_2$3	$1.00 \cdot 10^{-1}$	$2.78 \cdot 10^{-3}$	0.998	$1.15 \cdot 10^{-5}$
Black film, 3×3 mm				
TiO_2	$1.97 \cdot 10^{-2}$	$8.71 \cdot 10^{-4}$	0.987	$3.91 \cdot 10^{-6}$
Ag-$TiO_2$0.5	$4.17 \cdot 10^{-2}$	$4.08 \cdot 10^{-3}$	0.975	$2.49 \cdot 10^{-5}$
Ag-$TiO_2$1	$5.62 \cdot 10^{-2}$	$3.19 \cdot 10^{-3}$	0.988	$2.47 \cdot 10^{-5}$
Ag-$TiO_2$3	$6.03 \cdot 10^{-2}$	$2.37 \cdot 10^{-3}$	0.993	$1.84 \cdot 10^{-5}$
Transparent film, 1×1 mm				
TiO_2	$1.99 \cdot 10^{-2}$	$6.82 \cdot 10^{-4}$	0.993	$2.22 \cdot 10^{-6}$
Ag-$TiO_2$0.5	$2.61 \cdot 10^{-2}$	$1.86 \cdot 10^{-3}$	0.972	$1.04 \cdot 10^{-5}$
Ag-$TiO_2$1	$3.23 \cdot 10^{-2}$	$6.20 \cdot 10^{-4}$	0.998	$2.01 \cdot 10^{-6}$
Ag-$TiO_2$3	$4.75 \cdot 10^{-2}$	$1.51 \cdot 10^{-3}$	0.993	$1.30 \cdot 10^{-5}$
Transparent film, 3×3 mm				
TiO_2	$1.61 \cdot 10^{-2}$	$1.24 \cdot 10^{-3}$	0.989	$1.64 \cdot 10^{-6}$
Ag-$TiO_2$0.5	$2.08 \cdot 10^{-2}$	$1.19 \cdot 10^{-3}$	0.994	$1.62 \cdot 10^{-6}$
Ag-$TiO_2$1	$1.98 \cdot 10^{-2}$	$7.41 \cdot 10^{-4}$	0.994	$1.73 \cdot 10^{-6}$
Ag-$TiO_2$3	$2.61 \cdot 10^{-2}$	$1.41 \cdot 10^{-3}$	0.974	$1.09 \cdot 10^{-5}$

The SEM imaging analysis focused on black LDPE films (1×1 mm) to track morphological changes over time at 60 min, 480 min, and 960 min under UV-A irradiation using Ag-$TiO_2$3 (*Figure 28*). The black LDPE films (1×1 mm) were selected for SEM analysis because they exhibited the greatest mass loss during a 960 min UV exposure period in the presence of the catalyst. The appearance of surface irregularities, such as roughness, cracks, flakes, grains, holes, wrinkles, and pits, indicates successful fragmentation and oxidation of the polymer chain.

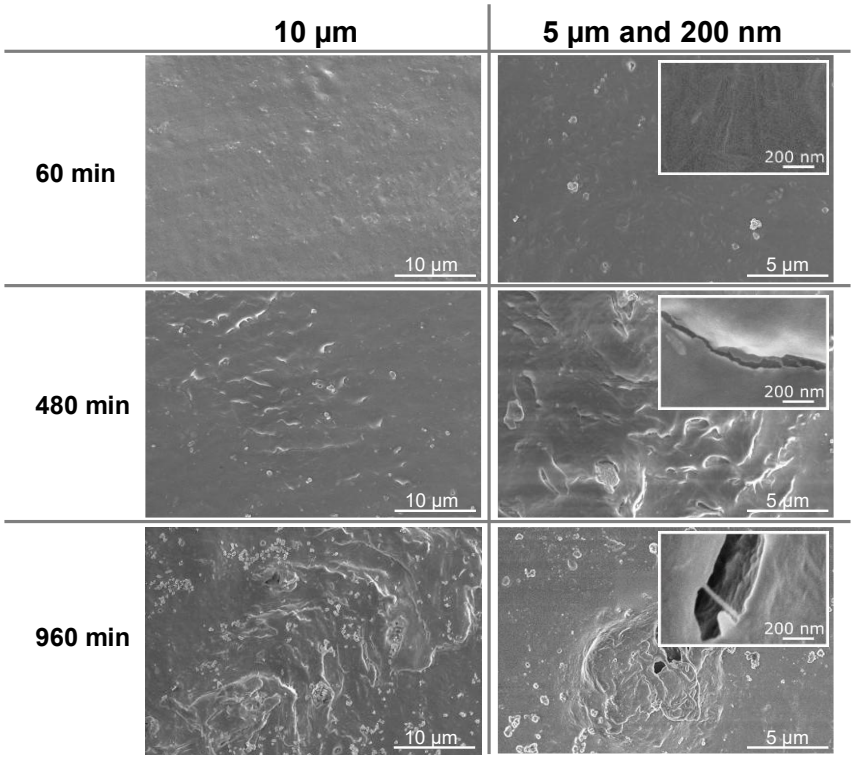

Figure 28. SEM micrographs of LDPE films (black color, 1×1 mm) at various time intervals of photocatalytic degradation using Ag-$TiO_2$3.

After an initial exposure of 60 min, the surface of the LDPE film closely resembled that of pristine black LDPE films, with only minor flake formation, indicating the beginning of surface deterioration. Notable surface changes were observed after 480 min of UV irradiation, including wrinkles, cracks, and small grooves, likely due to the formation of oxygen-containing groups and the release of volatile compounds from the LDPE matrix. After 960 min of exposure to UV light, deep cavities and pits formed on the surface of LDPE, along with more flakes and cracks. The formation of wrinkles and microcracks is particularly critical because it allows water molecules to penetrate into the

amorphous region of the polymer, facilitating further oxidation within the LDPE film (Kamalian et al., 2020).

3.3.4. Comparison of photocatalytic degradation of PE films with literature reports

The photocatalytic degradation of PE and LDPE films was analyzed in previously reported studies between 2016 and 2025. *Table 14* provides an overview of the experimental conditions, including the type of PE, photocatalyst properties, light source, irradiation time, and post-degradation analytical tools. Previous studies utilized PE films with varying sizes, ranging from 1×1 mm pieces to 11×12 cm sheets. The primary analytical techniques used to determine the degradation efficiency of PE films were mass reduction calculations, FTIR spectral analysis, and SEM imaging. Most studies have focused on metal oxide photocatalysts, aiming to improve their properties through metal doping, nanocomposite formation, and morphological engineering (Kovinchuk et al., 2023; Tofa et al., 2019). Photocatalytic tests have been primarily carried out in aqueous media, which are preferred over solid-phase reactions because they are easier to control and do not suffer from poor mass transfer and uneven light penetration (Ali et al., 2016; Kaewkam et al., 2022; Kovinchuk et al., 2023).

The literature reports variations in the photocatalytic degradation efficiencies of PE and LDPE films, influenced by the type of photocatalyst and reaction conditions. According to the reviewed studies, Ningsih et al. (2024) reported the greatest degradation efficiency for PE films. In particular, the Ru-gCN@PE film exhibited a mass loss of 74.51% after 24 h of visible-light irradiation in an aqueous medium at pH 3 and 50 °C. In contrast, no significant mass loss was observed for the pure PE films after 24 h of light irradiation, even under the optimal conditions (pH 3 at 50 °C). These results suggested that the incorporation of the catalyst (Ru-gCN) into the PE film composite enhanced photocatalytic degradation. The high activity of PE composite films was attributed to the formation of a heterojunction between Ru and g-C_3N_4, which facilitated electron transfer. In addition, at the optimal pH, the surface of the Ru-gCN@PE film attracts more protons (H^+) than pure PE films, leading to the formation of hydroperoxides and macroradicals. It is important to emphasize that PE and LDPE films require longer irradiation periods for complete degradation than most other organic pollutants. For instance, the complete mineralization of methylene blue can be accomplished in just 0.5 h, while phenolic compounds typically require around 2 h for full degradation (Alvarado et al., 2024).

Table 14. Comparison of photocatalytic degradation of PE and LDPE films**.**

Type of catalyst	Type of MPs	Irradiation time	Reaction conditions	MPs characterization	Removal efficiency	References
TiO_2 NPs	LDPE film; 3×3 cm	15 days 45 days	18 W UV lamp (λ = 315 nm) 85 W visible lamps (λ = 400–700 nm) Ambient air; solid-phase reaction	XRD, EDS, UV-VIS, weight loss, SEM, UTM, FTIR	67% 36%	(Ali et al., 2016)
ZnO nanorods	LDPE film, 1×1 cm	175 h	50 W dichroic halogen lamp (visible light), aqueous medium	SEM, OM, FTIR, DMA	CI=1.38	(Tofa et al., 2019)
Pt-ZnO nanorods	LDPE film, 1×1 cm	175 h	50 W dichroic halogen lamp (visible light), aqueous medium	SEM, OM, FTIR	CI=1.49	(Tofa et al., 2019)
N-TiO_2	LDPE film, 5×5 mm LDPE film 3×3 mm	50 h	50 W visible LED lamp (λ = 400–700 nm; room) temperature; stirring, aqueous medium (pH 3));	OM, FTIR, weight loss	0.97% 1.38%	(Llorente-García et al., 2020)
$NiAl_2O_4$	LDPE film, 3×3 cm	5 h	350 W halide lamp (visible light); aqueous medium	Weight loss, FTIR, XPS	12.50%	(Venkataramana et al., 2021)
TiO_2	LDPE film, 7×7 cm	216 h	20 W UV-A lamp (λ = 352 nm); 20 W UV-C lamp (λ = 254 nm); room temperature, solid-phase reaction	ATR-FTIR, mass loss, SEM	3.28%; 17.30%	(Kaewkam et al., 2022)
TiO_2	LDPE film coating TiO_2, 1×1 cm	288 h	250 W mercury lamp (λ = 250–420 nm) LDPE loaded with 12% Catalyst; aqueous medium (pH 4)	FTIR, GC-MS, weight loss, SEM,	6.25%	(Tejaswini and Pathak, 2023)

Type of catalyst	Type of MPs	Irradiation time	Reaction conditions	MPs characterization	Removal efficiency	References
TiO_2 TiO_2/MnO_2	PE film, thickeness of 50-70 μm	90 h	6 W UV lamp (λ = 280 nm); ambient air; solid-phase reaction	TGA, DMA, FTIR, weight loss, SEM	14.6% 21.2%	(Kovinchuk et al., 2023)
Ru-g-C_3N_4	PE film, 1×1 cm Ru-gCN@PE film, 1×1 cm	24 h	500 W Mercury-Xenon Lamp (λ > 350 nm), aqueous medium (pH 1–6) at 0, 35, 50, and 70 °C	ATR-FTIR, weight loss, SEM	No weight loss 74%	(Ningsih et al., 2024)
TiO_2	LDPE film, 4×4 cm	800 h	UV lamp (λ = 254 nm); with and without NaOH pre-treatment; room temperature; solid-phase reaction	ATR-FTIR, weight loss, XPS, SEM, tensile test, TGA, DSC	87% 55%	(Lu et al., 2025)
Ag-TiO_2	LDPE film, black, 3×3 mm LDPE film, black, 1×1 mm LDPE film transparent, 3×3 mm LDPE film transparent, 1×1 mm	16 h	36 W UV lamp (λ > 365 nm); aqueous medium (pH = 7)	ATR-FTIR, weight loss, SEM	6.19% 9.88% 2.94% 4.85%	This study

Figure 29 shows the degradation efficiency of LDPE films plotted against time, despite differences in the photocatalytic test conditions. It can be observed that PE and LDPE films achieve mass losses exceeding 50% only following extended light irradiation. For example, Lu et al. (2025) found an 87% mass loss of LDPE films after 800 h of photocatalytic degradation. Similarly, Ali et al. (2016) reported a 67% mass loss in LDPE films after 15 days of UV exposure. While degradation efficiencies of PE and LDPE films generally increased linearly over time, some findings deviated notably from this pattern. Deviation from typical degradation trends was observed, with an exceptionally high mass loss of 74.51% within 24 h of light irradiation, as

reported by Ningsih et al. (2024). The observed variations might be associated with the incorporation of the catalyst into the plastic matrix and with optimized reaction conditions that promote more efficient degradation. The mass loss of LDPE films used in this study varied from 2.94% to 9.88% over 16 h of UV-A irradiation. Compared with earlier studies, this work demonstrated high efficiency in the photocatalytic degradation of LDPE films after 16 h of UV-A exposure, even when compared with reports that use longer irradiation times (Kaewkam et al., 2022; Tejaswini and Pathak, 2023).

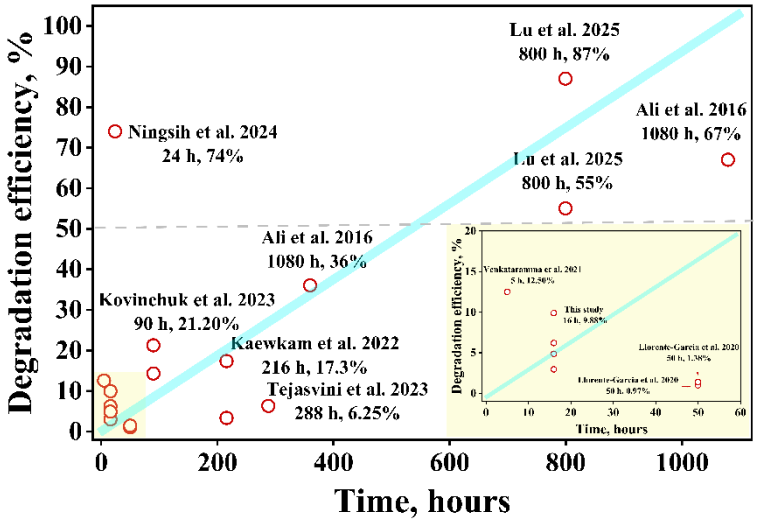

Figure 29. Photocatalytic degradation efficiency of PE and LDPE films as a function of irradiation time.

3.3.5. Influence of LDPE film physical properties on photocatalytic degradation

The photocatalytic degradation of the studied LDPE films using TiO_2 and Ag-TiO_2 is presented in *Figure 30.* As expected, bare TiO_2 NPs show limited variations in mass loss between black and transparent LDPE films due to catalytic constraints. Meanwhile, in the presence of Ag-$TiO_2$3, more pronounced differences in mass loss were observed between black and transparent LDPE films. After 480 min and 960 min of UV-A irradiation with Ag-$TiO_2$3, black LDPE films exhibited 1.5 to 2 times greater mass loss than transparent LDPE films under the same reaction conditions. Statistical analysis further confirmed significant differences in degradation efficiency among the studied LDPE films based on their physical properties ($F(3;8) = 535.115$, $p < 0.001$, $\eta^2 = 0.995$). Furthermore, the Post-Hoc test

showed that black LDPE films with dimensions of 1×1 mm exhibited significantly higher mass loss than other LDPE films.

When comparing black and transparent LDPE films, particular attention should be given to the additives present in each material. XRF analysis revealed that while transparent LDPE films are primarily pure, black LDPE films contain relatively high concentrations of inorganic materials, specifically Ca and Ti. Additives in LDPE films can influence the stability and reactivity of the polymer. For example, additives such as anti-blocking agents increase the surface roughness of black films, which enhances catalyst interaction. Meanwhile, the presence of TiO_2 in black LDPE films modulates UV resistance: a low TiO_2 abundance (5–10%) within LDPE films prevents UV damage, whereas TiO_2 levels above 15% alter polymer crystallinity and can enhance oxidation (Ndibewu et al., 2024). The present study indicated that increased additive content can impact the efficiency of photocatalytic degradation of LDPE films. The effect of additives mainly depends on their concentrations and reaction conditions, which determine whether they reinforce the polymer or initiate new reactions within the polymer chain.

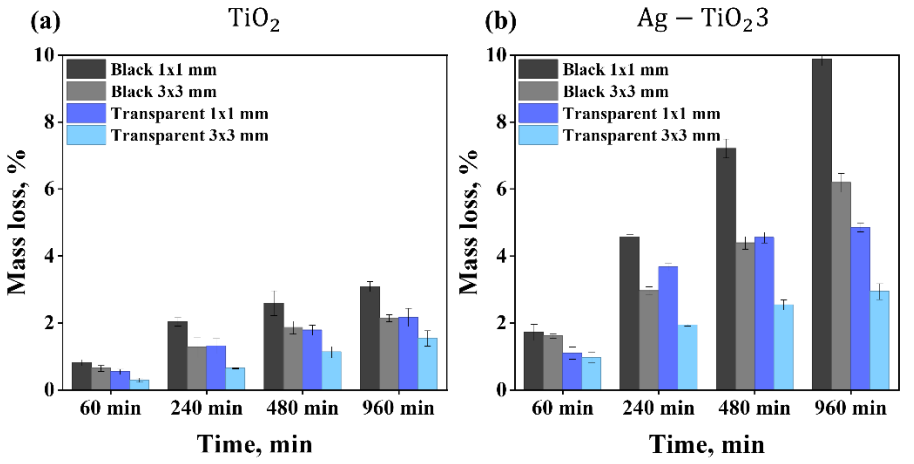

Figure 30. A comparative analysis of the photocatalytic degradation of LDPE with different physical properties using catalysts (a) TiO_2, and (b) Ag-$TiO_2$3.

The higher degradation observed in black LDPE films is also attributed to their heat absorption capacity. The increased radiation absorption in black films raises the surface temperature, ultimately promoting photochemical processes (Reinicker, 2018). However, these results contrast with a few earlier studies. Yang et al. (2022) observed that white PE mulch films released more microplastic particles (163 particles/cm^2) than black PE films (147 particles/cm^2) after 70 days of UV exposure. Similarly, Key et al. (2024) found that

black HDPE lids exhibited the lowest degradation efficiency and showed no significant increase in their CI compared with white, silver, red, blue, and green lids. This suggests that pigments, colorants, or stabilizing agents play a crucial role in the interaction of plastics with UV and visible light, as well as in polymer durability. However, inconsistencies across studies indicate that microplastic degradation is not determined by color alone but is also heavily influenced by other factors, including the polymerization process, additives, and environmental or storage conditions.

A comparison of mass reduction in LDPE films of different sizes (1×1 mm and 3×3 mm) indicated that smaller films degrade faster than larger ones. The mass loss of LDPE films of size 1×1 mm was 1.5 times greater than that of 3×3 mm films within 480 min and 960 min of UV exposure. The increased degradation efficiency in smaller LDPE films is attributed to a higher surface area-to-volume ratio, which enhances interactions with the photocatalyst and ROS and promotes greater light absorption. Moreover, smaller LDPE films were found to distribute more evenly in the reaction solution. In contrast, larger LDPE films tended to overlap and block one another, thereby reducing light penetration and the number of available active sites on their surfaces. These findings are consistent with the work of Llorente-García et al. (2020), which reported that smaller HDPE microbeads (382 ± 154 μm) experienced a mass loss that was 21 times higher than that of larger particles (814 ± 91 μm) over a 50 h irradiation period in the presence of TiO_2-based catalysts. Despite the higher degradation efficiency observed in smaller microplastics, it is crucial to note that they pose a greater environmental risk. This is due to their ability to release more additives and absorb more contaminants into the surrounding ecosystems.

The SEM was used to study LDPE films with different physical properties that underwent 960 min of UV irradiation using catalysts TiO_2 and Ag-$TiO_2$3 (*Figure 31)*. While the application of TiO_2 resulted in only slight alterations to surface morphology, the incorporation of Ag led to extensive surface damage and structural modifications. The SEM analysis of black LDPE films (1×1 mm) showed that they exhibited the most pronounced surface changes among the samples. After 960 min of UV irradiation with Ag-$TiO_2$3, cracks, cavities, and deep pits were observed on the surface of the black LDPE films. In addition, cavities and pits in the black LDPE films extended toward the internal layers and expanded along the surface. This suggests a notable decomposition of the LDPE matrix, most likely resulting from the volatilization of organic species and cleavage of the polymer main chain (Ali et al., 2016; Sura and Nain, 2024).

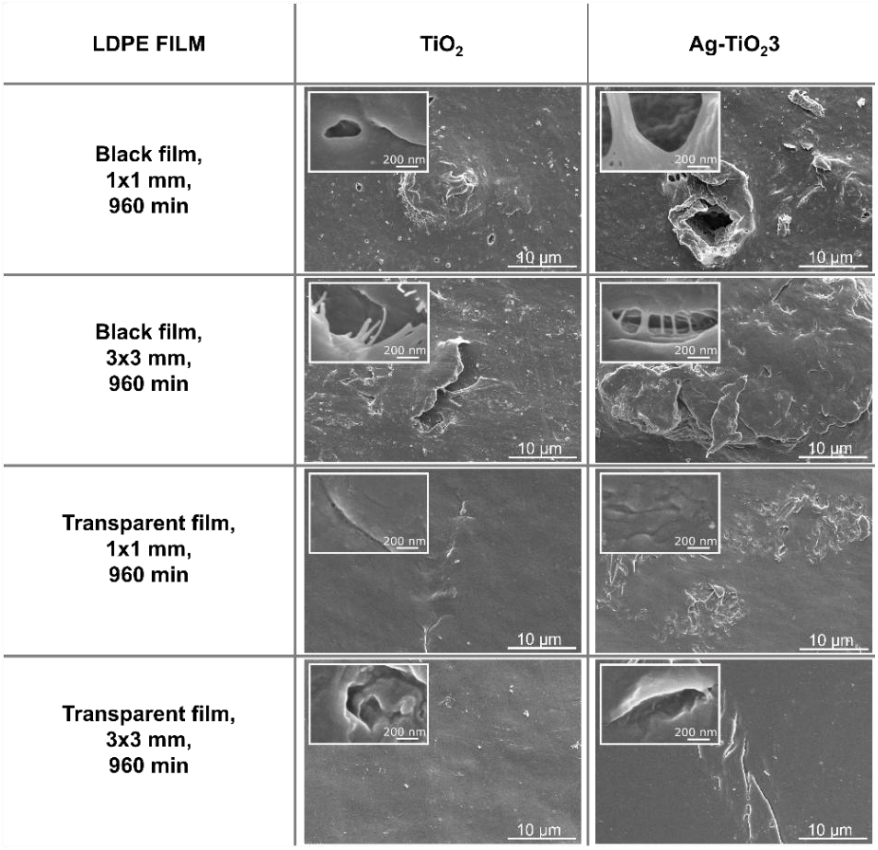

Figure 31. SEM micrographs of LDPE films after 960 min of UV-A irradiation with TiO_2 and Ag-TiO_2.

In contrast to the black LDPE films, the transparent LDPE films (1×1 mm) showed less surface damage after 960 min of UV-A irradiation in the presence of a catalyst. In transparent LDPE films, the surface mainly remained smooth and homogeneous. Physical alterations such as wrinkles, cracks, and small cavities were observed, but these appeared only in limited areas rather than across the entire surface. In addition, unlike the black LDPE films, the transparent LDPE films showed no substantial internal damage, indicating that degradation in the transparent LDPE films was only to the top layers. In pristine black LDPE films, the surfaces were characterized by roughness and minor fractures, which increase surface area, enhance light absorption, and promote interactions with catalysts. Defect-containing regions, such as wrinkles and cracks, play a critical role in degradation by serving as initiation sites for oxidation reactions. As a result, the surface characteristics of pristine black LDPE films are more favorable for photocatalytic degradation. The differences between the smaller (1×1 mm)

and larger (3×3 mm) LDPE films were also evaluated. As expected, the smaller LDPE films exhibited greater surface damage, consistent with the mass loss results *(Figure 30)*. This is attributed to their ability to achieve a more uniform distribution in the reaction solution, which allows for better interaction with the catalyst and with UV light. Meanwhile, alterations in larger LDPE films were less pronounced and more localized than in the smaller films. All studied samples exhibited wrinkles, flakes, cavities, and pits resulting from photocatalytic degradation. It is important to note that these morphological characteristics were typically observed in plastics sourced from agricultural areas (Zhang et al., 2021).

3.3.6. Evaluation of chemical transformation in LDPE films using FTIR

The photocatalytic degradation of LDPE films was further followed by ATR-FTIR analysis. The FTIR spectra were recorded after 60 min and 960 min of UV exposure using Ag-$TiO_2$3. In black LDPE films, several new characteristic peaks were identified, indicating the formation of oxygen-containing groups. Particularly, peaks at ~1740 cm^{-1} and ~1654 cm^{-1} suggested the appearance of carbonyl groups (C=O) (*Figure 32 (a, b)*). The carbonyl band typically appears in the 1650 cm^{-1} to 1850 cm^{-1} spectral region. This broader region reflects a variety of oxidation products, including esters, ketones, aldehydes, and carboxylic acids. The characteristic peak at 1740 cm^{-1} is attributed to the C=O stretching vibration of ester groups. This finding is highly consistent with reports in the literature, which typically assign ester bands to the 1735–1750 cm^{-1} (Aniśko-Michalak et al., 2025). Specifically, studies on the weathering and photodegradation of LDPE have identified characteristic ester bands at very similar wavenumbers, including 1735 cm^{-1}, 1739 cm^{-1}, and 1748 cm^{-1} (Gardette et al., 2013; Moharir and Kumar, 2021). Ester groups mainly form through the reaction of a peracid with a ketone or the combination of two hydroperoxide species. A second new peak at 1654 cm^{-1} corresponds to α,β-unsaturated ketones and aldehydes. Prior studies indicated that absorption bands in the 1650 cm^{-1} to 1690 cm^{-1} region are specific to unsaturated carbonyl compounds (Aniśko-Michalak et al., 2025; Moharir and Kumar, 2021). Another important indicator of degradation is the peroxide (C–O) stretching vibration, observed as a broad absorption band at 980–1158 cm^{-1}. Peroxide bands typically lie within the broader spectral range of 1000 cm^{-1} to 1350 cm^{-1} (Sura and Nain, 2024). For example, in previous research on the weathering and degradation of both LDPE and HDPE, peaks at 1068 cm^{-1}, 1032 cm^{-1}, and 1010 cm^{-1} were assigned to primary alcohols or to O–H deformation in alcohols, peroxides, or hydroperoxide (Gong et al.,

2023). The absorption band observed between 3220 cm^{-1} and 3620 cm^{-1} indicates the formation of hydroperoxide (–OOH) product and alcohols (–OH) (Lu et al., 2025).

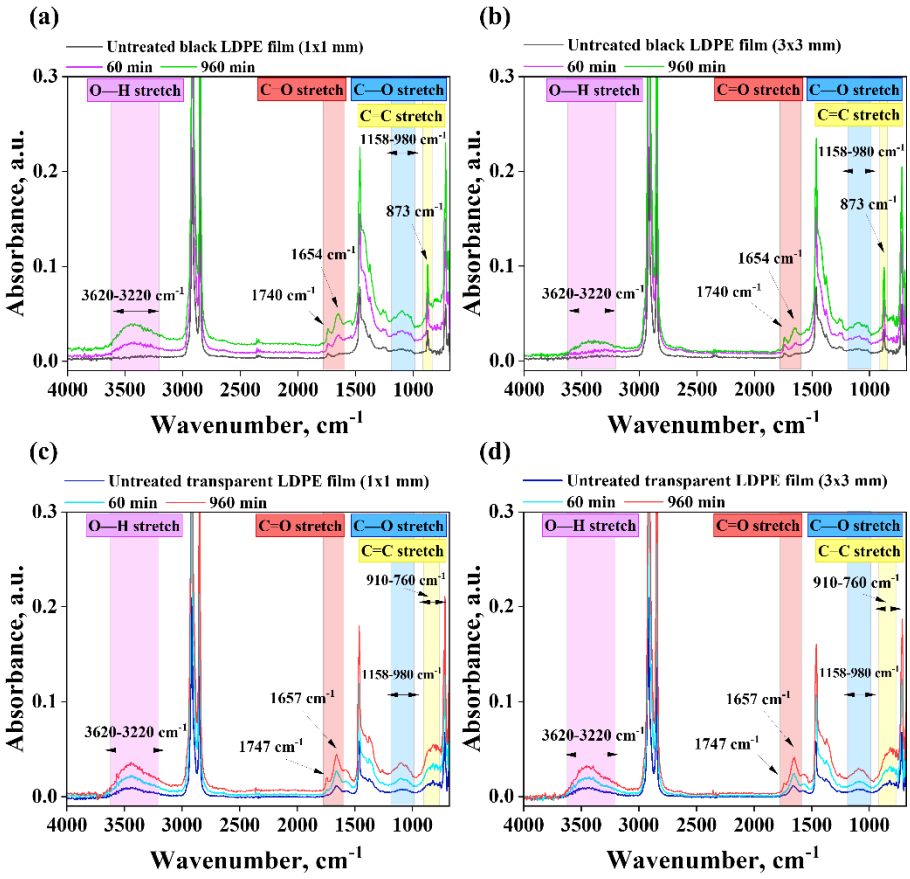

Figure 32. FTIR spectra of pristine (untreated) LDPE films and LDPE films degraded with Ag-$TiO_2$3 under UV irradiation for 60 min and 960 min: (a) black film 1 ×1 mm; (b) black film 3 ×3 mm, (c) transparent film 1 ×1 mm, and (d) transparent film 3 ×3 mm.

In pristine black LDPE films, unsaturated vinyl (–C=C–) groups were observed at 873 cm^{-1} and increased with UV irradiation time over 960 min. Previous studies also indicated an increase in unsaturated vinyl-family groups (vinylidene, terminal vinyl, and trans-vinylene) in the 888–990 cm^{-1} region as a result of the oxidation process (Gardette et al., 2013; Ghanadi and Padhye, 2024). Similar results were reported by Doğan (2021), who found a vinyl group at 874 cm^{-1}. The increasing intensity of the vinyl peak indicates the destabilization of the polymer chain and contributes to photo-oxidation reactions. The formation of these unsaturated species most likely arises from

olefin formation caused by cleavage of C–H bonds within the polymer. The broadening of the peaks at 718 cm^{-1} (CH_2 rocking) and 1462 cm^{-1} (CH_2 bending) indicates structural changes, including deformation of methyl groups, polymer chain cleavage, and disruption of crystallinity (Suresh et al., 2011).

Transparent LDPE films followed degradation patterns similar to black LDPE films, although it is important to note that they exhibited a lower carbonyl formation rate. For instance, the peak at 1747 cm^{-1} (C=O) was absent during the initial irradiation and appeared only after 960 min of UV exposure (*Figure 32 (c, d)*). The peak observed at 1657 cm^{-1} corresponds to the C=O bond, while absorption bands between 770–892 cm^{-1} are associated with the –C=C– bond. Bands in the range of 3220–3620 cm^{-1} indicate –OOH and –OH groups, and those between 1158–980 cm^{-1} are related to the C–O bond. These functional groups were already present in pristine, transparent LDPE films and increased with longer UV irradiation times. The increased intensity of absorption bands corresponding to oxygen-containing functional groups and unsaturated bonds suggested successful oxidation of the LDPE polymer chain. Furthermore, film size influenced the extent of degradation, with smaller (1×1 mm) LDPE films characterized by sharper and more intense C=O peaks than 3×3 mm films, suggesting enhanced photooxidation.

The extent of LDPE film degradation is evaluated through the CI and VI, both of which typically increase during photodegradation (*Table 15*). CI measures carbonyl groups, which are initial indicators of polymer oxidation processes. In contrast, VI tracks the formation of vinyl groups, which represent unsaturated sites arising mainly from bond-breaking at the tertiary carbons of the polymer branches. The formation of vinyl bonds in the polymer chain is typically attributed to the Norrish type II reaction (Sorasan et al., 2022).

The results in *Table 15* revealed that all LDPE films exhibited increases in CI and VI as UV exposure time rose from 60 min to 960 min. Notably, black LDPE films showed higher values than transparent films, with black LDPE films (1×1 mm) reaching the highest values of CI (0.93 ± 0.09) and VI (0.49 ± 0.04). Similarly, among transparent LDPE films, the smaller ones (1×1 mm) had higher CI (0.68 ± 0.04) and VI (0.34 ± 0.03) indices compared to larger films (3×3 mm). The obtained results suggested that even minor differences in the physical and chemical characteristics of LDPE can influence its photooxidation behavior.

Table 15. Measured carbonyl and vinyl indices for LDPE films after photocatalytic degradation with Ag-$TiO_2$3.

Sample	Exposure time, min	CI	VI
Untreated LDPE films (Control)			
Black LDPE	-	0.10 ± 0.02	0.23 ± 0.02
Transparent LDPE	-	0.31 ± 0.06	0.19 ± 0.02
After degradation			
Black LDPE, 1×1 mm	60	0.71 ± 0.05	0.38 ± 0.03
	960	0.93 ± 0.09	0.49 ± 0.04
Black LDPE, 3×3 mm	60	0.51 ± 0.04	0.33 ± 0.06
	960	0.64 ± 0.06	0.36 ± 0.03
Transparent LDPE, 1×1 mm	60	0.53 ± 0.09	0.26 ± 0.06
	960	0.68 ± 0.04	0.34 ± 0.03
Transparent LDPE, 3×3 mm	60	0.43 ± 0.05	0.25 ± 0.02
	960	0.50 ± 0.07	0.33 ± 0.03

3.3.7. Chapter conclusion

Doping TiO_2 with Ag significantly enhances the photocatalytic degradation of LDPE mulch films. The Ag loading on TiO_2 reduced the band gap energy from 3.2 eV for bare TiO_2 to 2.76 eV for Ag-$TiO_2$3. The maximum mass loss of the studied LDPE films was achieved with Ag-$TiO_2$3 under 960 min of UV-A irradiation. The mass loss of black LDPE (1×1 mm) was 9.88%, while transparent LDPE films of the same size reached only 4.85%. FTIR analysis further confirmed the successful oxidation of LDPE mulch films, with the black LDPE films (1×1 mm) showing the highest CI and VI values of 0.93 and 0.49, respectively.

The results revealed that physical properties, specifically size and color, are important factors in determining the degradation process. Smaller 1×1 mm LDPE films exhibited mass losses 1.5 times greater than those of 3×3 mm films due to a higher surface-to-volume ratio and better distribution in aqueous solution. SEM imaging confirmed that black films exhibited extensive structural damage, including the formation of deep pits and cavities, whereas transparent LDPE films showed only minor surface fractures. These findings indicate that the studies of “real-to-world” microplastics are essential for bridging the gap between fundamental laboratory research and practical applications.

3.4. Mechanisms of photocatalytic degradation of LDPE microplastics

3.4.1. Proposed mechanisms of LDPE degradation using TiO_2-clay nanocomposites

Previous studies have focused on understanding the processes and mechanisms involved in the photocatalytic degradation of LDPE (Ariza-Tarazona et al., 2020; Llorente-García et al., 2020; Tofa et al., 2019). Based on experimental and literature data, the photocatalytic degradation pathways of LDPE using TiO_2, TiO_2-Kao, and TiO_2-MMT were proposed and compared. In the present study, TiO_2 acts as the primary catalyst for the photocatalytic degradation of LDPE microplastics. When TiO_2 is irradiated by photons with energy greater than its band gap energy, electrons (e^-) are excited and move from the VB to the CB, creating e^-/h^+ pairs. These charge carriers migrate to the surface of the TiO_2 catalyst, where photogenerated h^+ oxidize water or hydroxyl ions (OH^-) to produce $\cdot OH$, while e^- reduces molecular oxygen (O_2) to form $\dot{O}_2^-$. UV-excited TiO_2 can produce two types of $\cdot OH$ radicals, free $\cdot OH_f$ and surface-bound $\cdot OH_s$. When $\cdot OH_f$ radicals form, they are well dispersed throughout the reaction solution, while $\cdot OH_s$ radicals react only with absorbed pollutants (Kim et al., 2014). In addition, the photogenerated h^+ can react directly with surface-bound polymers, forming organic free radicals that further contribute to degradation. In general, ROS act as primary oxidants that initiate and control the photocatalytic degradation of LDPE, typically following the Langmuir-Hinshelwood kinetic model (Turchi and Ollis, 1990). The detailed explanation of the LDPE degradation mechanism is discussed in Chapter *3.4.3*.

In the present study, clay minerals, such as kaolinite and montmorillonite, enhanced the degradation efficiency of LDPE microplastics. These minerals not only provide physical support to TiO_2 NPs, but they also have a combined effect through interaction with TiO_2 NPs. Clay minerals have three primary mechanisms for enhancing the photocatalytic degradation of LDPE. First, the layered structure of clay minerals helps spatially separate the e^- and h^+ generated by TiO_2 NPs upon light absorption. This separation prevents their recombination (Li et al., 2022). Second, h^+ photogenerated by TiO_2 NPs react with hydroxyl groups or oxygen molecules present on the surface of clay minerals. This interaction between photogenerated h^+ and surface functional groups of clay minerals promotes the formation of superoxide and hydroxyl radicals (Cao et al., 2021). Finally, both minerals can generate hydroxyl radicals in aqueous media under light irradiation, thereby increasing the concentration of $\cdot OH$ radicals and further enhancing overall

degradation efficiency (Ding et al., 2022). A schematic representation of the mechanisms of ROS generation using TiO_2 NPs and TiO_2-clay nanocomposites is shown in *Figure 33*.

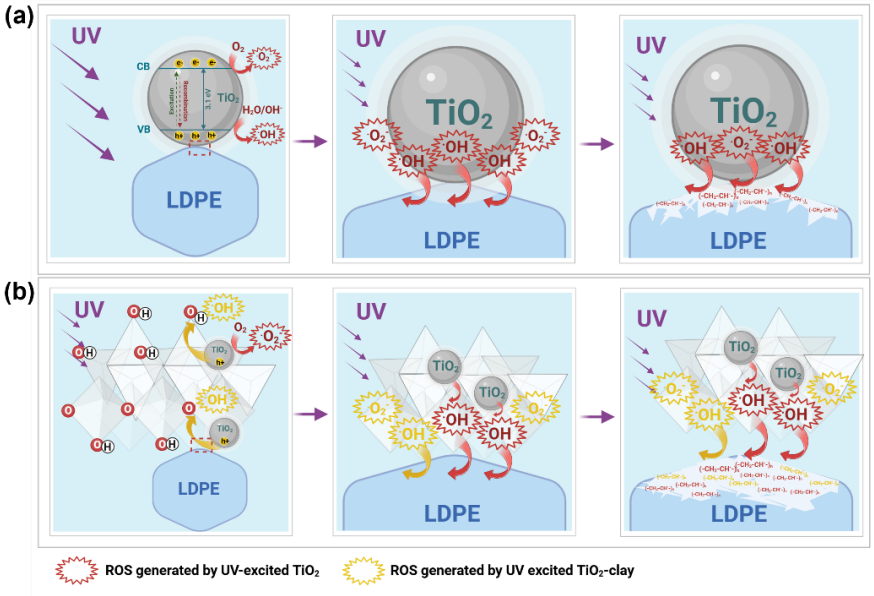

Figure 33. A schematic representation of ROS generation pathways in photoexcited (a) TiO_2 and (b) TiO_2-clay nanocomposites.

3.4.2. ROS generation and role in LDPE film degradation using Ag-TiO_2

Quenching experiments were performed to identify the primary ROS involved in the photocatalytic degradation of LDPE films, using scavengers (IPA, AA, AO) in combination with TiO_2 or Ag-TiO_2 under UV-A light for 240 min. When TiO_2 was used as a catalyst, only slight changes were observed in the mass loss of LDPE films, as shown in *Figure 34*. This can be attributed to minimal mass loss of LDPE when bare TiO_2 NPs were used and to a high e^-/h^+ recombination rate, which inhibits the generation of ROS necessary for the degradation process (Petronella et al., 2019). In the reaction system, a greater decrease in LDPE mass loss was observed when Ag-$TiO_2$3 served as the catalyst. IPA acts as a scavenger for $\cdot OH$ radicals. Its addition in the presence of Ag-$TiO_2$3 notably reduced degradation efficiency, decreasing mass loss from 4.57% to 1.76% for black LDPE films (1×1 mm) and from 3.67% to 1.68% for transparent LDPE films (1×1 mm). The IPA effect was much more notable than the changes observed with other scavengers (AA and AO). These results suggested that $\cdot OH$ radicals play a dominant role in the photodegradation of LDPE films in the Ag-TiO_2 reaction system. In addition

to AA, which specifically targets $O_2^{\cdot-}$ radicals, the mass loss was reduced from 4.57% to 3.09% for black films (1×1 mm) and from 3.68% to 2.62% for transparent films (1×1 mm). Although $O_2^{\cdot-}$ radicals contribute to LDPE degradation, their impact is less pronounced than that of $\cdot OH$ radicals. On the contrary, when AO was used to scavenge photogenerated h^+, only minor changes were observed in LDPE mass reduction, indicating that h^+ has only a limited role in the current reaction system compared to ROS.

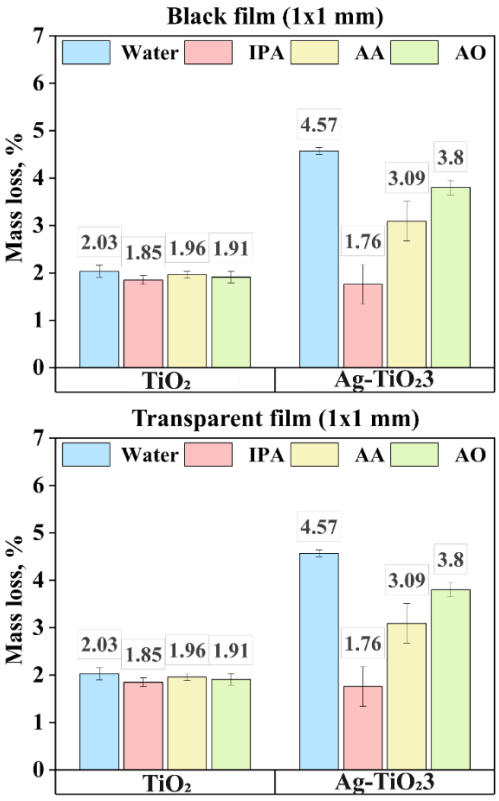

Figure 34. ROS quenching tests during the photocatalytic degradation of LDPE films using TiO_2 and Ag-$TiO_2$3 over 240 minutes. Images represent (a) black film (1×1 mm) and (b) transparent film (1×1 mm).

The results confirmed that $\cdot OH$ radicals are the primary ROS responsible for the photocatalytic degradation of LDPE films in the Ag-TiO_2 driven reaction system, following the order from highest to lowest contribution: $\cdot OH > O_2^{\cdot-} > h^+$. $\cdot OH$ radicals were found to be the most significant species to initiate and control photocatalytic degradation reactions of LDPE, most likely due to its high redox potential (+2.8 V) (Zhu et al., 2020). This aligns with the observed effects of $\cdot OH$ on degrading various organic pollutants, such as pharmaceuticals, dyes, and phenols, in earlier

studies of TiO_2-based photocatalytic degradation systems (Chen et al., 2020). The involvement of $O_2^{\cdot-}$ was more notable when Ag-TiO_2 was used instead of pure TiO_2. This is because Ag ions capture photogenerated electrons from TiO_2, facilitating the reduction of molecular oxygen into superoxide ions. Scavenging photogenerated h^+ resulted in the slightest decrease in mass loss. Although previous studies indicated the importance of h^+ as they can directly oxidize the polymer chain or react with hydroxide ions or water to form $\cdot OH$, the overall $^{h+}$ contribution depends on reaction conditions (Lu et al., 2025). These findings are consistent with studies on other microplastics like PE, PS, PP, and PVC, confirming that $\cdot OH$ and $O_2^{\cdot-}$ species are the dominant contributors to oxidation across different polymer chains (Ding et al., 2022; Ningsih et al., 2024). It should be noted that a few earlier studies have also highlighted the potential involvement of singlet oxygen ($^1O_2$), particularly in PS, suggesting that multiple oxidative pathways may contribute (Zheng et al., 2024).

3.4.3. Proposed mechanisms of LDPE degradation using Ag-TiO_2 nanomaterials

The photocatalytic degradation of LDPE by TiO_2 and Ag-TiO_2 nanomaterials is primarily driven by the generation of ROS. These ROS interact with a variety of chemical bonds, including C-H, C-N, C-C, C-O, and N-H, and their reactivity is determined by bond dissociation energy and the surrounding chemical environment. As discussed in subsection *3.4.1*, photoexcited TiO_2 generates e^-/h^+ pairs, which further initiate ROS generation in the reaction system. The incorporation of Ag onto the surface of TiO_2 enhances this process by mitigating charge-carrier recombination. As silver is a noble metal with a lower Fermi level than TiO_2, electrons spontaneously migrate from the TiO_2 to Ag until thermodynamic equilibrium is reached. This transition results in the formation of a Schottky barrier at the Ag-TiO_2, which contributes to capturing and accumulating electrons on the silver surface. By acting as an electron trap, the Ag NPs reduce the recombination rate of e^-/h^+ pairs and extend the lifetime of photogenerated electrons (Yuwendi et al., 2022). This improved charge separation in Ag-TiO_2 ultimately increases the yield of $O_2^{\cdot-}$ radicals, thereby facilitating the overall efficiency of the photocatalytic degradation (Kohtani et al., 2008). The mechanisms of ROS generation in TiO_2 and Ag-TiO_2 photocatalysts are illustrated in *Figure 35*.

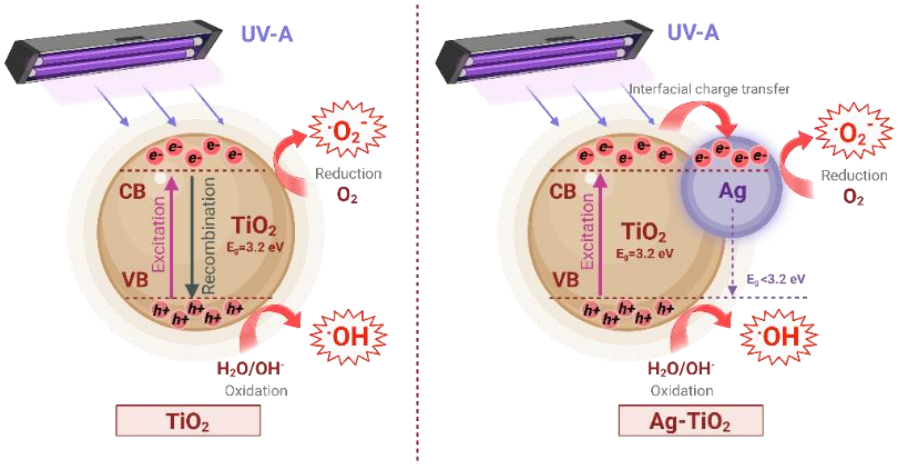

Figure 35. A schematic representation of ROS generation pathways in photoexcited TiO_2 and Ag-TiO_2.

Once ROS are generated in the reaction system, the $\cdot OH$ radicals act as initiators of LDPE degradation by oxidizing its C–C bonds, leading to the formation of alkyl radicals (-•CH-CH_2-). Then, alkyl radicals react with O_2, generating a peroxy radical (-CH_2-HCOO•-CH_2-) that propagates the reaction by abstracting hydrogen from other chains (RH), leading to the formation of hydroperoxides (-CH_2-HCOOH-CH_2-). The weak O–O bond in hydroperoxides renders them susceptible to UV-induced decomposition, leading to the formation of alkoxy (-CH_2-HCO•-CH_2-) and $\cdot OH$ radicals. Due to their high reactivity, alkoxy radicals participate in further oxidation reactions with O_2, contributing to β-scission (Gardette et al., 2013; Lu et al., 2025). As a result, polymers containing carbonyl functional groups are formed. Upon further exposure to UV light, carbonyl-containing groups become susceptible to Norrish type I and II reactions. Norrish type I involves α-cleavage, leading to chain scission and degradation into CO, resulting in mass reduction, whereas Norrish type II occurs via abstraction of hydrogen from the γ carbon, producing additional carbonyl and vinyl groups (Ningsih et al., 2024). The overview of proposed photocatalytic degradation pathways of LDPE is illustrated in *Figure 36*.

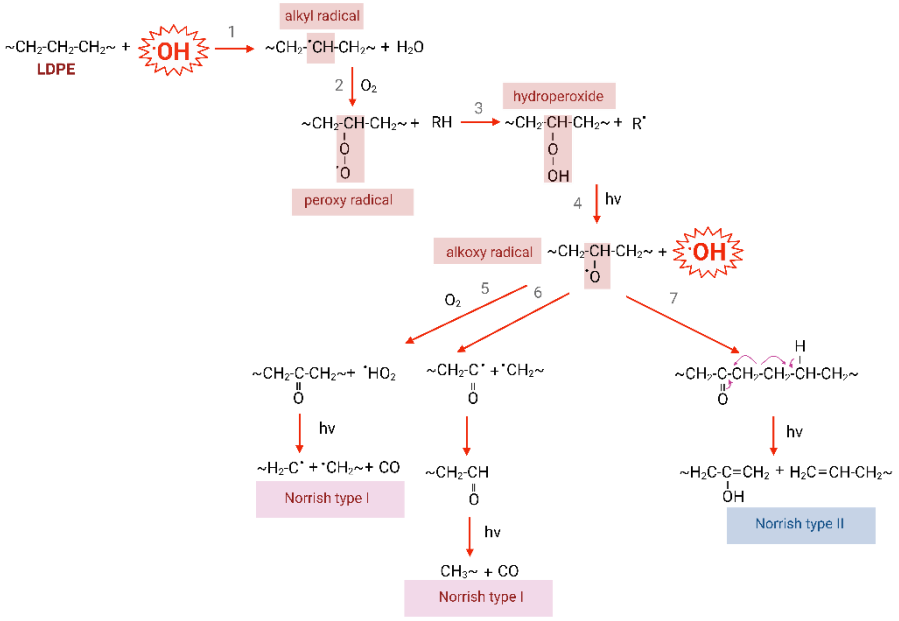

Figure 36. Proposed photocatalytic degradation pathways of LDPE microplastics.

3.4.4. Mechanisms of mass loss in LDPE during photocatalytic degradation

The mass loss of LDPE microplastics during photocatalytic degradation is not solely due to complete breakdown into CO_2 and H_2O. Rather, it results from a combination of oxidation-induced processes, including polymer chain scission, surface oxidation, and the formation of volatile and soluble organic compounds. In the initial step, chain scission occurs, first reducing the polymer's molecular weight without reducing its mass. Afterward, macroradicals formed during this process react with peroxy and hydroxyl radicals, introducing oxygen into the polymer chain. This leads to the formation of oxygen-containing groups, particularly ketones, aldehydes, and carboxylic acids (Yagoubi et al., 2015). When the oxidation products are reduced to sufficiently low molecular weights, they tend to become volatile or soluble. Volatile degradation products may move from the bulk of the LDPE to its surface and later be released into the surrounding medium. The loss of these volatile by-products from the LDPE matrix results in a decrease in sample mass, which can be determined by weight measurements. The primary volatile by-products resulting from the photocatalytic degradation of PE (LDPE and HDPE) include small hydrocarbons such as methane and ethane, oxygenated organic compounds such as formaldehyde, acetone, and

carboxylic acids, specifically formic and acetic acids (Ghanadi and Padhye, 2024).

In the meantime, common soluble products consist of oxidized oligomers, short-chain fatty acids, aldehydes, and ketones (Stancu et al., 2025). These compounds primarily form near the surface of the microplastics and dissolve into the surrounding medium, thereby contributing to measurable mass loss and partial mineralization of the solid polymer. Furthermore, in previous studies, LDPE by-products were tested using GC-MS and found to be non-toxic, suggesting that this process does not result in secondary pollution (Chen et al., 2022).

CONCLUSIONS

1. The modified TiO_2 NPs exhibited better photocatalytic performance for LDPE microplastics than pure TiO_2 NPs. At neutral pH and 480 min of UV-A irradiation, the highest mass loss of LDPE was observed with TiO_2-Kao (28.36%). With Ag-TiO_2 nanomaterials after 960 min of UV-A irradiation, the mass loss of black LDPE films (1×1 mm) increased from 3.08% (pure TiO_2 NPs) to 9.88% (Ag-$TiO_2$3).

2. Under acidic conditions (pH 3), the maximum mass loss of LDPE was 30.96% with TiO_2-Kao after 60 min of UV-A irradiation. Adjusting the LDPE-to-catalyst ratio to 1:2 improved mass loss by 10%, resulting in 25.98% for TiO_2-Kao over 60 min. Increasing the ionic strength to 0.5 $molL^{-1}$ reduced LDPE mass loss from 17.08% to 7.82%, depending on the catalyst type.

3. Using Ag-$TiO_2$3, black LDPE films (1×1 mm) exhibited twice the mass loss of transparent LDPE films (1×1 mm) over 960 min of UV irradiation, with 9.88% vs. 4.85%, respectively. LDPE film size also influenced degradation efficiency. Reducing the size from 3×3 mm to 1×1 mm increased mass loss from 6.19% to 9.88% for black LDPE films and from 2.94% to 4.85% for transparent LDPE films.

4. After the photocatalytic degradation, LDPE microplastics showed the formation of new oxygen-containing functional groups, including ester (1740 cm^{-1}), aldehydes (2634 cm^{-1} and 1654 cm^{-1}), ketones (1700–1850 cm^{-1}), and unsaturated vinyl groups (873 cm^{-1}). The CI reached a maximum of 1.41 with TiO_2-Kao in LDPE fragments and 0.93 with Ag-$TiO_2$3 in black LDPE films (1×1 mm). The highest VI 0.49 was observed in black LDPE films (1×1 mm), indicating extensive polymer chain scission.

5. Hydroxyl radicals (·*OH*) were identified as the dominant ROS initiating LDPE degradation, with their scavenging reducing mass loss from 4.57% to 1.76% in black LDPE films (1×1 mm) and from 3.68% to 1.68% in transparent LDPE films. Superoxide radicals ($O_2^{\cdot-}$) acted as secondary contributors, reducing mass loss from 4.57% to 3.09% in black LDPE films (1×1 mm) and from 3.68% to 2.62% in transparent LDPE films (1×1 mm), with their role notably enhanced in the presence of Ag-loaded catalyst.

SANTRAUKA

ĮVADAS

Plastikas yra viena iš plačiausiai naudojamų medžiagų šiuolaikinėje visuomenėje. Intensyvus plastiko naudojimas ir kaupimasis aplinkoje sukelia aplinkosauginių iššūkių. Šios problemos aktualumą dar labiau išryškina ir tai, kad plastikas yra viena iš gausiausių atliekų rūšių ir pagal kiekį užima trečią vietą pasaulyje (Yatoo ir kt., 2024). Dabartinės plastiko atliekų tvarkymo strategijos apima šalinimą sąvartynuose (79 %), deginimą (12 %) ir mechaninį perdirbimą (9 %) (Geyer ir kt., 2017). Nors plastiko atliekų šalinimas sąvartynuose vis dar yra vyraujantis jų tvarkymo būdas, šis metodas laikomas neefektyviu dėl galimo dirvožemio ir gruntinio vandens užteršimo. Pasak Fayshal (2024), prognozuojama, kad iki 2060-ųjų m. plastiko atliekų kiekis pasieks 1 milijardą tonų. Patekus į aplinką, plastiko produktai ilgainiui pradeda fragmentuoti į mažesnes plastiko daleles, kurios yra vadinamos mikroplastiku.

Iki šiol mikroplastikas jau buvo aptiktas įvairiose ekosistemose (vandens ir sausumos aplinkose) ir skirtinguose organizmuose (žuvyse, paukščiuose ir žinduoliuose). Nors mikroplastiko poveikis gyviesiems organizmams nėra visapusiškai ištirtas, naujausių mokslinių tyrimų duomenys rodo, kad šios dalelės gali sukelti mechaninius audinių pažeidimus, uždegimines reakcijas, oksidacinį stresą ir sutrikdyti ląstelinius bei fiziologinius procesus (Jung ir kt., 2025).

Mažo tankio polietilenas (*angl.* low-density polyethylene, LDPE) yra viena plačiausiai naudojamų plastiko rūšių. Itin daug LDPE kilmės plastiko yra naudojama žemės ūkio sektoriuje. Be to, LDPE mulčiavimo plėvelės yra laikomos pagrindiniu žemės ūkio plastiko atliekų šaltiniu (Koskei ir kt., 2021). Iš žemės ūkio plastiko atliekų atskilęs mikroplastikas gali patekti į orą pakeltas vėjo arba būti išplautas audrų metu ir patekti į vandens sistemas. LDPE plėvelių perdirbimas dažnai yra techniškai ir ekonomiškai neįmanomas dėl jų daugiasluoksnės struktūros, skirtingų priedų kiekio ir didelio užterštumo dirvožemiu bei organinėmis medžiagomis (Carrieri ir kt., 2025).

Dėl mikroplastiko atsparumo irimo procesams ir didelės taršos aplinkoje, yra ieškoma efektyvesnių šalinimo bei skaidymo technologijų. Pažangūs oksidaciniai procesai (*angl.* advanced oxidation processes, AOPs) yra laikomi vienu efektyviausių metodų mikroplastiko dalelių šalinimui. Ankstesniuose tyrimuose, įvairūs katalizatoriai (puslaidininkiai, metalų oksidai (TiO_2, ZnO), anglies pagrindu pagamintos nanomedžiagos ir nanokompozitai) buvo taikomi mikroplastiko degradacijai (Kaur ir Kaur,

2025). Minėtos medžiagos pasižymi aukštu fotokatalitiniu efektyvumu, tačiau didelė jų dalis yra sintetinės kilmės, neekonomiškos ir potencialiai pavojingos aplinkai (Ahmed ir kt., 2025). Tvarių alternatyvų paieškos, ypač natūralių medžiagų naudojimas nanokompozitų sintezei, reikšmingai didina fotokatalitinės degradacijos taikymo potencialą. Šiame tyrime buvo pasirinkti TiO_2-molio (kaolinito, *angl.* kaolinite (Kao) ir montmorilonito *angl.* montmorillonite, (MMT)) nanokompozitai, kurie yra plačiai prieinami, ekonomiškai efektyvūs, turi didelį specifinį paviršiaus plotą ir universalų funkcionalumą (Ding ir kt., 2022).

Didžioji dalis mokslinių tyrimų yra atlikti su laboratorinio grynumo mikroplastiku, kuris neatspindi realaus plastiko sudėties kompleksiškumo (Ramírez-Escárcega ir kt., 2025). Aplinkoje aptinkamos mikroplastiko dalelės pasižymi skirtingomis fizikinėmis ir cheminėmis savybėmis, tokiomis kaip: polimero tipas, priedų kiekis ir cheminė prigimtis, paviršiaus morfologija, dydis, spalva. Kiekviena iš šių savybių gali nulemti mikroplastiko fotokatalitinės degradacijos efektyvumą. Todėl labai svarbu išsamiai ištirti aplinkoje labiausiai paplitusių mikroplastiko dalelių fotokatalitinės degradacijos procesus, siekiant išplėsti žinias, kaip šių dalelių fizikinės ir cheminės savybės nulemia jų degradacijos efektyvumą.

Aktualumas

Klasikiniai plastiko ir mikroplastiko atliekų tvarkymo metodai dažnai yra lėti ir nepakankamai efektyvūs. Fotokatalitinė degradacija yra vienas perspektyviausių, aplinkai nekenksmingų metodų, kuris leidžia sudėtingas polimerų struktūras suskaidyti iki pirminių medžiagų. Šio proceso tyrimas vandeninėje terpėje yra ypač reikšmingas, nes jį galima toliau taikyti nuotekų valymo įrenginiuose (NVĮ), kurie laikomi pagrindiniu barjeru tarp antropogeninės veiklos ir natūralių vandens telkinių. Europos Parlamentas persvarstytoje miesto nuotekų valymo direktyvoje (ES) 2024/3019 nurodė, kad iki 2045-ųjų bent 80% mikroplastiko turėtų būti pašalinama iš miesto nuotekų vandens (European Parliament and Council of the European Union, 2024). Išsamūs mikroplastiko fotokatalitinės degradacijos tyrimai, apimantys reakcijos parametrų poveikio vertinimą, mikroplastiko fizikocheminių savybių įtakos analizę ir reaktyviųjų deguonies rūšių (*angl.* reactive oxygen species, ROS) susidarymą, suteikia naujų žinių apie mikroplastiko mineralizacijos procesus realiomis sąlygomis. Tokių tyrimų rezultatai prisideda prie efektyvių vandens valymo technologijų vystymo ir plastiko taršos mažinimo metodų kūrimo.

Pagrindinis tyrimo tikslas

Šio darbo tikslas yra įvertinti LDPE mikroplastiko dalelių fotokatalitinės degradacijos efektyvumą ir mechanizmus, naudojant TiO_2 pagrindu susintetintas nanomedžiagas vandeninėje terpėje.

Uždaviniai

1. Susintetinti TiO_2, TiO_2-Kao ir TiO_2-MMT nanomedžiagas, taikant zolio-gelio sintezės metodą ir susintetinti Ag-TiO_2 nanomedžiagas, su skirtingomis Ag koncentracijomis, taikant fotoredukcijos metodą.
2. Nustatyti TiO_2 pagrindu susintetintų nanomedžiagų struktūrines, morfologines, optines ir chemines savybes.
3. Ištirti fragmentinio tipo LDPE mikroplastiko fotokatalitinę degradaciją, atsižvelgiant į reakcijos sąlygas (katalizatoriaus kiekį, tirpalo pH ir joninę jėgą).
4. Ištirti plėvelės tipo LDPE mikroplastiko fizikinių savybių įtaką fotokatalitinės degradacijos efektyvumui.
5. Įvertinti reaktyviųjų deguonies rūšių (*angl.* reactive oxygen species, ROS) susidarymą fotokatalitinės degradacijos sistemoje ir pasiūlyti galimus reakcijos mechanizmus.

Mokslinis naujumas

Šiame darbe buvo tiriamos komercinės mulčiavimo plėvelės ir natūralaus molio pagrindu susintetinti, TiO_2 pagrindu veikiantys nanokompozitai. Įvertinti fizikiniai ir cheminiai veiksniai, nulemiantys degradacijos procesus ir atlikta mechanistinė ROS susidarymo analizė. Gauti tyrimų rezultatai padeda geriau suprasti sudėtingų teršalų savybes ir turi tiesioginę praktinę reikšmę, kuriant mikroplastiko šalinimo technologijas.

Ginamieji teiginiai

1. TiO_2 nanodalelių (NDs) modifikavimas moliu ir metalo NDs padidina TiO_2 NDs fotokatalitinį aktyvumą. Tai nulemia didesnį LDPE mikroplastiko degradacijos efektyvumą, lyginant su nemodifikuotomis TiO_2 NDs.
2. Fragmentinio tipo LDPE mikroplastiko fotokatalitinės degradacijos efektyvumas gerinamas optimizuojant pagrindinius reakcijos parametrus: taikant rūgštinę reakcijos terpę, didesnę katalizatoriaus koncentraciją ir ilgesnę UV spinduliuotės poveikio trukmę.

3. Plėvelės tipo LDPE mikroplastiko fizikinės savybės, ypač dydis ir spalva, nulemia fotokatalitinės degradacijos efektyvumą. Mažesnio dydžio, juodos LDPE mikroplastiko plėvelės degraduoja du kartus efektyviau nei to paties dydžio permatomos LDPE plėvelės.

4. Hidroksilo radikalai *(·OH)* ir superoksido anijono radikalai ($O_2^{\cdot -}$) yra pagrindinės ROS, inicijuojančios ir kontroliuojančios LDPE fotokatalitinės degradacijos procesą, naudojant Ag-TiO_2 nanomedžiagas.

Autoriaus indėlis

Disertacijos autorė atliko nanomedžiagų sintezę (TiO_2, TiO_2-Kao, TiO_2-MMT, Ag-TiO_2), planavo ir vykdė LDPE mikroplastiko fotokatalitinės degradacijos eksperimentus. Autorė charakterizavo susintetintas nanomedžiagas, atliekant UV-Vis ir ATR-FTIR matavimus, aktyviai dalyvavo, vykdant XRD, SEM, TEM ir XRF matavimus bei savarankiškai analizavo ir interpretavo visų minėtų tyrimų rezultatus. Autorė atliko fotokatalitinės degradacijos eksperimentų duomenų analizę ir validaciją, parengė grafines pateiktis, rašė ir redagavo originalius straipsnių rankraščius ir pristatė savo rezultatus nacionalinėse ir tarptautinėse konferencijose.

METODIKA

Nanomedžiagų sintezė

TiO_2 NDs buvo susintetintos zolio-gelio (*angl.* sol-gel) metodu, remiantis ankstesniais moksliniais tyrimais (Liu ir kt., 2007; Zhang ir kt., 2011). Pirmiausia paruošiamas Ti^+ tirpalo pirmtakas, sumaišius $TiCl_4$ su 2 M HCl tirpalu ledo vonioje. Gautas mišinys praskiedžiamas 3–4 °C temperatūros dejonizuotu vandeniu, lašinama 5 M NH_4OH, kol reakcijos mišinio pH pasiekia 2–3. Gauta suspensija buvo maišoma 6 val. 650 aps./min greičiu, po to brandinama 12 val. Po minėtos reakcijos susidariusios nuosėdos buvo centrifuguojamos, kelis kartus plaunamos dejonizuotu vandeniu ir etanoliu, džiovinamos džiovinimo krosnyje (“Snol” 67/350, Umega, Lietuva) 70 °C temperatūroje 24 val. ir kalcinuojamos 500 °C temperatūroje 1 val. mufelinėje krosnyje (“Snol” 8.2/110, AB Utenos Elektrotechnika, Lietuva).

TiO_2-Kao ir TiO_2-MMT nanokompozitai taip pat buvo susintetinti zolio-gelio metodu. Pirmiausia 4 g kiekvieno molio buvo sumaišyti su 400 ml dejonizuoto vandens atskirose laboratorinėse stiklinėse ir maišomi dar 5 val. kambario temperatūroje, siekiant užtikrinti susidariusios suspensijos homogeniškumą. Po to, į paruoštą suspensiją buvo sulašinta 100 ml Ti^+

pirmtako. Į gautą mišinį lašinama 5 M NH_4OH, kol pasiekiama pH vertė 2–3. Mišinys buvo maišomas 70 °C temperatūroje 4 val., po to brandinamas 12 val. Susintetinti TiO_2-molio nanokompozitai buvo centrifuguojami, bent tris kartus plaunami dejonizuotu vandeniu ir etanoliu, džiovinami džiovinimo krosnyje 70 °C temperatūroje 24 val. ir kalcinuojami mufelinėje krosnyje 500 °C temperatūroje 1 val.

Ag-TiO_2 nanomedžiagos su skirtingomis Ag koncentracijomis buvo susintetintos taikant fotoredukcijos metodą (Huang ir kt., 2017). TiO_2 NDs (3 mmol) buvo sumaišomos su 100 ml dejonizuoto vandens. Į TiO_2 vandeninį tirpalą buvo sulašinama $AgNO_3$ su skirtingomis koncentracijomis (0,5 mmol; 1 mmol; 3 mmol). Gauti mėginiai patalpinami į uždarą UV kamerą, maišomi 6 val., apšviečiant 36 W UV-A šviesos šaltiniu (bangos ilgis: 365 nm). Susintetintos nanomedžiagos centrifuguojamos, plaunamos dejonizuotu vandeniu ir etanoliu, po to džiovinamos džiovinimo krosnyje 70 °C temperatūroje 10 val. Ag-TiO_2 nanomedžiagos buvo pažymėtos kaip: Ag-$TiO_2$0.5, Ag-$TiO_2$1 ir Ag-$TiO_2$3, atitinkamai nurodant sintezės metu naudotas Ag-NO_3 sidabro koncentracijas.

Nanomedžiagų charakterizavimas

Nanomedžiagų kristalinė fazė buvo apibūdinta rentgeno spindulių difrakcijos (XRD) metodu, naudojant „Rigatu SmartLab“ difraktometrą, su besisukančiu vario anodu ir ultratiesiniu D/Tex detektoriumi. Difrakcijos modeliai buvo užregistruoti „Bragg-Brentano“ nuskaitymo režimu 2θ intervale nuo 10° iki 80°, taikant 0,02º žingsnio dydį. TiO_2 NDs dydis susintetintuose TiO_2-Kao ir TiO_2-MMT nanokompozituose buvo įvertintas remiantis Scherrer lygtimi (*10 lygtis*) (Toro ir kt., 2020). Ag-TiO_2 nanomedžiagų vidutinis dydis buvo įvertintas taikant Halder-Vagner metodą, remiantis ankstesnių tyrimų rekomendacijomis (*11 lygtis*) (Nath ir kt., 2020).

TiO_2-molio nanokompozitų paviršiaus morfologija buvo analizuojama naudojant FEI Helios Nanolab 650 skenuojantį elektroninį mikroskopą (SEM). Prieš analizę, mėginiai buvo padengti anglies sluoksniu ir vaizdinami antrinių elektronų (SEI) režimu, esant 3 kV įtampai ir 100 pA srovei. Ag-TiO_2 morfologinės savybės buvo nustatytos naudojant peršviečiamąją elektroninę mikroskopiją (TEM). Mikroskopas FEI Tecnai F20 X-TWIN (FEI, Netherlands, 2011) buvo naudotas Ag-TiO_2 vaizdinimui. Mikrografijos buvo užfiksuotos, naudojant „Gatan Orius“ CCD kamerą, šviesiojo lauko režimu, esant 200 kV įtampai.

Furjė transformacijos infraraudonųjų spindulių (FTIR) spektroskopijos analizė buvo atlikta naudojant μ-FTIR (LUMOS II, Bruker, Vokietija, 2024)

spektrometrą su susilpninto visiškojo atspindžio (ATR) priedu. IR spektrai buvo registruojami 4000–680 cm^{-1} bangos skaičių diapazone, taikant 4 cm^{-1} skiriamąją gebą ir 128 skenavimus vienam mėginiui.

Susintetintų nanomedžiagų optinė absorbcija įvertinta UV-Vis spektrofotometrijos metodu, atliekant matavimus 250–800 nm bangos ilgių diapazone. Matavimams atlikti buvo naudotas UV-Vis spektrofotometras „Specord 210 Plus“ („Analytic Jena“, Vokietija). Draustinės juostos tarpo energija (E_g) apskaičiuota taikant Tauc lygtį (*12 lygtis*) (Tauc ir kt., 1966).

LDPE mikroplastiko parinkimas ir charakterizavimas

Analitinio grynumo, fragmentinio tipo LDPE mikroplastikas (~300 µm) buvo įsigytas iš „Goodfellow“ (Vokietija). Fragmentinio tipo LDPE dalelės pasižymėjo mažu tankiu, lankstumu ir hidrofobinėmis savybėmis. Komerciškai prieinamos LDPE plastiko plėvelės buvo įsigytos prekybos centre „Ermitažas“ (Lietuva). Šiame tyrime buvo naudotos juodos ir permatomos LDPE plėvelės, kurių storis siekė 120 µm. Plėvelės tipo LDPE mikroplastikas buvo supjaustytas į dvi dydžių grupes 1×1 mm ir 3×3 mm, naudojant pjaustyklę „Fellowes Neutron Plus“ (Dongguan, Kinija).

Siekiant išanalizuoti LDPE mikroplastiko chemines savybes, mėginiai buvo tirti taikant FTIR spektroskopiją (µ-FTIR LUMOS II, Bruker, Vokietija, 2024) ATR režimu. IR spektrai buvo registruojami atliekant 128 skenavimus 4000–680 cm^{-1} bangos skaičių diapazone, taikant 4 cm^{-1} skiriamąją gebą. Fragmentinio ir plėvelės tipų LDPE mikroplastikas buvo matuojamas penkiose pasirinktose pozicijose, pagal Kaewkam ir kt. (2022) rekomendacijas (*8 pav.*).

Plėvelės tipo LDPE mikroplastiko paviršiaus morfologija buvo analizuojama atliekant SEM vaizdinimą. Prieš matavimus LDPE mikroplastikas buvo padengtas chromu (žr. 2.5.2 skyrelį).

Rentgeno spindulių fluorescencijos (WDXRF) analizė buvo atlikta naudojant „Axios mA“ spektrometrą („Panalytical“, Nyderlandai), siekiant apibūdinti LDPE plėvelių elementinę sudėtį. Elementinė analizė nuo deguonies (O) iki urano (U) atlikta naudojant šešis kristalinius analizatorius. Sistema buvo sukalibruota pagal sertifikuotas etalonines medžiagas.

Fotokatalitinės degradacijos tyrimas

Fotokatalitinės degradacijos eksperimentai buvo vykdomi uždaroje UV kameroje (*angl.* UV chamber) su 36 W UV-A šviesos šaltiniu, naudojant 365 nm bangos ilgį. Šio bangos ilgio pasirinkimas grindžiamas tuo, kad TiO_2

pasižymi didžiausia šviesos sugertimi artimos UV spinduliuotės srityje (Zhou ir kt., 2024). UV spinduliuotės šaltinis buvo įrengtas 10 cm aukštyje virš tiriamojo mėginio. Fotokatalitinė reakcija buvo vykdoma kambario temperatūros sąlygomis (22–24 °C) pasirinktą laiko periodą.

Atliekant fragmentinio tipo LDPE fotokatalitinės degradacijos tyrimą, į Petri lėkštelę buvo atsveriama 20 mg LDPE mikroplastiko ir atitinkamo katalizatoriaus (TiO_2, TiO_2-Kao arba TiO_2-MMT), kuris buvo suspenduojamas 10 mL dejonizuoto vandens. Paruoštas reakcijos mišinys buvo perkeliamas į UV kamerą, reakcija buvo vykdoma nuo 60 iki 480 min. Šiame tyrime taip pat buvo tiriama įvairių parametrų įtaka fotokatalitinės degradacijos efektyvumui (LDPE ir katalizatoriaus masių santykio (1:2; 1:1; 2:1), reakcijos terpės pH (3–11) ir joninės jėgos (0,05–0,5 $molL^{-1}$)).

Plėvelės tipo LDPE mikroplastiko tyrimuose pirmiausia vienas iš pasirinktų katalizatorių (TiO_2, Ag-$TiO_2$0.5, Ag-$TiO_2$1 arba Ag-$TiO_2$3) buvo suspenduotas 10 mL dejonizuoto vandens. Tuomet į suspensiją buvo pridedama plėvelės tipo LDPE mikroplastiko (1 g/L). Paruoštas reakcijos mišinys buvo perkeliamas į UV kamerą. Reakcija buvo vykdoma 60–960 min trukmės laiko intervalais. Eksperimentinė reakcijos schema pateikiama *9 pav.*

Kontroliniai fotokatalitinės degradacijos eksperimentai su fragmentinio ir plėvelės tipų LDPE mikroplastiku buvo atliekami laikantis tos pačios procedūros, tačiau nepridedant katalizatoriaus. Po fotokatalitinės degradacijos eksperimento, kiekvienas mėginys buvo filtruojamas per stiklo pluošto filtrą („Branchia“, 50 mm, porų dydis: 1,6 µm, Vokietija), kelis kartus plaunamas dejonizuotu vandeniu ir džiovinamas džiovinimo krosnyje 40 °C temperatūroje 60 min.

LDPE analizė po degradacijos proceso

LDPE mikroplastiko šalinimo efektyvumas buvo įvertintas taikant gravimetrinį analizės metodą ir skaičiuojant masės netekimą po fotokatalitinės degradacijos (*13 lygtis*). Masės netekimo apskaičiavimas yra vienas iš plačiausiai naudojamų mikroplastiko degradacijos vertinimo metodų, nes jis leidžia kiekybiškai nustatyti šalinimo efektyvumą (Kinyua ir kt., 2024; Tan ir kt., 2023).

Plėvelės tipo LDPE paviršiaus morfologijos pokyčiams įvertinti buvo taikomas SEM vaizdinimas naudojant FEI Helios Nanolab 650 mikroskopą. Prieš SEM matavimus kiekviena LDPE plėvelė buvo padengta chromu. LDPE plėvelės buvo vaizdinamos SEI režimu, esant 3 kV įtampai ir 100 pA srovei.

Funkcinių grupių pokyčiai po fotokatalitinės degradacijos buvo įvertinti naudojant µ-FTIR (LUMOS II, Bruker, Vokietija, 2024)

spektrometrą su ATR priedu. IR spektrai buvo registruojami 4000–680 cm^{-1} bangos skaičių diapazone, taikant 4 cm^{-1} skiriamąją gebą ir 128 skenavimus vienam mėginiui. Oksidaciniai polimerinės grandinės pokyčiai taip pat buvo įvertinti apskaičiuojant karbonilo indeksą (*angl.* carbonyl index, CI) ir vinilo indeksą (*angl.* vinyl index, VI) (*15, 16 lygtys*).

ROS slopinimo eksperimentai

ROS slopinimo tyrimai (*angl.* quenching test) yra kokybinis metodas, pagrįstas specifiniu cheminių reagentų veikimu, kurie reaguoja su konkrečiomis ROS, taip slopindami fotokatalitinę LDPE degradaciją.

Šiame tyrime, pagrindinės ROS, inicijuojančios ir kontroliuojančios LDPE degradacijos reakcijas, buvo nustatytos naudojant izopropilo alkoholį (IPA) (10 mM), askorbo rūgštį (AA) (2 g/L) ir amonio oksalatą (AO) (1 g/L), kurie atitinkamai slopina hidroksilo radikalus ($\cdot OH$), superoksido anijonus ($O_2^{\cdot -}$) ir teigiamai įkrautas elektronų skyles (h^+). ROS slopinimo tyrimai buvo atlikti po 240 min, laikantis tos pačios procedūros, kaip ir vykdant fotokatalitinės degradacijos tyrimus (*žr. 2.4 skyrelį*).

REZULTATAI

NANOMEDŽIAGŲ CHARAKTERIZAVIMAS

XRD struktūrinė analizė

TiO_2, TiO_2-Kao ir TiO_2-MMT rentgeno spindulių difraktogramos pateiktos *10 (a) pav.* Smailės ties 27,38° (110), 36,08° (101), 39,29° (200), 41,22° (111), 44,16° (210), 54,32° (211), 56,61° (211), 62,89° (002), 64,23° (310), 69,01° (301) ir 69,89° (112) atitinka rutilo fazės TiO_2 (PDF Card No.: 04-004-4337), o smailės ties 25,34° (101) ir 48,05° (200) rodo anatazės fazės TiO_2 (PDF Card No.: 04-002-2750). Kaolinitas nustatytas pagal difrakcijos smailes ties 21,9° ir 26,6° (PDF Card No.: 00-005-0143), o montmorilonitas identifikuotas pagal smailę ties 35,02° (PDF Card No.: 00-029-1499). Rutilo fazės TiO_2 difrakcijos smailės ties 39,29°, 44,16°, 56,61°, 62,80°, 64,23°, 69,01° ir 69,89° nebuvo užfiksuotos TiO_2-Kao ir TiO_2-MMT nanokompozituose. Tai rodo sėkmingą TiO_2 nusodinimą ant molių paviršiaus. Vidutinis TiO_2 NDs dydis siekė 40–60 nm.

Ag-$TiO_2$0.5, Ag-$TiO_2$1 ir Ag-$TiO_2$3 rentgeno spindulių difraktogramos pateiktos *10 (b) pav.* Difrakcijos smailės ties 25,31° (101), 36,95° (103), 38,58° (112), 48,04° (200), 53,90° (105), 55,07° (211), 62,69° (204), 68,76° (116), 70,30° (220) ir 75,06° (215) buvo priskirtos anatazės fazės TiO_2 (PDF

Card No.: 04-014-5762). Aiškiai atskirtos TiO_2 smailės rodo, kad Ag^+ jonai pirmiausia nusėda TiO_2 paviršiuje, o ne integruojasi į kristalinę gardelę. Difrakcijos smailės, esančios ties 38,12° (111), 44,28° (200), 64,43° (220) ir 77,47° (311), priskiriamos metalinio sidabro fazei. Didinant $AgNO_3$ koncentraciją fotoredukcinėje sintezėje, Ag smailės tapo intensyvesnės. Tai siejama su Ag^+ jonų koncentracijos padidėjimu, kuris inicijuoja metalinės fazės Ag susidarymą. Vidutinis Ag NDs dydis siekė 19 nm.

ATR-FTIR spektrinė analizė

TiO_2, TiO_2-Kao ir TiO_2-MMT FTIR spektrai yra pateikti *11 pav.* TiO_2 absorbcijos juostos, aptiktos bangos skaičių diapazone nuo 800 cm^{-1} iki 680 cm^{-1}, buvo priskirtos titano-deguonies-titano (Ti-O-Ti) ryšio tempimo virpesiams. TiO_2-Kao nanokompozite kaolinitui būdingos absorbcijos juostos nustatytos ties 1054 cm^{-1}, 754 cm^{-1} ir 720 cm^{-1}. Tipinės montmorilonito absorbcijos juostos TiO_2-MMT nanokompozite buvo aptiktos ties 1037 cm^{-1}, 917 cm^{-1} ir 720 cm^{-1}. Absorbcijos juosta ties 1030 cm^{-1} yra būdinga molio kristalams ir įprastai priskiriama silicio-deguonies (Si-O) ryšiui, o šiuo atveju rodo Si-O-Si ir O-Si-O ryšių tempimo virpesius (Li ir Yang, 2014). TiO_2-Kao ir TiO_2-MMT nanokompozituose Si-O tempimo virpesių juostos yra pasislinkusios į ilgesnių bangos skaičių sritį, šiuo atveju tai rodo naujų cheminių sąveikų susidarymą tarp TiO_2 paviršiaus ir Si-O grupių.

12 pav. pateikiami TiO_2, Ag-$TiO_2$0.5, Ag-$TiO_2$1 ir Ag-$TiO_2$3 FTIR spektrai. Plati absorbcijos juosta ties 800–680 cm^{-1} yra būdinga Ti-O-Ti ryšio tempimo virpesiams. Sidabro nusodinimas ant TiO_2 paviršiaus nepakeitė TiO_2 būdingų absorbcijos juostų ir rodo tik nedidelius spektrinius pokyčius. Didinant $AgNO_3$ kiekį sintezės reakcijos sistemoje, pastebėtas Ti-O-Ti ryšio tempimo virpesių intensyvumo sumažėjimas, kuris yra siejamas su Ag ir TiO_2 sąveika. Be to, būdingų sidabro oksido absorbcijos juostų nebuvimas rodo, kad Ag išlieka metalinėje fazėje, nesusidarant atskirai oksido fazei.

SEM ir TEM vaizdinimas

TiO_2, kaolinito, montmorilonito, TiO_2-Kao ir TiO_2-MMT SEM mikrografijos pateikiamos *13 pav.* TiO_2 NDs pasižymėjo sferine arba netaisyklinga forma ir buvo linkusios agreguoti (*13 (a, b) pav.*). Kaolinito molio mineralams buvo būdinga lakštinė struktūra, pasižyminti pseudo-heksagonine struktūra ir lygiu paviršiumi (*13 (c, d) pav.*). Tuo tarpu, montmorilonitas pasižymėjo šiurkščios tekstūros sluoksniais, kurie buvo linkę agreguoti ir sudaryti klasterius (*13 (e, f) pav.*). Nustatytos molių morfologinės

savybės atitinka literatūroje pateikiamas molio morfologines charakteristikas (Ural, 2021).

TiO_2 NDs buvo sėkmingai nusodintos ant molių paviršiaus (*13 (g–j) pav.*). Po TiO_2 NDs nusodinimo ant kaolinito, šio molio paviršius išliko plokščias, lygus ir pseudo-heksagoninės struktūros (*13 (g, h) pav.*). Lyginant su TiO_2-Kao, TiO_2-MMT pasižymėjo kur kas netolygesniu TiO_2 NDs pasiskirstymu montmorilonito paviršiuje (*13 (i, j) pav.*). Taip pat buvo pastebėta, jog TiO_2 NDs agregacija ant montmorilonito paviršiaus buvo ryškesnė, palyginti su kaolinitu.

TEM vaizdinimas buvo pritaikytas Ag-$TiO_2$0.5, Ag-$TiO_2$1 ir Ag-$TiO_2$3 nanomedžiagų morfologinių paviršiaus savybių analizei (*14 pav.*). TEM analizė parodė, kad TiO_2 NDs pasižymi netaisyklinga forma ir plačiu dydžių pasiskirstymu, o jų vidutinis dydis siekia 130 nm. Tamsių sričių atsiradimas TiO_2 paviršiuje rodo Ag NDs. TiO_2 NDs dydis ir forma išliko nepakitę po sidabro nusodinimo. Tamsių sričių plotas yra didesnis nanomedžiagose, kurių sintezei buvo naudojama didesnė $AgNO_3$ koncentracija. Tai siejama su sėkmingai atlikta fotoredukcine nanomedžiagų sinteze.

Optinių savybių tyrimas

TiO_2, TiO_2-Kao ir TiO_2-MMT optinės savybės buvo įvertintos remiantis UV-Vis absorbcijos spektrais (*15 pav.*). Kiekvieno katalizatoriaus draustinės juostos tarpo energijai (E_g) nustatyti buvo taikoma Tauc lygtis. TiO_2-molio nanokompozituose Eg vertės sumažėjo nuo 3,10 eV (grynos TiO_2 NDs) iki 2,95 eV (TiO_2-MMT) ir 2,88 eV (TiO_2-Kao). Draustinės juostos tarpo energijos sumažėjimas yra siejamas su heterostruktūrų susidarymu ir Ti-O-Si (arba Ti-O-Al) ryšių formavimusi, kurie pakeičia elektroninę TiO_2 struktūrą.

TiO_2 ir Ag-TiO_2 nanomedžiagų, su skirtingomis Ag koncentracijomis, UV-Vis absorbcijos spektrai yra pateikti *16 (a) pav*. Maksimali TiO_2 absorbcijos smailė buvo aptikta ties 330 nm. Nusodinus Ag ant TiO_2 paviršiaus, absorbcijos juosta pasislinko į ilgesnių bangos ilgių sritį. Maksimalios Ag-$TiO_2$0.5, Ag-$TiO_2$1 ir Ag-$TiO_2$3 absorbcijos smailės atitinkamai buvo aptiktos ties 331 nm, 340 nm ir 358 nm. Šis poslinkis link regimosios šviesos srities yra siejamas su paviršiaus plazmonų rezonanso (*angl.* surface plasmon resonance (SPR)) efektu.

FRAGMENTINIO TIPO LDPE FOTOKATALITINĖ DEGRADACIJA NAUDOJANT TiO_2-MOLIO NANOKOMPOZITUS

Reakcijos trukmės įtaka fragmentinio tipo LDPE fotokatalitinei degradacijai

Fragmentinio tipo LDPE mikroplastiko fotokatalitinė degradacija buvo tiriama skirtingais laiko intervalais (60–480 min) esant neutraliam tirpalo pH (*17 (a, b) pav.*). Naudojant grynas TiO_2 NDs, LDPE masės netekimas po 60 min siekė 13,29 %, o po 480 min padidėjo iki 14,66 %. Tuo tarpu, LDPE masės netekimas po 60 min, naudojant TiO_2-MMT ir TiO_2-Kao, atitinkamai padidėjo iki 14,90 % ir 17,08 %. Padidinus fotokatalitinės reakcijos trukmę iki 480 min, LDPE masės netekimas išaugo iki 21,25 % su TiO_2-MMT ir iki 28,36 % su TiO_2-Kao. Pradiniame fotodegradacijos etape LDPE masės netekimas yra siejamas su mažos molekulinės masės ir lakiųjų junginių (aldehidų, ketonų, alkoholių, karboksirūgščių ir eterių) susidarymu (Ainali ir kt., 2021). Šie rezultatai rodo, kad ilgesnis poveikis UV-A spinduliuote didina LDPE fotokatalitinės degradacijos efektyvumą, ypač atliekant reakcijas su TiO_2 ir molio nanokompozitais.

TiO_2 ir molio nanokompozitai pasižymėjo didesniu LDPE fotokatalitinės degradacijos efektyvumu, palyginti su grynomis TiO_2 NDs. Po 480 min užfiksuotas LDPE masės netekimas su TiO_2-MMT buvo apytiksliai pusantro karto didesnis, o su TiO_2-Kao beveik dvigubai didesnis, lyginant su LDPE masės netekimu reakcijos sistemoje tik su TiO_2. Pagerintas TiO_2 fotokatalitinis efektyvumas siejamas su kaolinito ir montmorilonito savybėms, tokiomis kaip didelis paviršiaus plotas, poringumas, aukšta adsorbcijos talpa. Montmorilonitas pasižymi sluoksniuota struktūra, didesniu paviršiaus plotu ir didesne katijonų mainų geba. Šios montmorilonito savybės reikšmingai prisideda prie pagerintų TiO_2 fotokatalitinių savybių. Tuo tarpu kaolinitas turi daugiau hidroksilo grupių sluoksnių kraštuose, kurios inicijuoja ROS susidarymą reakcijos tirpale (Cao ir kt., 2021).

Pseudo pirmo laipsnio modelis gerai aprašė visų trijų katalizatorių (TiO_2, TiO_2-MMT ir TiO_2-Kao) kinetiką, o tai patvirtino aukštos determinacijos koeficiento (R^2) vertės (*9 lentelė*). Didžiausia R^2 vertė nustatyta naudojant TiO_2-Kao ($R^2 = 0{,}984$). Apskaičiuotos LDPE degradacijos greičio konstantos (k), taikant TiO_2, TiO_2-MMT ir TiO_2-Kao, atitinkamai siekė $3{,}79 \cdot 10^{-2}$ min^{-1}, $4{,}09 \cdot 10^{-2}$ min^{-1} ir $4{,}49 \cdot 10^{-2}$ min^{-1}. Remiantis kinetinės analizės rezultatais, TiO_2-Kao pasižymėjo palankiausiomis fotokatalitinėmis savybėmis.

Fragmentinio tipo LDPE FTIR spektroskopinė analizė

Nepaveiktų UV-A šviesa fragmentinio tipo LDPE mikroplastiko dalelių FTIR spektrai parodė charakteringas absorbcijos juostas, kurios yra būdingos LDPE polimerams (*18 (a, b) pav.*). Absorbcijos juosta ties 2800 cm^{-1}–3000 cm^{-1} priskiriama simetriniams ir asimetriniams CH_2 tempimo virpesiams. Ryški smailė ties 1463 cm^{-1} atitinka CH_2 lenkimo virpesius, o smailė ties 1378 cm^{-1} priskiriama CH_3 lenkimo virpesiams (Jia ir kt., 2024).

Funkcinių grupių pokyčiai LDPE polimeruose buvo pastebėti po 60 min fotokatalitinės degradacijos, ypač naudojant TiO_2-MMT ir TiO_2-Kao. Nauja absorbcijos smailė ties 2023 cm^{-1} priskiriama aldehidų C–H tempimo virpesiams. Plačios absorbcijos juostos susidarymas ties 1850–1700 cm^{-1} priskiriamas C=O tempimo virpesiams karboksirūgštyse arba ketonuose. Po 480 min fotokatalitinės reakcijos LDPE spektruose buvo užfiksuotas charakteringų LDPE smailių išplatėjimas, rodantis polimerinės grandinės skilimą, padidėjusį šakotumą ir CH_2 bei CH_3 grupių susidarymą. Šie polimerinės grandinės pokyčiai taip pat yra siejami su polimero kristališkumo sumažėjimu, dėl kurio susidaro daugiau jautrių sričių foto-oksidacijos procesams. Po 480 min fotokatalitinės degradacijos, absorbcijos juostos intensyvumas ties 1752 cm^{-1} (C=O) reikšmingai padidėjo. FTIR spektrų analizė patvirtino, kad TiO_2-MMT ir TiO_2-Kao pasižymi didesniu fotokatalitiniu efektyvumu, kuris nulemia ankstesnį ir intensyvesnį karbonilo grupių susidarymą.

CI buvo apskaičiuotas, siekiant kiekybiškai įvertinti LDPE degradacijos procesą (*18 (c) pav.*). Atitinkamai po 60 min ir 480 min fotokatalitinės degradacijos CI vertės padidėjo nuo 0,61 ± 0,15 iki 0,74 ± 0,08, naudojant grynas TiO_2 NDs. Tuo tarpu naudojant TiO_2-MMT ir TiO_2-Kao CI vertės buvo aukštesnės ir atitinkamai padidėjo nuo 0,95 ± 0,18 iki 1,26 ± 0,14 ir nuo 1,24 ± 0,14 iki 1,41 ± 0,09. Reikšmingiausi funkcinių grupių pokyčiai LDPE polimerinėje grandinėje buvo nustatyti, atliekant fotokatalitines reakcijas su TiO_2-Kao.

Fragmentinio tipo LDPE ir katalizatoriaus masių santykio įtaka

LDPE mikroplastiko fotokatalitinės degradacijos efektyvumas priklausė nuo masės santykio tarp LDPE ir katalizatoriaus. Padidinus katalizatoriaus dozę nuo 10 mg iki 40 mg, LDPE skaidymo efektyvumas padidėjo nuo 9,27 % iki 22,59 % su TiO_2 NDs, nuo 10,99 % iki 23,03 % su TiO_2-MMT ir nuo 14,55 % iki 25,98 % su TiO_2-Kao (*19 pav.*). LDPE masės netekimo padidėjimas yra siejamas su padidėjusiu katalizatoriaus paviršiaus

plotu, kuris nulemia padidėjusių aktyviųjų centrų skaičių ir pagreitina ROS susidarymą reakcijos tirpale (Tan ir kt., 2023). Kai katalizatoriaus kiekis reakcijos tirpale buvo mažesnis nei LDPE (1:2), fotokatalitinės degradacijos efektyvumas buvo mažiausias.

Šiame tyrime nustatyta optimali katalizatoriaus dozė atitinka literatūroje aprašytas vertes. Uogintė ir kt. (2023) nustatė, kad padidinus katalizatoriaus ir mikroplastiko masių santykį iki 2:1, PE mikroplastiko masės netekimas padidėjo iki 6,5 %. Kitame tyrime buvo užfiksuota, kad LDPE mikroplastiko masės netekimas padidėjo, kai katalizatoriaus koncentracija buvo padidinta nuo 500 ppm iki 1000 ppm. Tačiau toliau didinant katalizatoriaus koncentraciją nuo 1000 ppm iki 1500 ppm, masės netekimas sumažėjo 6,68 % (Tan ir kt., 2023). Pasiekus tam tikrą katalizatoriaus koncentraciją, degradacijos efektyvumo sumažėjimas siejamas su padidėjusiu tirpalo drumstumu, kuris sumažina šviesos prasiskverbimą ir ROS susidarymą reakcijos tirpale (Abdel-Khalek ir kt., 2018).

Reakcijos terpės pH ir joninės jėgos įtaka fragmentinio tipo LDPE degradacijai

LDPE fotokatalitinės degradacijos tyrimai buvo atlikti skirtingose pH terpėse, kurių pH vertės svyravo nuo 3 iki 11 (*20 pav.*). Didžiausias LDPE degradacijos efektyvumas nustatytas esant pH 3. Naudojant TiO_2 NDs, TiO_2-MMT ir TiO_2-Kao LDPE masės netekimas atitinkamai siekė 24,67 %, 25,28 % ir 30,96 %. Esant neutralioms tirpalo sąlygoms (pH 7) LDPE degradacijos efektyvumas buvo perpus mažesnis nei rūgštiniame tirpale (pH 3), šiuo atveju LDPE masės netekimas su atitinkamais katalizatoriais (TiO_2 NDs, TiO_2-MMT ir TiO_2-Kao) siekė 13,29 %, 14,56 % ir 17,08 %. Kai tirpalo pH vertė buvo padidinta iki 11, LDPE masės netekimas sumažėjo iki 4,75 %, 6,67 % ir 7,41 % atitinkamai naudojant TiO_2 NDs, TiO_2-MMT ir TiO_2-Kao. Efektyvesnė fotokatalitinė LDPE degradacija rūgštinėje terpėje yra siejama su padidėjusia vandenilio jonų (H^+) koncentracija tirpale (Ariza-Tarazona ir kt., 2020).

Tirpalo joninės jėgos poveikis LDPE fotokatalitinės degradacijos efektyvumui buvo tiriamas naudojant NaCl tirpalą (0,05–0,5 $molL^{-1}$) (*21 pav.*). LDPE degradacijos efektyvumas sumažėjo, didinat tirpalo joninę jėgą. Kai tirpalo joninė jėga buvo padidinta nuo 0 $molL^{-1}$ iki 0,5 $molL^{-1}$, LDPE masės netekimas atitinkamai sumažėjo nuo 13,29 % iki 7,82 % su TiO_2 NDs, nuo 14,56 % iki 9,48 % su TiO_2-MMT ir nuo 17,08 % iki 8,31 % su TiO_2-Kao. LDPE degradacijos efektyvumo sumažėjimas yra siejamas su mažėjančiomis stūmos jėgomis tarp neigiamai įkrautų mikroplastiko dalelių. Mažėjant stūmos

jėgoms, Van der Waals jėgos tampa dominuojančia trauka tarp mikroplastiko dalelių, todėl šios agreguojasi į didesnes grupes. Susidariusiems mikroplastiko dalelių agregatams yra būdingas padidėjęs hidrodinaminis skersmuo, o tai nulemia sumažėjusį dalelių difuzijos greitį ir bendrą judrumą (Lu ir kt., 2018). Be to, Na^+ ir Cl^- jonai turi įtakos katalizatorių elektrostatinėms savybėms, įprastai sukeldami jų agregavimą ir slopindami ROS susidarymą reakcijos tirpale.

Skyrelio išvados

TiO_2-MMT ir TiO_2-Kao nanokompozitų taikymas reikšmingai pagerino fragmentinio tipo LDPE mikroplastiko fotokatalitinės degradacijos efektyvumą vandeninėje terpėje. TiO_2 NDs draustinės juostos tarpo energija sumažėjo nuo 3,10 eV (TiO_2 NDs) iki 2,95 eV (TiO_2-MMT) ir 2,88 eV (TiO_2-Kao). Po 480 min fotokatalitinės degradacijos didžiausias LDPE masės netekimas nustatytas naudojant TiO_2-Kao ir siekė 28,36 %. FTIR spektrų analizė patvirtino LDPE polimerinės grandinės oksidaciją, o didžiausia CI vertė buvo aptikta naudojant TiO_2-Kao (CI = 1,41). Tyrimo rezultatai rodo, kad TiO_2-Kao pasižymi geromis struktūrinėmis ir morfologinėmis savybėmis ir turi aukštą potencialą mikroplastiko fotokatalitinės degradacijos tyrimuose.

Fotokatalitinės degradacijos sąlygų tyrimas parodė, kad LDPE degradacija yra efektyviausia rūgštinėje terpėje (pH 3), kur šių dalelių masės netekimas naudojant TiO_2-Kao siekė 30,96 %. Padidinus katalizatoriaus kiekį reakcijos sistemoje, LDPE masės netekimas padidėjo apie 10 % su visais tirtais katalizatoriais. Tirpalo joninės jėgos padidinimas iki 0,5 $molL^{-1}$ sumažino LDPE masės netekimą nuo 17,08 % iki 8,31 % naudojant TiO_2-Kao. Reakcijos parametrų analizė patvirtino, kad fotokatalitinės reakcijos sąlygų optimizavimas gali pagerinti LDPE degradacijos efektyvumą, padidinant LDPE masės netekimą ir sumažinant reakciją slopinančių faktorių įtaką.

PLĖVELĖS TIPO LDPE FOTOKATALITINĖ DEGRADACIJA NAUDOJANT AG-TiO_2 NANOMEDŽIAGAS

Plėvelės tipo LDPE savybių tyrimas

Šiame tyrime buvo naudotos komerciškai prieinamos, juodos ir permatomos LDPE plėvelės (*22 (a, d) pav.*). LDPE plėvelių paviršiaus morfologija buvo analizuojama taikant SEM vaizdinimą. Juodos LDPE plėvelės pasižymėjo paviršiaus nelygumais ir šiurkštumu, o permatomoms

LDPE plėvelėms buvo būdinga lygi paviršiaus struktūra, be pastebimų defektų (*22 (b, e) pav.*).

ATR-FTIR absorbcijos spektrai parodė LDPE polimerams būdingas absorbcijos juostas (Jung ir kt., 2018) (*22 (c, f) pav.*). Smailės ties ~2916 cm^{-1} ir ~2845 cm^{-1} atitinka asimetrinius ir simetrinius CH_2 ryšio tempimo virpesius. Absorbcijos juosta ties ~1462 cm^{-1} priskiriama CH_2 ryšio lenkimo virpesiams, o smailė ties ~717 cm^{-1} būdinga CH_2 ryšio siūbavimo virpesiams. Tačiau tarp juodų ir permatomų LDPE plėvelių buvo užfiksuoti funkcinių grupių skirtumai. Juoda LDPE plėvelė turi papildomą smailę ties ~873 cm^{-1}, kuri yra siejama su vinilo grupių (C=C) susidarymu (Miranda ir kt., 2021). Permatomose LDPE plėvelėse buvo užfiksuota plati absorbcijos juosta ties 892 cm^{-1} –770 cm^{-1}, kuri taip pat siejama su (C=C) grupių formavimusi. Nauja absorbcijos juosta permatomose LDPE plėvelėse buvo užfiksuota ir ties 3600 cm^{-1}–3200 cm^{-1}, priskiriama O–H grupių susidarymui. Dar viena smailė, aptikta permatomose LDPE plėvelėse ties 1661 cm^{-1} yra priskiriama C=O grupių atsiradimui. Deguonies turinčios grupės ir dvigubojo ryšio susidarymas LDPE polimerinėje grandinėje įprastai gali atsirasti dėl gamybos procesų, tokių kaip oksidacinės reakcijos polimerizacijos proceso metu arba dėl priedų, kurie įterpiami į polimero matricą (Wang ir kt., 2022).

XRF analizė parodė LDPE plėvelėse esančių neorganinių elementų cheminę sudėtį, kuri yra siejama su gaminimo metu pridedamais priedais, užpildais ir pigmentais (*12 lentelė*) (Carrieri ir kt., 2025). Permatomose plėvelėse buvo aptikti šie neorganiniai elementai: Na, Al, Si, Cl, Ca ir Zn, kurie sudarė mažiau nei 0,05 %. Įprastai, permatomų plėvelių gamybai naudojami itin gryni LDPE polimerai, norint išsaugoti plėvelių skaidrumą, todėl yra įtraukiamos tik tokios medžiagos kaip termoplastinis krakmolas, silicio oksidas, aerogelis arba cinko oksidas (Yang ir kt., 2022). Priešingai, juodose plėvelėse buvo daug daugiau neorganinių elementų, ypač Ca (25,2776 %) ir Ti (5,0056 %). Kitų neorganinių elementų (Na, K, Ni, Br, Sr, ir Ba) bendras kiekis sudarė iki 0,05 %. Ca kartu su Mg, Al ir Si naudojami siekiant padidinti paviršiaus šiurkštumą (Vallada ir kt., 2020). Juodose LDPE plėvelėse aptiktas Ti elementas yra siejamas su TiO_2, kuris itin dažnai naudojamas kaip UV stabilizatorius.

Plėvelės tipo LDPE fotokatalitinė degradacija naudojant Ag-TiO_2

Plėvelės tipo LDPE mikroplastiko fotokatalitinė degradacija buvo atlikta naudojant skirtingus katalizatorius: TiO_2, Ag-$TiO_2$0.5, Ag-$TiO_2$1 ir Ag-$TiO_2$3 (*26 pav.*). Didžiausias fotokatalitinės degradacijos efektyvumas buvo pasiektas su Ag-$TiO_2$1 ir Ag-$TiO_2$3. Juodos spalvos plėvelės (1×1 mm) buvo

degraduojamos efektyviausiai iš visų tirtų LDPE plėvelių. Po 960 min juodų LDPE plėvelių (1×1 mm) masės netekimas naudojant TiO_2, Ag-$TiO_2$0.5, Ag-$TiO_2$1 ir Ag-$TiO_2$3 atitinkamai siekė 3,08 % ± 0,15 %, 4,52 % ± 0,13 %, 7,14 % ± 0,11 % ir 9,88 % ± 0,20 %.

Ag nusodinimas ant TiO_2 paviršiaus pagerino plėvelių tipo LDPE fotokatalitinę degradaciją. Taip pat buvo pastebėta, kad didesnė Ag koncentracija Ag-TiO_2 nanomedžiagose pagerina TiO_2 fotokatalitinį aktyvumą. Pavyzdžiui, naudojant Ag-$TiO_2$3 katalizatorių, juodų LDPE plėvelių (1×1 mm) masės netekimas buvo 4,5 karto didesnis nei naudojant grynas TiO_2 NDs ir dvigubai didesnis nei naudojant Ag-$TiO_2$0.5.

LDPE plėvelių fotokatalitinė degradacija naudojant visus keturis katalizatorius atitiko pseudo pirmo laipsnio kinetinį modelį. Tai patvirtina aukštos determinacijos koeficiento vertės (R^2), kurios svyravo nuo 0,972 iki 0,998 (*27 pav., 13 lentelė*). Reakcijos greičio konstanta (k) padidėjo, didinat Ag kiekį Ag-TiO_2 nanomedžiagose. Didžiausios k vertės buvo nustatytos degraduojant juodas LDPE plėveles (1×1 mm): $2{,}64 \cdot 10^{-2}$ min^{-1} su TiO_2, $4{,}10 \cdot 10^{-2}$ min^{-1} su Ag-$TiO_2$0.5, $5{,}91 \cdot 10^{-2}$ min^{-1} su Ag-$TiO_2$1, ir $1{,}00 \cdot 10^{-1}$ min^{-1} su Ag-$TiO_2$3. Apskaičiuotos k vertės atitiko eksperimentinių tyrimų metu nustatytą katalizatorių efektyvumo eiliškumą.

Morfologiniai juodų LDPE plėvelių (1×1 mm) pokyčiai buvo nustatyti atlikus SEM vaizdinimą po 60 min, 480 min ir 960 min fotokatalitinės degradacijos naudojant Ag-$TiO_2$3 (*28 pav.*). Po 60 min fotokatalitinės degradacijos juodų LDPE plėvelių (1×1 mm) paviršius išliko beveik nepakitęs, tačiau po 480 min ir 960 min atsirado reikšmingi struktūriniai paviršiaus pokyčiai, tokie kaip raukšlės, padidėjęs paviršiaus šiurkštumas, mikroįtrūkimai, gilios ertmės. Raukšlių ir įtrūkimų formavimasis plėvelių paviršiuje yra itin svarbus, nes tai leidžia vandens molekulėms prasiskverbti į amorfinę polimero sritį ir inicijuoja tolesnius degradacijos procesus (Kamalian ir kt., 2020).

Plėvelės tipo LDPE fizikinių savybių įtaka fotokatalitinės degradacijos efektyvumui

Fizikinių LDPE plėvelių savybių įtaka fotokatalitinės degradacijos efektyvumui buvo analizuojama atsižvelgiant į plėvelių spalvą (juodos ir permatomos) ir dydį (1×1 mm ir 3×3 mm) (*30 pav.*). Po 480 min ir 960 min fotokatalitinės degradacijos naudojant Ag-$TiO_2$3 buvo nustatyta, jog juodos LDPE plėvelės atitinkamai degraduojamos pusantro ir du kartus efektyviau nei permatomos LDPE plėvelės. Lyginant juodas ir permatomas LDPE plėveles yra svarbu atkreipti dėmesį į jų sudėtyje aptiktus neorganinius

elementus. XRF analizės metu buvo nustatyta, kad permatomoms plėvelėms yra būdingas aukštas polimero grynumas, kai tuo tarpu juodos LDPE plėvelės pasižymėjo santykinai dideliu kiekiu neorganinių elementų. Juodose LDPE plėvelėse esantys priedai gali turėti įtakos polimero stabilumui ir reaktyvumui. Pavyzdžiui, tokie priedai kaip Ca, Al, Mg ir Si padidina juodų LDPE plėvelių paviršiaus šiurkštumą ir nelygumus, taip padidinant bendrą paviršiaus plotą ir sąveiką su katalizatoriumi. Be to, efektyvesnė fotokatalitinė juodų LDPE plėvelių degradacija yra siejama ir su šių plėvelių gebėjimų sugerti daugiau šviesos. Didesnė juodų LDPE plėvelių šviesos sugertis padidina temperatūrą plėvelių paviršiuje, o tai pagreitina fotocheminius procesus (Reinicker, 2018).

Palyginus skirtingų dydžių (1×1 mm ir 3×3 mm) LDPE plėvelių masės netekimą, paaiškėjo, kad mažesnės LDPE plėvelės degraduoja efektyviau. Po 480 min ir 960 min, LDPE plėvelių (1×1 mm) masės netekimas buvo pusantro karto didesnis nei LDPE plėvelių, kurių dydis siekė 3×3 mm. Didesnis mažesnių LDPE plėvelių degradacijos efektyvumas yra siejamas su joms būdingu didesniu paviršiaus ploto ir tūrio santykiu, kuris pagerina sąveiką su katalizatoriumi ir ROS. Taip pat buvo aptikta, kad mažesnio dydžio mikroplastiko plėvelės yra tolygiau pasiskirsčiusios reakcijos sistemoje, o tai užtikrina ne tik geresnę sąveiką su katalizatoriumi, bet ir su šviesos šaltiniu. Efektyvesnė mažesnių mikroplastiko dalelių degradacija buvo pastebėta ir ankstesniuose tyrimuose. Pavyzdžiui, Llorente-García ir kt. (2020) nustatė, kad mažesnio dydžio (382 ± 154 μm) mikrogranulių fotokatalitinė degradacija buvo efektyvesnė 21 kartą už didesnio dydžio (814 ± 91 μm) mikrogranulių degradaciją.

Paviršiaus morfologijos pokyčiai tarp skirtingų fizikinių savybių LDPE plėvelių taip pat buvo nustatyti po 960 min fotokatalitinės degradacijos, naudojant Ag-$TiO_2$3 (*31 pav.*). Juodų LDPE plėvelių (1×1 mm) SEM analizė parodė, kad jų paviršiuje įvyko ryškiausi pokyčiai: susiformavo gilūs įtrūkimai ir ertmės. Šie pokyčiai rodo, kad plėvelės pažeidimai perėjo ir į gilesnius sluoksnius ir yra siejami su organinių medžiagų išgaravimu ir polimerinės grandinės skilimu (Ali ir kt., 2016; Sura ir Nain, 2024). Skirtingai nuo juodų LDPE plėvelių, permatomos LDPE plėvelės (1×1 mm) parodė žymiai mažiau paviršiaus pažeidimų. Šių LDPE plėvelių paviršius iš esmės išliko lygus ir homogeniškas. Nors tam tikri pakitimai, tokie kaip raukšlės ir mikroįtrūkimai buvo užfiksuoti ir permatomų LDPE plėvelių paviršiuje, jie buvo randami tik ribotose paviršiaus srityse ir neperėjo į gilesnius plėvelės sluoksnius. Mažesnės LDPE plėvelės (1×1 mm), lyginant su didesnėmis (3×3 mm), patyrė ryškesnius paviršiaus pažeidimus, tai siejama su geresniu mažesnių dalelių pasiskirstymu reakcijos tirpale ir efektyvesne sąveika su katalizatoriumi ir UV spinduliuote.

Plėvelių tipo LDPE FTIR spektroskopinė analizė

Po 960 min fotokatalitinės degradacijos juodose LDPE plėvelėse buvo aptiktos naujai susiformavusios absorbcijos juostos (*32 pav.*), kurios yra siejamos su oksidaciniais polimerinės grandinės pažeidimais. Smailės ties ~1740 cm^{-1} ir ~1654 cm^{-1} yra priskiriamos C=O grupių formavimuisi. Naujai susidariusi absorbcijos juosta ties 980–1158 cm^{-1} yra būdinga peroksido (C–O) tempimo virpesiams, o absorbcijos juosta srityje ties 3220–3620 cm^{-1} rodo hidroperoksido ir alkoholio funkcinių grupių formavimąsi. Po 960 min permatomos LDPE plėvelės pasižymėjo panašiais funkcinių grupių pokyčiais kaip ir juodos LDPE plėvelės. Plėvelių dydis taip pat turėjo įtakos fotokatalitinės degradacijos efektyvumui. Intensyvesnės C=O grupėms būdingos smailės buvo aptiktos LDPE plėvelėse, kurių dydis siekė 1×1 mm nei LDPE plėvelėse, kurių dydis buvo 3×3 mm. Tai siejama su efektyviau vykstančiais foto-oksidaciniais procesais mažesnio dydžio LDPE plėvelėse.

Visų LDPE plėvelių CI ir VI vertės padidėjo, ilginant degradacijos trukmę nuo 60 min iki 960 min (*15 lentelė*). Juodos LDPE plėvelės parodė didesnes CI ir VI vertes nei permatomos LDPE plėvelės. Didžiausia CI vertė buvo nustatyta degraduojant juodas LDPE plėveles, kurių dydis siekė 1×1 mm (CI = 0,93 ± 0,09, VI = 0,49 ± 0,04). Tuo tarpu mažesnio dydžio permatomų LDPE plėvelių CI ir VI vertės atitinkamai buvo 0,68 ± 0,04 ir 0,34 ± 0,03. Gauti rezultatai leidžia teigti, kad net nedideli skirtumai tarp LDPE fizikinių savybių gali daryti reikšmingą įtaką fotokatalitinės degradacijos efektyvumui.

ROS susidarymas fotokatalitinės degradacijos metu

ROS slopinimo tyrimai buvo atlikti siekiant nustatyti pagrindines ROS, inicijuojančias LDPE plėvelių fotokatalitinę degradaciją (*34 pav.*). Pridėjus IPA į reakcijos sistemą, kurioje Ag-$TiO_2$3 buvo naudojamas kaip katalizatorius, juodų LDPE plėvelių (1×1 mm) masės netekimas sumažėjo nuo 4,57 % iki 1,76 %, o permatomų LDPE plėvelių (1×1 mm) – nuo 3,67 % iki 1,68 %. LDPE plėvelių masės netekimo sumažėjimai naudojant IPA buvo ženkliai didesnis nei naudojant AA arba AO. Šie rezultatai rodo, kad *·OH* yra pagrindinės ROS, inicijuojančios ir kontroliuojančios foto-oksidacinius procesus LDPE polimerinėje grandinėje. Į reakcijos mišinį pridėjus AA, juodų LDPE plėvelių (1×1 mm) masės netekimas sumažėjo nuo 4,57 % iki 3,09 %, o to paties dydžio permatomų LDPE plėvelių – nuo 3,68 % iki 2,62 %. Nors $O_2^{\cdot-}$ prisideda prie LDPE degradacijos procesų, tačiau jų poveikis yra mažesnis nei *·OH*. Kai reakcijos sistemoje buvo naudojamas AO, LDPE plėvelių masės

netekimo sumažėjime pastebėti tik nežymūs pokyčiai, o tai rodo, kad h^+ mažiau prisideda prie LDPE degradacijos nei $\cdot OH$ ir $O_2^{\cdot -}$.

Skyrelio išvados

Ag nusodinimas ant TiO_2 paviršiaus pagerino plėvelės tipo LDPE mikroplastiko fotokatalitinės degradacijos efektyvumą. Didinant Ag kiekį Ag-TiO_2 nanomedžiagoje, draustinės juostos tarpo energija sumažėjo nuo 3,2 eV (TiO_2 NDs) iki 2,76 eV (Ag-$TiO_2$3). Didžiausias tirtų LDPE plėvelių masės netekimas siekė 9,88 % juodoms LDPE plėvelėms (1×1 mm), naudojant Ag-$TiO_2$3. Tuo tarpu, permatomų LDPE plėvelių didžiausias masės netekimas siekė 4,85 %. FTIR analizė taip pat patvirtino sėkmingą LDPE plėvelių fotokatalitinę degradaciją. Aukščiausios CI (0,93) ir VI (0,49) vertės buvo nustatytos degraduojant juodos spalvos LDPE plėveles (1×1 mm), naudojant Ag-$TiO_2$3.

Tyrimo rezultatai parodė, kad fizikinės savybės, tokios kaip dydis ir spalva, yra svarbūs veiksniai, kurie gali nulemti LDPE plėvelių fotokatalitinės degradacijos efektyvumą. Mažesnės LDPE plėvelės (1×1 mm) pasižymėjo pusantro karto didesniu masės netekimu nei didesnės LDPE plėvelės (3×3 mm). Tai siejama su mažesnių plėvelių didesniu paviršiaus ploto ir tūrio santykiu bei geresniu pasiskirstymu reakcijos mišinyje, lyginant su didesnėmis plėvelėmis. SEM vaizdinimo rezultatai parodė, reikšmingus struktūrinius skirtumus tarp tirtų LDPE plėvelių. Po 960 min degradacijos juodos plėvelės pasižymėjo ryškiais morfologiniais pokyčiais, tokiais kaip paviršiaus šiurkštumo padidėjimas ir gilių įtrūkimų bei ertmių formavimasis, kai tuo tarpu permatomos LDPE plėvelės parodė tik nežymius paviršiaus pažeidimus. ROS susidarymo tyrimai parodė, jog $\cdot OH$ ir $O_2^{\cdot -}$ yra pagrindinės ROS, inicijuojančios LDPE plėvelių foto-oksidacinius procesus.

IŠVADOS

1. Modifikuotos TiO_2 NDs pasižymėjo geresniu fotokatalitiniu aktyvumu nei grynos TiO_2 NDs. Didžiausias LDPE masės sumažėjimas esant neutralioms reakcijos sąlygoms buvo nustatytas, naudojant TiO_2-Kao nanokompozitus ir siekė 28,36 %. Prie TiO_2 NDs prijungus Ag NDs, juodų LDPE plėvelių (1x1 mm) masės netekimas išaugo nuo 3,08 % (naudojant TiO_2) iki 9,88 % (naudojant Ag-$TiO_2$3).

2. Didžiausias LDPE degradacijos efektyvumas buvo nustatytas rūgštinėje terpėje esant pH 3 ir siekė 30,96 % po 60 min fotokatalitinės degradacijos, naudojant TiO_2-Kao. Pritaikius LDPE ir katalizatoriaus santykį 1:2, LDPE masės netekimas padidėjo ~ 10 % su visais tirtais katalizatoriais, aukščiausia LDPE masės netekimo vertė po 60 min fotokatalitinės degradacijos siekė 25,98 % (TiO_2-Kao). Tirpalo joninės jėgos padidinimas iki 0,5 $molL^{-1}$, sumažino LDPE masės netekimą nuo 17,08 % iki 7,82 %, priklausomai nuo naudoto katalizatoriaus.

3. Naudojant Ag-$TiO_2$3 katalizatorių, juodų LDPE plėvelių (1×1 mm) fotokatalitinės degradacijos efektyvumas po 960 min fotokatalitinės degradacijos buvo dvigubai didesnis ir siekė 9,88 % nei to paties dydžio permatomų LDPE plėvelių, kurių degradacijos efektyvumas siekė 4,85 %. Sumažinus plėvelių matmenis nuo 3×3 mm iki 1×1 mm, LDPE degradacijos efektyvumas padidėjo nuo 6,19 % iki 9,88 % juodoms LDPE plėvelėms, ir nuo 2,94% iki 4,85% permatomoms LDPE plėvelėms.

4. Po fotokatalitinės degradacijos LDPE polimere užfiksuoti ryškūs funkcinių grupių pokyčiai. Aptiktos naujai susiformavusios deguonies turinčios funkcinės grupės, indikuojančios: esterius (1740 cm^{-1}), aldehidus (2634 cm^{-1} ir 1654 cm^{-1}), ketonus (1700–1850 cm^{-1}) ir nesotieji vinilo grupių ryšiai (873 cm^{-1}). Didžiausios karbonilo indekso vertės buvo pasiektos, naudojant TiO_2-Kao ir Ag-$TiO_2$3, atitinkamai 1,41 (fragmentinio tipo LDPE) ir 0,93 (juodose plėvelės tipo LDPE (1×1 mm)). Didžiausia vinilo indekso vertė (VI = 0,49) buvo nustatyta juodose LDPE plėvelėse (1×1 mm), patvirtinanti intensyvų polimero grandinių skilimą.

5. Hidroksilo radikalai (·*OH*) buvo nustatyti kaip dominuojančios ROS, kurios inicijuoja LDPE degradaciją. Hidroksilo radikalų slopinimo poveikis sumažino masės praradimo nuostolį nuo 4,57 % iki 1,76 % juoduose LDPE plėvelėse (1×1 mm) ir nuo 3,68 % iki 1,68 % permatomose LDPE plėvelėse (1×1 mm). TiO_2 paviršiaus padengimas Ag NDs sustiprino superoksido radikalų įtaką degradacijos efektyvumui. Superoksido radikalai ($O_2^{\cdot-}$) veikė kaip papildomi veiksniai, sumažindami masės praradimo nuostolį nuo 4,57 % iki 3,09 % juodose LDPE plėvelėse (1×1 mm) ir nuo 3,68% iki 2,62 % permatomose LDPE plėvelėse (1×1 mm).

ACKNOWLEDGEMENTS

I would like to express my deepest gratitude to my scientific supervisors, Dr. Ieva Uogintė and Dr. Steigvilė Byčenkienė, for their guidance and constant support throughout this journey. I am especially thankful for their trust and for fostering an environment that encouraged independent thinking and taught me to approach scientific questions from multiple perspectives. I am truly grateful for the opportunity to learn, grow, and develop as a researcher.

I am sincerely thankful to my colleagues in the Department of Environmental Research for creating a supportive and collaborative research environment. I would like to express my gratitude to PhD student Austėja Burbulytė, Tomas Stonkus, Dr. Mehri Davtalab, Dr. Sergej Šemčuk, Dr. Daria Pashneva, Dr. Abdullah Khan, Dr. Kristina Plauškaitė-Šukienė, Dr. Lina Davulienė, and Jonas Didžbalis for their kindness, support, advice, and many thoughtful discussions. I would especially like to thank my former colleagues, Dr. Raman Novikau for generously sharing his expertise in the design of experiments, as well as for his guidance and patience throughout this research, and to Dr. Dalia Jasinevičienė for sharing her expertise in environmental chemistry and providing access to laboratory equipment.

I am sincerely thankful to colleagues from the Department of Characterization of Materials Structure, Dr. Aušra Selskienė, Dr. Raimondas Giraitis, Dr. Sandra Stanionytė, and Dr. Martynas Skapas, for their assistance with the characterization of nanomaterials and plastic films. I greatly appreciate their valuable contributions to our joint publications, as well as their dedication and willingness to share their expertise.

Beyond the scientific team, I am deeply grateful to my family and friends for their unconditional support, love, patience, and encouragement. My special thanks go to my friends Karolina Jocytė, Karolina Karalevičiūtė, Agnė Kšanauskaitė, Agnė Minderytė, Audrė Kalinauskaitė, Kamilė Kvedaravičienė, Giedrė Čepurnaitė, Justė Tulaitė, Andžej Dovda, and Valdas Viluckis. Your support, empathy, curiosity, and understanding have been a constant source of strength.

Finally, I wish to sincerely thank my partner Martynas Arlauskas, for the most selfless, kind, and inspiring friendship I could ever have dreamt of. Thank you for celebrating my milestones and supporting me through challenges and setbacks along the way. This journey has shaped my world in many ways, and I could not be more grateful to have you in it.

AI STATEMENT

The author declared that generative AI was used in the writing of this dissertation. Generative AI tools (ChatGPT (OpenAI), GPT-5.5 and Grammarly Pro) were used only for language editing, grammar refinement, and text clarity during dissertation preparation. The tool was not used to generate scientific content, perform analyses, or interpret data. All scientific conclusions were developed by the author.

REFERENCES

Abbas, G., Ahmed, U., & Ahmad, M. A. (2025). Impact of Microplastics on Human Health: Risks, Diseases, and Affected Body Systems. In *Microplastics* (Vol. 4, Number 2). Multidisciplinary Digital Publishing Institute (MDPI). https://doi.org/10.3390/microplastics4020023

Abdel-Khalek, A. A., Mahmoud, S. A., & Zaki, A. H. (2018). Visible light assisted photocatalytic degradation of crystal violet, bromophenol blue and eosin Y dyes using AgBr-ZnO nanocomposite. *Environmental Nanotechnology, Monitoring and Management*, *9*, 164–173. https://doi.org/10.1016/j.enmm.2018.03.002

Ahmed, M. A., Mahmoud, S. A., & Mohamed, A. A. (2025). Interfacially engineered metal oxide nanocomposites for enhanced photocatalytic degradation of pollutants and energy applications. In *RSC Advances* (Vol. 15, Number 20, pp. 15561–15603). Royal Society of Chemistry. https://doi.org/10.1039/d4ra08780a

Ainali, N. M., Bikiaris, D. N., & Lambropoulou, D. A. (2021). Aging effects on low- and high-density polyethylene, polypropylene and polystyrene under UV irradiation: An insight into decomposition mechanism by Py-GC/MS for microplastic analysis. *Journal of Analytical and Applied Pyrolysis*, *158*. https://doi.org/10.1016/j.jaap.2021.105207

Ali, S. S., Qazi, I. A., Arshad, M., Khan, Z., Voice, T. C., & Mehmood, C. T. (2016). Photocatalytic degradation of low density polyethylene (LDPE) films using titania nanotubes. *Environmental Nanotechnology, Monitoring and Management*, *5*, 44–53. https://doi.org/10.1016/j.enmm.2016.01.001

Almond, J., Sugumaar, P., Wenzel, M. N., Hill, G., & Wallis, C. (2020). Determination of the carbonyl index of polyethylene and polypropylene using specified area under band methodology with ATR-FTIR spectroscopy. *E-Polymers*, *20*(1), 369–381. https://doi.org/10.1515/epoly-2020-0041

Alvarado, J. A., Gonzalez, G. S. A., & Cao, G. (2024). Rapid and efficient mineralization of methylene blue dye (above 95 % in 20 min) catalyzed by ZnO nanoparticles under sunlight. *Materials Today Sustainability*, *27*. https://doi.org/10.1016/j.mtsust.2024.100883

Andrady, A. L. (2017). The plastic in microplastics: A review. In *Marine Pollution Bulletin* (Vol. 119, Number 1, pp. 12–22). Elsevier Ltd. https://doi.org/10.1016/j.marpolbul.2017.01.082

Aniśko-Michalak, J., Sokolohorskyj, A., Szafraniak-Wiza, I., Kosmela, P., Piasecki, A., & Barczewski, M. (2025). Unveiling the Effects of Thermal Aging on the Oxidative Stability of Biobased Low-Density Polyethylenes. *ACS Omega*, *10*(24), 25432–25450. https://doi.org/10.1021/acsomega.5c00636

Ariza-Tarazona, M. C., Villarreal-Chiu, J. F., Barbieri, V., Siligardi, C., & Cedillo-González, E. I. (2019). New strategy for microplastic degradation: Green photocatalysis using a protein-based porous N-TiO 2 semiconductor. *Ceramics International*, *45*(7), 9618–9624. https://doi.org/10.1016/j.ceramint.2018.10.208

Ariza-Tarazona, M. C., Villarreal-Chiu, J. F., Hernández-López, J. M., Rivera De la Rosa, J., Barbieri, V., Siligardi, C., & Cedillo-González, E. I. (2020). Microplastic pollution reduction by a carbon and nitrogen-doped TiO2: Effect of pH and temperature in the photocatalytic degradation process. *Journal of Hazardous Materials*, *395*. https://doi.org/10.1016/j.jhazmat.2020.122632

Armaković, S. J., Savanović, M. M., & Armaković, S. (2023). Titanium Dioxide as the Most Used Photocatalyst for Water Purification: An Overview. In *Catalysts* (Vol. 13, Number 1). MDPI. https://doi.org/10.3390/catal13010026

Asghar, W., Qazi, I. A., Ilyas, H., Khan, A. A., Awan, M. A., & Rizwan Aslam, M. (2011). Comparative solid phase photocatalytic degradation of polythene films with doped and undoped TiO2 nanoparticles. *Journal of Nanomaterials*, *2011*. https://doi.org/10.1155/2011/461930

Ayankunle, A. Y., Buhhalko, N., Pachel, K., Lember, E., Drenkova-Tuhtan, A., & Heinlaan, M. (2025). Microplastics in Estonian wastewater treatment plants: First evaluation of baseline concentrations and stage-wise removal efficiency. *Aquatic Toxicology*, *281*. https://doi.org/10.1016/j.aquatox.2025.107305

Azmi, A., Sata, S. A., Rohman, F. S., & Aziz, N. (2019). Melt flow index of low-density polyethylene determination based on molecular weight and branching properties. *Journal of Physics: Conference Series*, *1349*(1). https://doi.org/10.1088/1742-6596/1349/1/012094

Barbosa, L. V., Marçal, L., Nassar, E. J., Calefi, P. S., Vicente, M. A., Trujillano, R., Rives, V., Gil, A., Korili, S. A., Ciuffi, K. J., & De Faria, E. H. (2015). Kaolinite-titanium oxide nanocomposites prepared via sol-gel as heterogeneous photocatalysts for dyes degradation. *Catalysis Today*, *246*, 133–142. https://doi.org/10.1016/j.cattod.2014.09.019

Behera, A. K., Shadangi, K. P., & Sarangi, P. K. (2022). Synthesis of dye-sensitized TiO2/Ag doped nano-composites using UV photoreduction process for phenol degradation: A comparative study. *Environmental Pollution*, *312*. https://doi.org/10.1016/j.envpol.2022.120019

Belbel, A., Draoui, A., & Cheraif, K. (2024). ZR-PILLARED MONTMORILLONITE CLAY AS HOST TO IONIC LIQUIDS FROM AQUEOUS SOLUTIONS. *Revue Roumaine de Chimie*, *69*(10–12), 565–571. https://doi.org/10.33224/rrch.2024.69.10-12.05

Calabrese, C., Maertens, A., Piras, A., Aprile, C., & Liotta, L. F. (2023). Novel Sol-Gel Synthesis of TiO2 Spherical Porous Nanoparticles Assemblies with Photocatalytic Activity. *Nanomaterials*, *13*(13). https://doi.org/10.3390/nano13131928

Camacho-González, M. A., Hernández-Reyes, A., Garrido-Hernández, A., Olivares-Xometl, O., Likhanova, N. V., & Lijanova, I. V. (2025). TPA and PET Photo-Degradation by Heterogeneous Catalysis Using a (Al2O3)0.75TiO2 Coating. *Surfaces*, *8*(2). https://doi.org/10.3390/surfaces8020034

Cao, Z., Wang, Q., & Cheng, H. (2021). Recent advances in kaolinite-based material for photocatalysts. *Chinese Chemical Letters*, *32*(9), 2617–2628. https://doi.org/10.1016/j.cclet.2021.01.009

Carrieri, E., Motte, J., Nachtergaele, P., Mertens, I., Hoogenboom, R., Dewulf, J., & De Meester, S. (2025). Development of a solvent based recycling process for agricultural film. *Resources, Conservation and Recycling*, *212*. https://doi.org/10.1016/j.resconrec.2024.107981

Chanani, J., Buazar, F., & Nikpour, Y. (2023). Promoted Photocatalytic Activity of Green Titanium Oxide-Clay Nanocomposite Toward Polychlorinated Biphenyl Degradation in Actual Samples. *Water, Air, and Soil Pollution*, *234*(6). https://doi.org/10.1007/s11270-023-06356-y

Chen, D., Cheng, Y., Zhou, N., Chen, P., Wang, Y., Li, K., Huo, S., Cheng, P., Peng, P., Zhang, R., Wang, L., Liu, H., Liu, Y., & Ruan, R. (2020). Photocatalytic degradation of organic pollutants using TiO2-based photocatalysts: A review. In *Journal of Cleaner Production* (Vol. 268). Elsevier Ltd. https://doi.org/10.1016/j.jclepro.2020.121725

Chen, J., Wu, J., Sherrell, P. C., Chen, J., Wang, H., Zhang, W. xian, & Yang, J. (2022). How to Build a Microplastics-Free Environment: Strategies for Microplastics Degradation and Plastics Recycling. In *Advanced Science* (Vol. 9, Number 6). John Wiley and Sons Inc. https://doi.org/10.1002/advs.202103764

Commission Regulation (EU) 2023/2055. (2023). *Commission Regulation (EU) 2023/2055 of 25 September 2023 amending Annex XVII to Regulation (EC) No 1907/2006 (REACH)*. https://eur-lex.europa.eu/eli/reg/2023/2055/oj

da Silva, M. R. C., Andrade Neto, J. da S., Walkley, B., & Kirchheim, A. P. (2024). Effects of kaolinite and montmorillonite calcined clays on the sulfate balance, early hydration, and artificial pore solution of limestone calcined clay cements (LC3). *Materials and Structures/Materiaux et Constructions*, *57*(8). https://doi.org/10.1617/s11527-024-02462-3

Deng, Y., Zhang, Y., Lemos, B., & Ren, H. (2017). Tissue accumulation of microplastics in mice and biomarker responses suggest widespread health risks of exposure. *Scientific Reports*, *7*. https://doi.org/10.1038/srep46687

Ding, L., Yu, X., Guo, X., Zhang, Y., Ouyang, Z., Liu, P., Zhang, C., Wang, T., Jia, H., & Zhu, L. (2022). The photodegradation processes and mechanisms of polyvinyl chloride and polyethylene terephthalate microplastic in aquatic environments: Important role of clay minerals. *Water Research*, *208*. https://doi.org/10.1016/j.watres.2021.117879

Directive (EU) 2019/904. (2019). *Directive (EU) 2019/904 on the reduction of the impact of certain plastic products on the environment*. https://eur-lex.europa.eu/eli/dir/2019/904/oj

Doğan, M. (2021). Ultraviolet light accelerates the degradation of polyethylene plastics. *Microscopy Research and Technique*, *84*(11), 2774–2783. https://doi.org/10.1002/jemt.23838

Doi, A., Ejtemaei, M., & Nguyen, A. V. (2019). Effects of ion specificity on the surface electrical properties of kaolinite and montmorillonite. *Minerals Engineering*, *143*. https://doi.org/10.1016/j.mineng.2019.105929

Dong, P., Yang, F., Cheng, X., Huang, Z., Nie, X., Xiao, Y., & Zhang, X. (2019). Plasmon enhanced photocatalytic and antimicrobial activities of Ag-TiO 2

nanocomposites under visible light irradiation prepared by DBD cold plasma treatment. *Materials Science and Engineering C*, *96*, 197–204. https://doi.org/10.1016/j.msec.2018.11.005

El Mchaouri, M., Mallah, S., Abouhajjoub, D., Boumya, W., Elmoubarki, R., Essadki, A., Barka, N., & Elhalil, A. (2025). Engineering TiO2 photocatalysts for enhanced visible-light activity in wastewater treatment applications. In *Tetrahedron Green Chem* (Vol. 6). Elsevier Ltd. https://doi.org/10.1016/j.tgchem.2025.100084

El-Zohry, A. M., Kloo, L., & He, L. (2024). Understanding Charge Dynamics in TiO2 Using Ultrafast Mid-infrared Spectroscopy: Trapping versus Recombination. *Journal of Physical Chemistry C*, *128*(10), 4192–4199. https://doi.org/10.1021/acs.jpcc.3c07155

European Parliament and Council of the European Union. (2024). *Directive (EU) 2024/3019 on urban wastewater treatment*. https://eur-lex.europa.eu/eli/dir/2024/3019/oj

Fairbrother, A., Hsueh, H. C., Kim, J. H., Jacobs, D., Perry, L., Goodwin, D., White, C., Watson, S., & Sung, L. P. (2019). Temperature and light intensity effects on photodegradation of high-density polyethylene. *Polymer Degradation and Stability*, *165*, 153–160. https://doi.org/10.1016/j.polymdegradstab.2019.05.002

Fayshal, M. A. (2024). Current practices of plastic waste management, environmental impacts, and potential alternatives for reducing pollution and improving management. In *Heliyon* (Vol. 10, Number 23). Elsevier Ltd. https://doi.org/10.1016/j.heliyon.2024.e40838

Gao, P., Liu, X., Guo, Z., & Tournassat, C. (2023). Acid-Base Properties of Cis-Vacant Montmorillonite Edge Surfaces: A Combined First-Principles Molecular Dynamics and Surface Complexation Modeling Approach. *Environmental Science and Technology*, *57*(3), 1342–1352. https://doi.org/10.1021/acs.est.2c07171

Gardette, M., Perthue, A., Gardette, J. L., Janecska, T., Földes, E., Pukánszky, B., & Therias, S. (2013). Photo- and thermal-oxidation of polyethylene: Comparison of mechanisms and influence of unsaturation content. *Polymer Degradation and Stability*, *98*(11), 2383–2390. https://doi.org/10.1016/j.polymdegradstab.2013.07.017

Garnai Hirsch, S., Barel, B., & Segal, E. (2019). Characterization of surface phenomena: probing early stage degradation of low-density polyethylene films. *Polymer Engineering and Science*, *59*, E129–E137. https://doi.org/10.1002/pen.24886

Ge, J., Zhang, Z., Ouyang, Z., Shang, M., Liu, P., Li, H., & Guo, X. (2022). Photocatalytic degradation of (micro)plastics using TiO2-based and other catalysts: Properties, influencing factor, and mechanism. *Environmental Research*, *209*. https://doi.org/10.1016/j.envres.2022.112729

Geyer, R., Jambeck, J. R., & Law, K. L. (2017). Production, use, and fate of all plastics ever made. *Science Advances*, *3*(7). https://doi.org/10.1126/sciadv.1700782

Ghamarpoor, R., Fallah, A., & Jamshidi, M. (2023). Investigating the use of titanium dioxide (TiO2) nanoparticles on the amount of protection against UV irradiation. *Scientific Reports*, *13*(1). https://doi.org/10.1038/s41598-023-37057-5

Ghanadi, M., & Padhye, L. P. (2024). Revealing the long-term impact of photodegradation and fragmentation on HDPE in the marine environment: Origins of microplastics and dissolved organics. *Journal of Hazardous Materials*, *465*. https://doi.org/10.1016/j.jhazmat.2024.133509

Gong, Z., Jin, L., Yu, X., Wang, B., Hu, S., Ruan, H., Sung, Y. J., Lee, H. G., & Jin, F. (2023). Biodegradation of Low Density Polyethylene by the Fungus Cladosporium sp. Recovered from a Landfill Site. *Journal of Fungi*, *9*(6). https://doi.org/10.3390/jof9060605

González-Pleiter, M., Edo, C., Aguilera, Á., Viúdez-Moreiras, D., Pulido-Reyes, G., González-Toril, E., Osuna, S., de Diego-Castilla, G., Leganés, F., Fernández-Piñas, F., & Rosal, R. (2021). Occurrence and transport of microplastics sampled within and above the planetary boundary layer. *Science of the Total Environment*, *761*. https://doi.org/10.1016/j.scitotenv.2020.143213

Goutham, C., Ashok Kumar, K. V., Kumar Raavi, S. S., Subrahmanyam, C., & Asthana, S. (2022). Enhanced electrical and photocatalytic activities in Na0.5Bi0.5TiO3 through structural modulation by using anatase and rutile phases of TiO2. *Journal of Materiomics*, *8*(1), 18–29. https://doi.org/10.1016/j.jmat.2021.06.003

Guo, G., Yu, B., Yu, P., & Chen, X. (2009). Synthesis and photocatalytic applications of Ag/TiO2-nanotubes. *Talanta*, *79*(3), 570–575. https://doi.org/10.1016/j.talanta.2009.04.036

Guo, M., Noori, R., & Abolfathi, S. (2024). Microplastics in freshwater systems: Dynamic behaviour and transport processes. In *Resources, Conservation and Recycling* (Vol. 205). Elsevier B.V. https://doi.org/10.1016/j.resconrec.2024.107578

He, Y., Rehman, A. U., Xu, M., Not, C. A., Ng, A. M. C., & Djurišić, A. B. (2023). Photocatalytic degradation of different types of microplastics by TiOx/ZnO tetrapod photocatalysts. *Heliyon*, *9*(11). https://doi.org/10.1016/j.heliyon.2023.e22562

HELCOM. (2021). *Baltic Sea Action Plan 2021*. https://helcom.fi/wp-content/uploads/2021/10/Baltic-Sea-Action-Plan-2021-update.pdf

Huang, Q., Li, J., Wei, W., Wu, Y., & Li, T. (2017). Synthesis, characterization and application of TiO2/Ag recyclable SERS substrates. *RSC Advances*, *7*(43), 26704–26709. https://doi.org/10.1039/c7ra03112b

Huang, Y., Liu, Q., Jia, W., Yan, C., & Wang, J. (2020). Agricultural plastic mulching as a source of microplastics in the terrestrial environment. *Environmental Pollution*, *260*, 114096. https://doi.org/10.1016/j.envpol.2020.114096

Huang, Z., Bu, J., & Wang, H. (2022). Application of two modified kaolin materials in removing micro-plastics from water. *Journal of Material Cycles and Waste Management*, *24*(4), 1460–1475. https://doi.org/10.1007/s10163-022-01393-x

Iftikhar, A., Qaiser, Z., Sarfraz, W., Ejaz, U., Aqeel, M., Rizvi, Z. F., & Khalid, N. (2024). Understanding the leaching of plastic additives and subsequent risks to

ecosystems. In *Water Emerging Contaminants and Nanoplastics* (Vol. 3, Number 1). OAE Publishing Inc. https://doi.org/10.20517/wecn.2023.58

ISO 24187:2023. (2023). *ISO 24187:2023 - Principles for the analysis of microplastics present in the environment*. https://www.iso.org/standard/78033.html

Jadhav, V., Patil, M., Pardeshi, S., Suryavanshi, H., & Bhagare, A. (2025). Green synthesis of Ag@TiO2 nanomaterials using Achyranthes aspera leaf extract for sustainable photocatalytic degradation of dyes. *Discover Applied Sciences*, *7*(7). https://doi.org/10.1007/s42452-025-07324-3

Jia, T., Liang, X., Zhao, K., Guo, Q., Zhang, Y., Zeng, L., Yang, L., Othman, S. I., Allam, A. A., Rudayni, H. A., & Wang, C. (2024). Exploring the photocatalytic degradation mechanism for low-density polyethylene utilizing Bi4Ti3O12 nanoflower catalyst. *Journal of Environmental Chemical Engineering*, *12*(5). https://doi.org/10.1016/j.jece.2024.113482

Jiang, S., Yin, M., Ren, H., Qin, Y., Wang, W., Wang, Q., & Li, X. (2023). Novel CuMgAlTi-LDH Photocatalyst for Efficient Degradation of Microplastics under Visible Light Irradiation. *Polymers*, *15*(10). https://doi.org/10.3390/polym15102347

Jung, H. Y., Yeo, I. S., Kim, T. U., Ki, H. C., & Gu, H. B. (2018). Surface plasmon resonance effect of silver nanoparticles on a TiO 2 electrode for dye-sensitized solar cells. *Applied Surface Science*, *432*, 266–271. https://doi.org/10.1016/j.apsusc.2017.04.237

Jung, M. R., Horgen, F. D., Orski, S. V., Rodriguez C., V., Beers, K. L., Balazs, G. H., Jones, T. T., Work, T. M., Brignac, K. C., Royer, S. J., Hyrenbach, K. D., Jensen, B. A., & Lynch, J. M. (2018). Validation of ATR FT-IR to identify polymers of plastic marine debris, including those ingested by marine organisms. *Marine Pollution Bulletin*, *127*, 704–716. https://doi.org/10.1016/j.marpolbul.2017.12.061

Jung, W., Yang, M. J., Kang, M. S., Kim, J. B., Yoon, K. S., Yu, T., Yoon, C., Yang, H. W., Choi, S. J., & Park, E. J. (2025). Chronic lung tissue deposition of inhaled polyethylene microplastics may lead to fibrotic lesions. *Toxicology Reports*, *15*. https://doi.org/10.1016/j.toxrep.2025.102111

Kaewkam, P., Kanchanapaetnukul, A., Khamyan, J., Phadmanee, N., Lin, K. Y. A., Kobwittaya, K., & Sirivithayapakorn, S. (2022). UV-assisted TiO2photocatalytic degradation of virgin LDPE films: Effect of UV-A, UV-C, and TiO2. *Journal of Environmental Chemical Engineering*, *10*(4). https://doi.org/10.1016/j.jece.2022.108131

Kamalian, P., Khorasani, S. N., Abdolmaleki, A., Karevan, M., Khalili, S., Shirani, M., & Neisiany, R. E. (2020). Toward the development of polyethylene photocatalytic degradation. *Journal of Polymer Engineering*, *40*(2), 181–191. https://doi.org/10.1515/polyeng-2019-0230

Kaur, K., & Kaur, H. (2025). Visible light induced photocatalytic degradation of polyvinyl chloride from water using graphene oxide/nitrogen-doped TiO2 nanocomposite. *Journal of Environmental Chemical Engineering*, *13*(2), 115664. https://doi.org/10.1016/j.jece.2025.115664

Kawsar, M., Hossain, M. S., Bahadur, N. M., & Ahmed, S. (2024). Synthesis of nano-crystallite hydroxyapatites in different media and a comparative study for estimation of crystallite size using Scherrer method, Halder-Wagner method size-strain plot, and Williamson-Hall model. *Heliyon*, *10*(3). https://doi.org/10.1016/j.heliyon.2024.e25347

Key, S., Ryan, P. G., Gabbott, S. E., Allen, J., & Abbott, A. P. (2024). Influence of colourants on environmental degradation of plastic litter. *Environmental Pollution*, *347*. https://doi.org/10.1016/j.envpol.2024.123701

Kim, M. G., Kang, J. M., Lee, J. E., Kim, K. S., Kim, K. H., Cho, M., & Lee, S. G. (2021). Effects of Calcination Temperature on the Phase Composition, Photocatalytic Degradation, and Virucidal Activities of TiO2Nanoparticles. *ACS Omega*, *6*(16), 10668–10678. https://doi.org/10.1021/acsomega.1c00043

Kim, W., Tachikawa, T., Moon, G. H., Majima, T., & Choi, W. (2014). Molecular-level understanding of the photocatalytic activity difference between anatase and rutile nanoparticles. *Angewandte Chemie - International Edition*, *53*(51), 14036–14041. https://doi.org/10.1002/anie.201406625

Kinyua, E. M., Nyakairu, G. W. A., Tebandeke, E., & Odume, O. N. (2024). Visible light photocatalytic degradation of HDPE microplastics using vanadium-doped titania. *Central Asian Journal of Water Research*, *10*(1), 126–141. https://doi.org/10.29258/CAJWR/2024-R1.v10-1/126-141.eng

Kohtani, S., Yoshida, K., Maekawa, T., Iwase, A., Kudo, A., Miyabe, H., & Nakagaki, R. (2008). Loading effects of silver oxides upon generation of reactive oxygen species in semiconductor photocatalysis. *Physical Chemistry Chemical Physics*, *10*(20), 2986–2992. https://doi.org/10.1039/b719913a

Koskei, K., Munyasya, A. N., Wang, Y. B., Zhao, Z. Y., Zhou, R., Indoshi, S. N., Wang, W., Cheruiyot, W. K., Mburu, D. M., Nyende, A. B., & Xiong, Y. C. (2021). Effects of increased plastic film residues on soil properties and crop productivity in agro-ecosystem. *Journal of Hazardous Materials*, *414*. https://doi.org/10.1016/j.jhazmat.2021.125521

Kovinchuk, I., Haiuk, N., Lazzara, G., Cavallaro, G., & Sokolsky, G. (2023). Enhanced photocatalytic degradation of PE film by anatase/γ-MnO2. *Polymer Degradation and Stability*, *210*. https://doi.org/10.1016/j.polymdegradstab.2023.110295

Kumari, N., & Mohan, C. (2021). Basics of Clay Minerals and Their Characteristic Properties. In *Clay and Clay Minerals*. IntechOpen. https://doi.org/10.5772/intechopen.97672

Lebreton, L. C. M., van der Zwet, J., Damsteeg, J.-W., Slat, B., Andrady, A., & Reisser, J. (2017). River plastic emissions to the world's oceans. *Nature Communications*, *8*(1), 15611. https://doi.org/10.1038/ncomms15611

Lecoanet, H. F., Bottero, J. Y., & Wiesner, M. R. (2004). Laboratory assessment of the mobility of nanomaterials in porous media. *Environmental Science and Technology*, *38*(19), 5164–5169. https://doi.org/10.1021/es0352303

Li, C., Dong, X., Zhu, N., Zhang, X., Yang, S., Sun, Z., Liu, Y., Zheng, S., & Dionysiou, D. D. (2020). Rational design of efficient visible-light driven

photocatalyst through 0D/2D structural assembly: Natural kaolinite supported monodispersed TiO2 with carbon regulation. *Chemical Engineering Journal*, *396*. https://doi.org/10.1016/j.cej.2020.125311

Li, D., Zhang, N., Yuan, R., Chen, H., Wang, F., & Zhou, B. (2021). Effect of wavelengths on photocatalytic oxidation mechanism of sulfadiazine and sulfamethoxazole in the presence of TiO2. *Journal of Environmental Chemical Engineering*, *9*(5). https://doi.org/10.1016/j.jece.2021.106243

Li, H., Yao, Y., Yang, X., Zhou, X., Lei, R., & He, S. (2022). Degradation of phenol by photocatalysis using TiO2/montmorillonite composites under UV light. *Environmental Science and Pollution Research*, *29*(45), 68293–68305. https://doi.org/10.1007/s11356-022-20638-8

Li, J., Li, Z., Wang, C., Hu, C., Jiang, S., Zhang, C., Zhou, Y., Lin, X., & Xu, J. (2026). Lignin-Based Nanofibrous Membranes for Microplastic Adsorption and Closed-Loop Utilization with Triboelectric Functionalization. *ACS Sustainable Chemistry and Engineering*, *14*(1), 709–721. https://doi.org/10.1021/acssuschemeng.5c11176

Li, M., He, L., Zhang, X., Rong, H., & Tong, M. (2020). Different surface charged plastic particles have different cotransport behaviors with kaolinite ☆particles in porous media. *Environmental Pollution*, *267*. https://doi.org/10.1016/j.envpol.2020.115534

Li, S., Liu, H., Gao, R., Abdurahman, A., Dai, J., & Zeng, F. (2018). Aggregation kinetics of microplastics in aquatic environment: Complex roles of electrolytes, pH, and natural organic matter. *Environmental Pollution*, *237*, 126–132. https://doi.org/10.1016/j.envpol.2018.02.042

Li, X., & Yang, H. (2014). Pd hybridizing ZnO/kaolinite nanocomposites: Synthesis, microstructure, and enhanced photocatalytic property. *Applied Clay Science*, *100*(C), 43–49. https://doi.org/10.1016/j.clay.2014.05.007

Li, Y., Liu, Q., Li, J., Hou, D., Zhang, J., & Li, J. (2022). The preparation of high-yield uniform nanotubes from coal-measure kaolinite. *Applied Clay Science*, *229*. https://doi.org/10.1016/j.clay.2022.106668

Liu, J., Li, X., Zuo, S., & Yu, Y. (2007). Preparation and photocatalytic activity of silver and TiO2 nanoparticles/montmorillonite composites. *Applied Clay Science*, *37*(3–4), 275–280. https://doi.org/10.1016/j.clay.2007.01.008

Liu, P., Qian, L., Wang, H., Zhan, X., Lu, K., Gu, C., & Gao, S. (2019). New Insights into the Aging Behavior of Microplastics Accelerated by Advanced Oxidation Processes. *Environmental Science and Technology*, *53*(7), 3579–3588. https://doi.org/10.1021/acs.est.9b00493

Llorente-García, B. E., Hernández-López, J. M., Zaldívar-Cadena, A. A., Siligardi, C., & Cedillo-González, E. I. (2020). First insights into photocatalytic degradation of HDPE and LDPE microplastics by a mesoporous N-TiO2 coating: Effect of size and shape of microplastics. *Coatings*, *10*(7). https://doi.org/10.3390/coatings10070658

Lu, P. Y., Ningsih, L. A., Heksa, A. C., Hu, C. C., Chen, W. C., & Chiu, Y. C. (2025). Solid base-assisted photocatalytic degradation of polyethylene via the Norrish mechanism through the generation of alternating polyketones. *Polymer Journal*, *57*(5), 575–586. https://doi.org/10.1038/s41428-024-01009-1

Lu, S., Zhu, K., Song, W., Song, G., Chen, D., Hayat, T., Alharbi, N. S., Chen, C., & Sun, Y. (2018). Impact of water chemistry on surface charge and aggregation of polystyrene microspheres suspensions. *Science of the Total Environment*, *630*, 951–959. https://doi.org/10.1016/j.scitotenv.2018.02.296

Magni, S., Binelli, A., Pittura, L., Avio, C. G., Della Torre, C., Parenti, C. C., Gorbi, S., & Regoli, F. (2019). The fate of microplastics in an Italian Wastewater Treatment Plant. *Science of the Total Environment*, *652*, 602–610. https://doi.org/10.1016/j.scitotenv.2018.10.269

Malato, S., Fernández-Ibáñez, P., Maldonado, M. I., Blanco, J., & Gernjak, W. (2009). Decontamination and disinfection of water by solar photocatalysis: Recent overview and trends. In *Catalysis Today* (Vol. 147, Number 1, pp. 1–59). https://doi.org/10.1016/j.cattod.2009.06.018

Maleki, F., Di Liberto, G., & Pacchioni, G. (2023). pH- and Facet-Dependent Surface Chemistry of TiO2 in Aqueous Environment from First Principles. *ACS Applied Materials and Interfaces*, *15*(8), 11216–11224. https://doi.org/10.1021/acsami.2c19273

Maraveas, C., & Hahladakis, J. N. (2025). A scoping review on the European Union agricultural plastic waste management strategies: focusing on liquefaction. In *Journal of Hazardous Materials Advances* (Vol. 18). Elsevier B.V. https://doi.org/10.1016/j.hazadv.2025.100727

Marsh, A., Heath, A., Patureau, P., Evernden, M., & Walker, P. (2018). Alkali activation behaviour of un-calcined montmorillonite and illite clay minerals. *Applied Clay Science*, *166*, 250–261. https://doi.org/10.1016/j.clay.2018.09.011

Md Noor, S. F., Paiman, S. H., Nordin, A. H., Ngadi, N., Nik Malek, N. A. N., & Abd Hamed, N. K. (2024). Solid- and aqueous-phase approaches on zinc oxide-based photocatalytic system for degradation of plastics and microplastics: A review. *Chemical Engineering Research and Design*, *201*, 194–208. https://doi.org/10.1016/j.cherd.2023.11.039

Megha, K. B., Anvitha, D., Parvathi, S., Neeraj, A., Sonia, J., & Mohanan, P. V. (2025). Environmental impact of microplastics and potential health hazards. *Critical Reviews in Biotechnology*, *45*(1), 97–127. https://doi.org/10.1080/07388551.2024.2344572

Microbead-Free Water Act of 2015, Pub. L. Pub. L. 114–114, 21 U.S.C. §§ 331 (2015). https://www.congress.gov/bill/114th-congress/house-bill/1321/text

Miranda, M. N., Sampaio, M. J., Tavares, P. B., Silva, A. M. T., & Pereira, M. F. R. (2021). Aging assessment of microplastics (LDPE, PET and uPVC) under urban environment stressors. *Science of the Total Environment*, *796*. https://doi.org/10.1016/j.scitotenv.2021.148914

Mishra, A., Mehta, A., & Basu, S. (2018). Clay supported TiO2 nanoparticles for photocatalytic degradation of environmental pollutants: A review. In *Journal of*

Environmental Chemical Engineering (Vol. 6, Number 5, pp. 6088–6107). Elsevier Ltd. https://doi.org/10.1016/j.jece.2018.09.029

Mogal, S. I., Mishra, M., Gandhi, V. G., & Tayade, R. J. (2013). Metal doped titanium dioxide: Synthesis and effect of metal ions on physico-chemical and photocatalytic properties. *Materials Science Forum*, *734*, 364–378. https://doi.org/10.4028/www.scientific.net/MSF.734.364

Moharir, R. V., & Kumar, S. (2021). Structural characterization of LDPE films to analyse the impact of heavy metals and effect of UV pre-treatment on polymer degradation. *Journal of Cleaner Production*, *298*. https://doi.org/10.1016/j.jclepro.2021.126670

Moles, S., Ormad, M. P., Gomez, J., Szpunar, J., Bolea, E., & Mosteo, R. (2024). Pilot plant approach combining photocatalysis and adsorption for antibiotics removal from slaughterhouse and urban wastewater treatment plant effluents. *Environmental Technology and Innovation*, *34*. https://doi.org/10.1016/j.eti.2024.103586

Munhoz, D. R., Harkes, P., Beriot, N., Larreta, J., & Basurko, O. C. (2022). Microplastics: A Review of Policies and Responses. *Microplastics*, *2*(1), 1–26. https://doi.org/10.3390/microplastics2010001

Murray, F., & Cowie, P. R. (2011). Plastic contamination in the decapod crustacean Nephrops norvegicus (Linnaeus, 1758). *Marine Pollution Bulletin*, *62*(6), 1207–1217. https://doi.org/10.1016/j.marpolbul.2011.03.032

Nath, D., Singh, F., & Das, R. (2020). X-ray diffraction analysis by Williamson-Hall, Halder-Wagner and size-strain plot methods of CdSe nanoparticles- a comparative study. *Materials Chemistry and Physics*, *239*. https://doi.org/10.1016/j.matchemphys.2019.122021

Ndibewu, P. P., Lefakane, T. E., & Netshiozwi, T. E. (2024). Effects of Titanium Dioxide (TiO2) on Physico-Chemical Properties of Low-Density Polyethylene. *Polymers*, *16*(19). https://doi.org/10.3390/polym16192788

Ningsih, L. A., Lu, P. Y., Ashimura, S., Yoshida, M., Chen, W. C., Chiu, Y. C., & Hu, C. (2024). Highly effective photocatalytic degradation of plastic film (LDPE) using Ruthenium-incorporated g-C3N4 via the Norrish mechanism. *Chemical Engineering Journal*, *480*. https://doi.org/10.1016/j.cej.2023.148089

Nohara, N. M. L., Ariza-Tarazona, M. C., Triboni, E. R., Nohara, E. L., Villarreal-Chiu, J. F., & Cedillo-González, E. I. (2024). Are you drowned in microplastic pollution? A brief insight on the current knowledge for early career researchers developing novel remediation strategies. In *Science of the Total Environment* (Vol. 918). Elsevier B.V. https://doi.org/10.1016/j.scitotenv.2024.170382

Ohtake, Y., Kobayashi, T., Asabe, H., Murakami, N., & Ono, K. (1998). Oxidative Degradation and Molecular Weight Change of LDPE Buried under Bioactive Soil for 32-37 Years. In *J Appl Polym Sci* (Vol. 70). John Wiley & Sons, Inc. https://onlinelibrary.wiley.com/doi/10.1002/(SICI)1097-4628(19981128)70:9%3C1643::AID-APP1%3E3.0.CO;2-V

Osman, A. I., Hosny, M., Eltaweil, A. S., Omar, S., Elgarahy, A. M., Farghali, M., Yap, P.-S., Wu, Y.-S., Nagandran, S., Batumalaie, K., Gopinath, S. C. B., John, O. D., Sekar, M., Saikia, T., Karunanithi, P., Hatta, M. H. M., & Akinyede, K. A. (2023). Microplastic sources, formation, toxicity and remediation: a review. *Environmental Chemistry Letters*, *21*(4), 2129–2169. https://doi.org/10.1007/s10311-023-01593-3

Petronella, F., Truppi, A., Striccoli, M., Curri, M. L., & Comparelli, R. (2019). Photocatalytic Application of Ag/TiO2 Hybrid Nanoparticles. In *Noble Metal-Metal Oxide Hybrid Nanoparticles: Fundamentals and Applications* (pp. 373–394). Elsevier. https://doi.org/10.1016/B978-0-12-814134-2.00018-8

PlasticsEurope. (2025). *Plastics the Facts 2025: An analysis of European plastics production, demand and waste data*. https://plasticseurope.org/knowledge-hub/plastics-the-fast-facts-2025/

Poerio, T., Lavorato, C., Severino, A., Russo, B., Molinari, R., Argurio, P., & Figoli, A. (2024). Combined membrane separation and photocatalysis process for the recovery and decomposition of micro/nanoplastics from polyester fabrics. *Journal of Environmental Chemical Engineering*, *12*(5). https://doi.org/10.1016/j.jece.2024.113310

Priya, K. L., Renjith, K. R., Joseph, C. J., Indu, M. S., Srinivas, R., & Haddout, S. (2022). Fate, transport and degradation pathway of microplastics in aquatic environment — A critical review. In *Regional Studies in Marine Science* (Vol. 56). Elsevier B.V. https://doi.org/10.1016/j.rsma.2022.102647

Ramírez-Escárcega, K. J., Amaya-Galván, K. J., García-Prieto, J. C., Silerio-Vázquez, F. de J., & Proal-Nájera, J. B. (2025). Advancing photocatalytic strategies for microplastic degradation in aquatic systems: Insights into key challenges and future pathways. In *Journal of Environmental Chemical Engineering* (Vol. 13, Number 2). Elsevier Ltd. https://doi.org/10.1016/j.jece.2025.115594

Reinicker, R. (2018). *38 Pigments and Colorants for Polyethylene*.

Reinoso-Maset, E., & Ly, J. (2016). Study of uranium(VI) and radium(II) sorption at trace level on kaolinite using a multisite ion exchange model. *Journal of Environmental Radioactivity*, *157*, 136–148. https://doi.org/10.1016/j.jenvrad.2016.03.014

Romero, P., & Garg, N. (2022). Evolution of kaolinite morphology upon exfoliation and dissolution: Evidence for nanoscale layer thinning in metakaolin. *Applied Clay Science*, *222*. https://doi.org/10.1016/j.clay.2022.106486

Sanoja-López, K. A., Suarez, C., Navia-Pesantes, O., Quiroz-Suárez, K. A., & Luque, R. (2026). Advanced strategies for the detection, Removal, and degradation of microplastics: Bridging science and sustainable technologies. *Results in Engineering*, *29*, 109743. https://doi.org/10.1016/j.rineng.2026.109743

Sayam, S., Islam, T., Tusti, T. H., & Ghosh, J. (2026). Microplastic removal from wastewater through biopolymer and nanocellulose-based green technologies. In *RSC Sustainability* (Vol. 4, Number 1, pp. 79–117). Royal Society of Chemistry. https://doi.org/10.1039/d5su00634a

Senthil Kumar, R., & Gnanavel, B. (2017). High performance catalytic activity of pure and silver (Ag) doped TiO2 nanoparticles by a novel microwave irradiation technique. *Journal of Materials Science: Materials in Electronics*, *28*(5), 4253–4259. https://doi.org/10.1007/s10854-016-6048-2

Shi, H., Zhang, T., An, T., Li, B., & Wang, X. (2012). Enhancement of photocatalytic activity of nano-scale TiO 2 particles co-doped by rare earth elements and heteropolyacids. *Journal of Colloid and Interface Science*, *380*(1), 121–127. https://doi.org/10.1016/j.jcis.2012.04.069

Siddiqui, H. (2020). Modification of Physical and Chemical Properties of Titanium Dioxide (TiO 2) by Ion Implantation for Dye Sensitized Solar Cells . In *Ion Beam Techniques and Applications*. IntechOpen. https://doi.org/10.5772/intechopen.83566

Singh, N., Tiwari, E., Khandelwal, N., & Darbha, G. K. (2019). Understanding the stability of nanoplastics in aqueous environments: Effect of ionic strength, temperature, dissolved organic matter, clay, and heavy metals. *Environmental Science: Nano*, *6*(10), 2968–2976. https://doi.org/10.1039/c9en00557a

Sitorus, B., Silaban, F., & Aritonang, A. B. (2025). Optical Properties Characterization of TiO_2-Metakaolin Composites Synthesized by the Sol-Gel Method. *Jurnal Kimia Sains Dan Aplikasi*, *28*(2), 62–67. https://doi.org/10.14710/jksa.28.2.62-67

Song, Z., Yang, X., Chen, F., Zhao, F., Zhao, Y., Ruan, L., Wang, Y., & Yang, Y. (2019). Fate and transport of nanoplastics in complex natural aquifer media: Effect of particle size and surface functionalization. *Science of the Total Environment*, *669*, 120–128. https://doi.org/10.1016/j.scitotenv.2019.03.102

Sorasan, C., Ortega-Ojeda, F. E., Rodríguez, A., & Rosal, R. (2022). Modelling the Photodegradation of Marine Microplastics by Means of Infrared Spectrometry and Chemometric Techniques. *Microplastics*, *1*(1), 198–210. https://doi.org/10.3390/microplastics1010013

Sørensen, L., Groven, A. S., Hovsbakken, I. A., Del Puerto, O., Krause, D. F., Sarno, A., & Booth, A. M. (2021). UV degradation of natural and synthetic microfibers causes fragmentation and release of polymer degradation products and chemical additives. *Science of the Total Environment*, *755*. https://doi.org/10.1016/j.scitotenv.2020.143170

Stancu, A. G., Râpă, M., Popa, C. L., Donțu, S. I., Matei, E., & Covaliu-Mirelă, C. I. (2025). Degradation of Emerging Plastic Pollutants from Aquatic Environments Using TiO2 and Their Composites in Visible Light Photocatalysis. In *Molecules* (Vol. 30, Number 15). Multidisciplinary Digital Publishing Institute (MDPI). https://doi.org/10.3390/molecules30153186

Sun, Y., Li, G., Gong, Y., Sun, Z., Yao, H., & Zhou, X. (2021). Ag and TiO2 nanoparticles co-modified defective zeolite TS-1 for improved photocatalytic CO2 reduction. *Journal of Hazardous Materials*, *403*. https://doi.org/10.1016/j.jhazmat.2020.124019

Sura, A., & Nain, S. (2024). Visible light driven degradation of BPA and LDPE microplastic films using GO/SCN nanocomposite. *RSC Advances*, *14*(48), 35336–35347. https://doi.org/10.1039/d4ra06055e

Surana, M., Pattanayak, D. S., Yadav, V., Singh, V. K., & Pal, D. (2024). An insight decipher on photocatalytic degradation of microplastics: Mechanism, limitations, and future outlook. In *Environmental Research* (Vol. 247). Academic Press Inc. https://doi.org/10.1016/j.envres.2024.118268

Suresh, B., Maruthamuthu, S., Kannan, M., & Chandramohan, A. (2011). Mechanical and surface properties of low-density polyethylene film modified by photo-oxidation. *Polymer Journal*, *43*(4), 398–406. https://doi.org/10.1038/pj.2010.147

Szołdra, P., Frąc, M., Lach, R., Zych, Ł., Radecka, M., Trenczek-Zając, A., & Pichór, W. (2023). Effect of brookite on the photocatalytic properties of mixed-phase TiO2 obtained at a higher temperature. *Materials Science and Engineering: B*, *287*. https://doi.org/10.1016/j.mseb.2022.116104

Tan, S. Y., Chong, W. C., Sethupathi, S., Pang, Y. L., Sim, L. C., & Mahmoudi, E. (2023). Optimisation of aqueous phase low density polyethylene degradation by graphene oxide-zinc oxide photocatalysts. *Chemical Engineering Research and Design*, *190*, 550–565. https://doi.org/10.1016/j.cherd.2022.12.045

Tauc, J., Grigorovici, R., & Vancu, A. (1966). Optical Properties and Electronic Structure of Amorphous Germanium. *Physica Status Solidi (b)*, *15*(2), 627–637. https://doi.org/10.1002/pssb.19660150224

Tejaswini, M. S. S. R., & Pathak, P. (2023). In-situ photocatalytic degradation of low-density polyethylene: A pathway towards eco-sustainability and circular economy. *Sustainable Chemistry and Pharmacy*, *36*. https://doi.org/10.1016/j.scp.2023.101320

Thompson, R. C., Olsen, Y., Mitchell, R. P., Davis, A., Rowland, S. J., John, A. W. G., McGonigle, D., & Russell, A. E. (2004). Lost at Sea: Where Is All the Plastic? *Science*, *304*(5672), 838–838. https://doi.org/10.1126/science.1094559

Tofa, T. S., Kunjali, K. L., Paul, S., & Dutta, J. (2019). Visible light photocatalytic degradation of microplastic residues with zinc oxide nanorods. *Environmental Chemistry Letters*, *17*(3), 1341–1346. https://doi.org/10.1007/s10311-019-00859-z

Tofa, T. S., Ye, F., Kunjali, K. L., & Dutta, J. (2019). Enhanced visible light photodegradation of microplastic fragments with plasmonic platinum/zinc oxide nanorod photocatalysts. *Catalysts*, *9*(10). https://doi.org/10.3390/catal9100819

Tombácz, E., & Szekeres, M. (2004). Colloidal behavior of aqueous montmorillonite suspensions: the specific role of pH in the presence of indifferent electrolytes. *Applied Clay Science*, *27*(1–2), 75–94. https://doi.org/10.1016/j.clay.2004.01.001

Toro, R. G., Diab, M., de Caro, T., Al-Shemy, M., Adel, A., & Caschera, D. (2020). Study of the effect of titanium dioxide hydrosol on the photocatalytic and mechanical properties of paper sheets. *Materials*, *13*(6). https://doi.org/10.3390/ma13061326

Turchi, C., & Ollis, D. (1990). Photocatalytic degradation of organic water contaminants: Mechanisms involving hydroxyl radical attack. *Journal of Catalysis*, *122*(1), 178–192. https://doi.org/10.1016/0021-9517(90)90269-P

Uheida, A., Mejía, H. G., Abdel-Rehim, M., Hamd, W., & Dutta, J. (2021). Visible light photocatalytic degradation of polypropylene microplastics in a continuous water flow system. *Journal of Hazardous Materials*, *406*. https://doi.org/10.1016/j.jhazmat.2020.124299

Uogintė, I., Pleskytė, S., Pauraitė, J., & Lujanienė, G. (2022). Seasonal variation and complex analysis of microplastic distribution in different WWTP treatment stages in Lithuania. *Environmental Monitoring and Assessment*, *194*(11). https://doi.org/10.1007/s10661-022-10478-x

Uogintė, I., Pleskytė, S., Skapas, M., Stanionytė, S., & Lujanienė, G. (2023). Degradation and optimization of microplastic in aqueous solutions with graphene oxide-based nanomaterials. *International Journal of Environmental Science and Technology*, *20*(9), 9693–9706. https://doi.org/10.1007/s13762-022-04657-z

Ural, N. (2021). The significance of scanning electron microscopy (SEM) analysis on the microstructure of improved clay: An overview. In *Open Geosciences* (Vol. 13, Number 1, pp. 197–218). De Gruyter Open Ltd. https://doi.org/10.1515/geo-2020-0145

Vallada, D. D. S., Moraes, C. A. M., & Silva, P. R. S. da. (2020). Thermal pyrolysis of LDPE and LLDPE films in post-consumer packaging. *Revista Eletrônica Em Gestão, Educação e Tecnologia Ambiental*, *24*, e23. https://doi.org/10.5902/2236117062698

van Schothorst, B., Beriot, N., Huerta Lwanga, E., & Geissen, V. (2021). Sources of Light Density Microplastic Related to Two Agricultural Practices: The Use of Compost and Plastic Mulch. *Environments*, *8*(4), 36. https://doi.org/10.3390/environments8040036

Varnagiris, S., Urbonavicius, M., Sakalauskaite, S., Daugelavicius, R., Pranevicius, L., Lelis, M., & Milcius, D. (2020). Floating TiO2 photocatalyst for efficient inactivation of E. coli and decomposition of methylene blue solution. *Science of the Total Environment*, *720*. https://doi.org/10.1016/j.scitotenv.2020.137600

Venkataramana, C., Botsa, S. M., Shyamala, P., & Muralikrishna, R. (2021). Photocatalytic degradation of polyethylene plastics by NiAl2O4 spinels-synthesis and characterization. *Chemosphere*, *265*. https://doi.org/10.1016/j.chemosphere.2020.129021

Walker, T. R., & Fequet, L. (2023). Current trends of unsustainable plastic production and micro(nano)plastic pollution. In *TrAC - Trends in Analytical Chemistry* (Vol. 160). Elsevier B.V. https://doi.org/10.1016/j.trac.2023.116984

Wang, C. Y., He, G. J., Huang, W. T., Cao, X. W., Zou, X. L., & Feng, Y. H. (2022). Controlled functionalisation of PE in molten state using ozone at the gas-fluid interface. *Polymer Degradation and Stability*, *202*. https://doi.org/10.1016/j.polymdegradstab.2022.110025

Wang, D., Zhang, P., Yan, M., Jin, L., Du, X., Zhang, F., Wang, Q., Ni, B., & Chen, C. (2022). Degradation mechanism and properties of debris of photocatalytically degradable plastics LDPE-TiO2 vary with environments. *Polymer Degradation and Stability*, *195*. https://doi.org/10.1016/j.polymdegradstab.2021.109806

Wang, J., Sun, C., Huang, Q. X., Chi, Y., & Yan, J. H. (2021). Adsorption and thermal degradation of microplastics from aqueous solutions by Mg/Zn modified magnetic biochars. *Journal of Hazardous Materials*, *419*. https://doi.org/10.1016/j.jhazmat.2021.126486

Wang, K., Zhuo, Y., Chen, J., Gao, D., Ren, Y., Wang, C., & Qi, Z. (2020). Crystalline phase regulation of anatase-rutile TiO2for the enhancement of photocatalytic activity. *RSC Advances*, *10*(71), 43592–43598. https://doi.org/10.1039/d0ra09421h

Wang, R., Li, H., Ge, G., Dai, N., Rao, J., Ran, H., & Zhang, Y. (2021). Montmorillonite-based two-dimensional nanocomposites: Preparation and applications. *Molecules*, *26*(9). https://doi.org/10.3390/molecules26092521

Wang, T., Li, Y., Pan, J. hao, Zhang, Y. ling, Wu, L. guang, Dong, C. ying, & Li, C. juan. (2019). Alcohol solvothermal reduction for commercial P25 to harvest weak visible light and fabrication of the resulting floating photocatalytic spheres. *Scientific Reports*, *9*(1). https://doi.org/10.1038/s41598-019-50457-w

Wang, X., Teo, S. H., Shamsuddin, M. R., & Wid, N. (2025). Influence of Ag-concentration on TiO2-supported catalysts for photocatalytic degradation of microplastics PA66 in marine. *Regional Studies in Marine Science*, *81*. https://doi.org/10.1016/j.rsma.2024.103922

Wright, S. L., Thompson, R. C., & Galloway, T. S. (2013). The physical impacts of microplastics on marine organisms: a review. In *Environmental pollution (Barking, Essex : 1987)* (Vol. 178, pp. 483–492). https://doi.org/10.1016/j.envpol.2013.02.031

Wu, P., Huang, J., Zheng, Y., Yang, Y., Zhang, Y., He, F., Chen, H., Quan, G., Yan, J., Li, T., & Gao, B. (2019). Environmental occurrences, fate, and impacts of microplastics. In *Ecotoxicology and Environmental Safety* (Vol. 184). Academic Press. https://doi.org/10.1016/j.ecoenv.2019.109612

Yagoubi, W., Abdelhafidi, A., Sebaa, M., & Chabira, S. F. (2015). Identification of carbonyl species of weathered LDPE films by curve fitting and derivative analysis of IR spectra. *Polymer Testing*, *44*, 37–48. https://doi.org/10.1016/j.polymertesting.2015.03.008

Yang, S. B., Lee, J., Yeasmin, S., Park, J. M., Han, M. D., Kwon, D. J., & Yeum, J. H. (2022). Blown Composite Films of Low-Density/Linear-Low-Density Polyethylene and Silica Aerogel for Transparent Heat Retention Films and Influence of Silica Aerogel on Biaxial Properties. *Materials*, *15*(15). https://doi.org/10.3390/ma15155314

Yang, Y., Li, Z., Yan, C., Chadwick, D., Jones, D. L., Liu, E., Liu, Q., Bai, R., & He, W. (2022). Kinetics of microplastic generation from different types of mulch

films in agricultural soil. *Science of the Total Environment*, *814*. https://doi.org/10.1016/j.scitotenv.2021.152572

Yatoo, A. M., Hamid, B., Sheikh, T. A., Ali, S., Bhat, S. A., Ramola, S., Ali, M. N., Baba, Z. A., & Kumar, S. (2024). Global perspective of municipal solid waste and landfill leachate: generation, composition, eco-toxicity, and sustainable management strategies. In *Environmental Science and Pollution Research* (Vol. 31, Number 16, pp. 23363–23392). Springer. https://doi.org/10.1007/s11356-024-32669-4

Yuwendi, Y., Ibadurrohman, M., Setiadi, S., & Slamet, S. (2022). Photocatalytic Degradation of Polyeth-ylene Microplastics and Disinfection of E. coli in Water over Fe-and Ag-Modified TiO2 Nanotubes. *Bulletin of Chemical Reaction Engineering & Catalysis*, *17*(2), 263–277. https://doi.org/10.9767/bcrec.17.2.123400.263-277

Zeng, C., & Kobayashi, M. (2025). Charging and Aggregation of Nano-Clay Na-Montmorillonite in the Presence of Ciprofloxacin. *Nanomaterials*, *15*(5). https://doi.org/10.3390/nano15050389

Zhang, C., Huang, L., & Nekliudov, A. (2024). Construction of loading g-C3N4/TiO2 on waste cotton-based activated carbon S-scheme heterojunction for enhanced photocatalytic degradation of microplastics: Performance, DFT calculation and mechanism study. *Optical Materials*, *154*. https://doi.org/10.1016/j.optmat.2024.115786

Zhang, J., Zhou, P., Liu, J., & Yu, J. (2014). New understanding of the difference of photocatalytic activity among anatase, rutile and brookite TiO2. *Physical Chemistry Chemical Physics*, *16*(38), 20382–20386. https://doi.org/10.1039/c4cp02201g

Zhang, K., Hamidian, A. H., Tubić, A., Zhang, Y., Fang, J. K. H., Wu, C., & Lam, P. K. S. (2021). Understanding plastic degradation and microplastic formation in the environment: A review. In *Environmental Pollution* (Vol. 274). Elsevier Ltd. https://doi.org/10.1016/j.envpol.2021.116554

Zhang, Y., Gan, H., & Zhang, G. (2011). A novel mixed-phase TiO 2/kaolinite composites and their photocatalytic activity for degradation of organic contaminants. *Chemical Engineering Journal*, *172*(2–3), 936–943. https://doi.org/10.1016/j.cej.2011.07.005

Zheng, D., Duan, J., Wu, Y., & Dong, W. (2024). Polystyrene microplastics facilitated the photoconversion of losartan potassium: The pivotal role of aging and reactive oxygen species. *Process Safety and Environmental Protection*, *187*, 698–706. https://doi.org/10.1016/j.psep.2024.05.022

Zheng, X., Zhang, D., Gao, Y., Wu, Y., Liu, Q., & Zhu, X. (2019). Synthesis and characterization of cubic Ag/TiO2 nanocomposites for the photocatalytic degradation of methyl orange in aqueous solutions. *Inorganic Chemistry Communications*, *110*. https://doi.org/10.1016/j.inoche.2019.107589

Zhou, D., Luo, H., Zhang, F., Wu, J., Yang, J., & Wang, H. (2022). Efficient Photocatalytic Degradation of the Persistent PET Fiber-Based Microplastics over Pt

Nanoparticles Decorated N-Doped TiO2 Nanoflowers. *Advanced Fiber Materials*, *4*(5), 1094–1107. https://doi.org/10.1007/s42765-022-00149-4

Zhou, H., Wang, H., Yue, C., He, L., Li, H., Zhang, H., Yang, S., & Ma, T. (2024). Photocatalytic degradation by TiO2-conjugated/coordination polymer heterojunction: Preparation, mechanisms, and prospects. In *Applied Catalysis B: Environmental* (Vol. 344). Elsevier B.V. https://doi.org/10.1016/j.apcatb.2023.123605

Zhu, K., Jia, H., Sun, Y., Dai, Y., Zhang, C., Guo, X., Wang, T., & Zhu, L. (2020). Long-term phototransformation of microplastics under simulated sunlight irradiation in aquatic environments: Roles of reactive oxygen species. *Water Research*, *173*. https://doi.org/10.1016/j.watres.2020.115564

Zhu, M., Wang, H., Keller, A. A., Wang, T., & Li, F. (2014). The effect of humic acid on the aggregation of titanium dioxide nanoparticles under different pH and ionic strengths. *Science of the Total Environment*, *487*(1), 375–380. https://doi.org/10.1016/j.scitotenv.2014.04.036

Zhu, X., Rochman, C. M., Hardesty, B. D., & Wilcox, C. (2024). Plastics in the deep sea – A global estimate of the ocean floor reservoir. *Deep-Sea Research Part I: Oceanographic Research Papers*, *206*. https://doi.org/10.1016/j.dsr.2024.104266

Zou, Y., Hu, Y., Shen, Z., Yao, L., Tang, D., Zhang, S., Wang, S., Hu, B., Zhao, G., & Wang, X. (2022). Application of aluminosilicate clay mineral-based composites in photocatalysis. In *Journal of Environmental Sciences (China)* (Vol. 115, pp. 190–214). Chinese Academy of Sciences. https://doi.org/10.1016/j.jes.2021.07.015

CURRICULUM VITAE

Name:	Sonata
Surname:	Pleskytė
E-mail:	sonata.pleskyte@ftmc.lt

Education:

2022–2026	State Research Institute Center for Physical Sciences and Technology (FTMC) Department of Environmental Research *Ph.D. studies (Natural Sciences, Chemistry – N 003)*
2020–2022	Vilnius University, Faculty of Chemistry and Geosciences *Master's degree in Chemistry*
2016–2020	Vilnius Tech University, Faculty of Fundamental Sciences *Bachelor's degree in Bioengineering*

Work experience:

2024–present	Junior researcher, FTMC
2022–2024	Senior engineer, FTMC
2020-2022	Senior engineer, National Food and Veterinary Risk Assessment Institute (NMVRVI)

GYVENIMO APRAŠYMAS

Vardas:	Sonata
Pavardė:	Pleskytė
El. paštas:	sonata.pleskyte@ftmc.lt

Išsilavinimas:

2022–2026	Valstybinis mokslinių tyrimų institutas Fizinių ir technologijos mokslų centras (FTMC) Aplinkotyros skyrius. *Doktorantūra (gamtos mokslai, chemija – N 003)*
2020–2022	Vilniaus Universitetas, Chemijos ir geomokslų fakultetas *Chemijos magistro laipsnis*
2016–2020	Vilnius Tech Universitetas, Fundamentinių mokslų fakultetas *Bioinžinerijos bakalauro laipsnis*

Profesinė veikla:

2024–dabartis	Jaunesnioji mokslo darbuotoja, FTMC
2022–2024	Vyresnioji inžinierė, FTMC
2020–2022	Vyresnioji inžinierė, Nacionalinis maisto ir veterinarijos rizikos vertinimo institutas (NMVRVI)

FOR NOTES

FOR NOTES

FOR NOTES

FOR NOTES

Vilniaus universiteto leidykla
Saulėtekio al. 9, III rūmai, LT-10222 Vilnius
El. p. info@leidykla.vu.lt, www.leidykla.vu.lt
bookshop.vu.lt, journals.vu.lt
Tiražas 35 egz.